

INFORMATION TO USERS

This manuscript has been reproduced from the microfilm master. UMI films the text directly from the original or copy submitted. Thus, some thesis and dissertation copies are in typewriter face, while others may be from any type of computer printer.

The quality of this reproduction is dependent upon the quality of the copy submitted. Broken or indistinct print, colored or poor quality illustrations and photographs, print bleedthrough, substandard margins, and improper alignment can adversely affect reproduction.

In the unlikely event that the author did not send UMI a complete manuscript and there are missing pages, these will be noted. Also, if unauthorized copyright material had to be removed, a note will indicate the deletion.

Oversize materials (e.g., maps, drawings, charts) are reproduced by sectioning the original, beginning at the upper left-hand corner and continuing from left to right in equal sections with small overlaps. Each original is also photographed in one exposure and is included in reduced form at the back of the book.

Photographs included in the original manuscript have been reproduced xerographically in this copy. Higher quality 6" x 9" black and white photographic prints are available for any photographs or illustrations appearing in this copy for an additional charge. Contact UMI directly to order.

UMI[®]

**Bell & Howell Information and Learning
300 North Zeeb Road, Ann Arbor, MI 48106-1346 USA
800-521-0600**

RESULTS FROM THE 1994 LSND NEUTRINO
OSCILLATION SEARCHES IN BOTH THE
 $\bar{\nu}_\mu \longrightarrow \bar{\nu}_e$ AND $\nu_\mu \longrightarrow \nu_e$
CHANNELS

James E Hill

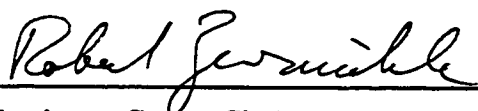
A DISSERTATION
in PHYSICS AND ASTRONOMY

Presented to the Faculties of the University of Pennsylvania in Partial
Fulfillment of the Requirements for the Degree of Doctor of Philosophy

1995



Supervisor of Dissertation



Graduate Group Chairperson

UMI Number: 9936813

UMI Microform 9936813

Copyright 1999, by UMI Company. All rights reserved.

**This microform edition is protected against unauthorized
copying under Title 17, United States Code.**

UMI

**300 North Zeeb Road
Ann Arbor, MI 48103**

Acknowledgements

“Let us begin from the beginning” as Alice said. I have often commented that no one ever seems to remember they were alive before grad school in their thesis acknowledgements, with the occasional exception of reference to one’s parents. I really feel, not only in the broad psycho-philosophical way of Sartre’s “Les Jeux Sont Fait”, but in a simpler more human way that my graduation now would not be possible without the strong help and guidance of not only my family, but my childhood friends and grammar school teachers. Particularly of note in the latter category are the late Miss Gardner, my kindergarden teacher, and Mr. Ripicki, the first real science teacher I had in 2nd grade. (I believe he has a masters in physics.) Also, not only personally, but for my whole family, I need to thank Mr. O’Brien, the headmaster of Saint Gregory’s School for Boys when I and my brothers were students there. In high school, many teachers were influential in my life, but particularly of note in this context are Mr. Olcott, from whom I learned the first basics of calculus, and Dr. Schmalberger, who left a full professorship in Astronomy to get to “real teaching” in Albany Boys Academy where I went to high school.

I still keep up with many of my friends from teenage days (and before) and without their support I would not have bothered with this arduous task of leaving home to come and study more years here. I know that some of them do not understand what

it is I want to do here, but they still help give me the strength to do it.

While my college history is somewhat mottled, I think the most important contributors to my having continued on the road that lead me here were Professors Bruce Marsh and Richard Goldstein, neither of whom was my official advisor, but both of whom let me describe what I felt my interests were and set me along a right course. (Goldstein's PhD is from Penn.) I owe a great debt to the physics and math departments of SUNY, and to the university as a whole for letting me pursue this goal after some time away from college. In most of the world this would not be possible, but there it was encouraged.

Finally, here at Penn and for shorter stays at Los Alamos and at Brookhaven, where this is seemingly coming to its fruition at some level, I have all these recent contacts that have very directly helped along the way. The first in rank is of course, my advisor, A.K.Mann. He has a reputation in the community of neutrino physics of working very hard to help his students find jobs. While this is undoubtably true, it is even more important, and now more obvious to me, that he also works very hard to make his students capable independent researchers. The undergraduates that he takes as his students are some of the best people (of any rank) with whom I have had the pleasure of working, and they deserve my acknowledgement as much as anyone. Also, Professor Gene Beier, for whom I worked two summers,

has taught me much about really doing physics. My experiences teaching, especially for the Math department here, are one of the strongest parts of my education, and I want to thank all of my students who taught me so much.

At Los Alamos, many people, especially the post-docs Randy Reeder, Jeremy Margulies, and Ion Stancu, have contributed to my understanding both the physics we are doing and the tools of physics analysis. Randy also knows all the best hikes in northern New Mexico.

Last, but not least, I need to mention several of my school-mates here. My friends Maneesh Deshpande and Farrukh Azfar have been close to me ever since we came here together 5 years ago. Naoya Hata has been not only a good friend, but also a great teacher of analyzing data for the very type of work I am doing. Most to me is my very closest friend, Shafinaz Ali (who is now working on her doctorate at Bartol). She has helped me be a better person. Without her strength and support, I am sure I would not have gotten through the ordeal of my qualifying exam, and so many personal struggles along the way here.

A few weeks before I came to Penn for graduate school, I was riding somewhere with my father, and he asked “What the hell are you going to do with all this school crap, anyway?” Well, this is it. My father died two years before I was able to finish. My 97 year old grandmother, though, is still around, and aware enough to be proud of me for this. She and my other two living

grandparents (both well into their 80's) are inspirational to me in their quiet strength in the face of lives that in most ways were not as easy as mine. On that scale, this work is very small indeed.

ABSTRACT

Results From the 1994 LSND Neutrino
Oscillation Searches in Both the

$$\bar{\nu}_{\mu} \longrightarrow \bar{\nu}_e \text{ and } \nu_{\mu} \longrightarrow \nu_e$$

Channels

Jim Hill

Prof. A.K. Mann

The Liquid Scintillator Neutrino Detector (LSND) 1994 data for the oscillation searches $\nu_{\mu} \rightarrow \nu_e$ and $\bar{\nu}_{\mu} \rightarrow \bar{\nu}_e$ yield limits on the mixing of the two flavors. A combined treatment of the two channels, and the resulting new limits are presented, under the assumptions of 2 family mixing and no CP violating terms in the mixing matrix. Appended to the main work, a critique is made of the analysis that seems to find a strong signal in the same data, and problems with that analysis are identified.

Contents

1	Introduction: The theory of neutrino oscillations	1
1.1	A general overview	1
1.2	Neutrino masses and the standard model . .	6
1.2.1	“Normal” mass terms	7
1.2.2	Other possible mass terms	9
1.3	Some history	15
2	The LAMPF neutrino beam	19
2.1	Physical configuration of the beam area . . .	20
2.2	Processes for neutrino production	22
2.3	The beam Monte Carlo	26
2.4	The neutrino beam spectra, a synopsis . . .	27
3	The Liquid Scintillator Neutrino Detector	34
3.1	Charged particle detection for neutrino physics	34
3.1.1	Čerenkov detection with mineral oil . . .	35
3.1.2	Liquid scintillator and charged particle de- tection	36

3.1.3	Combining Čerenkov and scintillator detectors	37
3.2	Passive shielding of the detector	38
3.3	The active veto shield	41
3.4	Front end electronics	43
3.5	The event trigger subsystem	46
4	Events in LSND	56
4.1	Calibration	57
4.1.1	Laser calibration	57
4.1.2	Electron energy	59
4.1.3	Gamma energy	62
4.2	Event reconstruction	64
4.2.1	Electron reconstruction	65
4.2.2	Gamma reconstruction	68
4.3	Particle Identification	69
4.3.1	Monte Carlo predictions	72
4.4	A tour through the data	74
5	Selection of $\bar{\nu}_\mu \rightarrow \bar{\nu}_e$ event candidates	88
5.1	Signal event signature	89
5.2	The fiducial region chosen	89
5.3	Selection based on previous events	94
5.4	Rejection for in-time veto system activity . .	96
5.5	Particle identification selection	97

5.6	The choice to include only 1994 data	98
5.7	Selection of correlated gamma rays	100
5.8	Signal event rates	102
5.9	Major $\bar{\nu}_\mu \rightarrow \bar{\nu}_e$ background sources	103
6	Selection of $\nu_\mu \rightarrow \nu_e$ event candidates	118
6.1	Signal event signature	118
6.2	The fiducial region chosen	120
6.3	Selection based on previous events	121
6.4	Rejection for in-time veto system activity . .	121
6.5	Particle identification selection	122
6.6	Signal event rates	124
6.7	Major $\nu_\mu \rightarrow \nu_e$ background sources	127
7	Data analysis and results	135
7.1	Statistical methods	135
7.2	Two separate limits	140
7.2.1	Mixing limit for $\bar{\nu}_\mu \rightarrow \bar{\nu}_e$	140
7.2.2	Mixing limit for $\nu_\mu \rightarrow \nu_e$	142
7.3	The combined limit	143
7.4	Improving on these limits	144
A	A critical look at other analyses	160
A.1	Event selection for the positive result	161
A.2	Interpretation of that event sample	165
A.3	Questions about the validity of the sample .	166

A.3.1	The intricacy of the selection criteria . . .	166
A.3.2	Some questionable distributions	169
B	Understanding the LAMPF neutrino beam	181
B.1	Pion yields in the A6 water target	182
B.2	The decay-in-flight spectrum of ν_μ	189
B.2.1	Detailed calculation for a special case . .	190

List of Tables

5.1	The effect of the “Y cut” on the $\nu_e C$ sample . . .	106
5.2	Standard decay at rest selection criteria	107
5.3	Major $\bar{\nu}_\mu \rightarrow \bar{\nu}_e$ backgrounds	108
5.4	Qualitative stability for changes in the decay at rest e^\pm selection	109
5.5	Qualitative stability for changes in the decay at rest γ selection	110
6.1	Standard decay-in-flight candidate selection . . .	130
6.2	Major $\nu_\mu \rightarrow \nu_e$ backgrounds	131
6.3	Qualitative stability for changes in the decay-in- flight e^\pm selection	132

List of Figures

1.1	Previous limits in the range studied	18
2.1	Timing structure of the LAMPF proton beam . .	28
2.2	The relative position of the detector and beam .	29
2.3	The whole LAMPF area	30
2.4	Feynman diagram for muon decay	31
2.5	Monte Carlo decay-in-flight neutrino fluxes for π in A6 area	32
2.6	Theoretical ν spectra for μ and π decay-at-rest .	33
3.1	Cross sections of the main detector	50
3.2	Cross section of the active veto shield	51
3.3	Signals in the front end electronics	52
3.4	Front end electronics schematic	53
3.5	The “Flash” ADC chip	54
3.6	Trigger logic flowchart	55
4.1	Reconstructed position error for laser events . . .	77
4.2	Muon decay time from a sample of vetoed cosmic rays	78

4.3	Spectrum of electrons from stopped muon decay	79
4.4	Beta spectrum tail with calibration fit	80
4.5	Gamma properties for a sample from the full run	81
4.6	Fiducial distance for e^\pm from stopped μ decay . .	82
4.7	Raw particle id parameter	83
4.8	Raw particle id. parameter versus energy	84
4.9	Energy corrected particle id. versus energy . . .	85
4.10	Energy corrected particle id.	86
4.11	PMT multiplicity for <i>all</i> events in 80 minutes . .	87
5.1	Projections of positions of background events . .	111
5.2	$d_\gamma^{(e)}(y, z)$ for accidental coincidences	112
5.3	Regions used in previous figure	113
5.4	Fiducial region used for the decay at rest search .	114
5.5	Y coordinate for decay at rest background events	115
5.6	1993 data with 1994 particle identification	116
5.7	Average gamma properties used for selection . .	117
6.1	$\chi_{\text{PID}}^{\text{cor.}}$ versus E over a broad range	133
6.2	$\chi_{\text{PID}}^{\text{cor.}}$ for $\nu_\mu \rightarrow \nu_e$ candidates	134
7.1	Exclusion plot for decay at rest oscillation search	149
7.2	$\bar{\nu}_\mu \rightarrow \bar{\nu}_e$ exclusion plot for case of lower background	150
7.3	Exclusion plot for decay-in-flight search	151
7.4	(Weaker) $\nu_\mu \rightarrow \nu_e$ exclusion assuming no ν back- grounds	152

7.5	$\nu_\mu \rightarrow \nu_e$ exclusion assuming low cross sections . .	153
7.6	Exclusion plot for combined data sets	154
7.7	Combined fit result assuming 1 degree of freedom	155
7.8	Combined fit if ν_e ^{12}C is low by a factor of 2 . . .	156
7.9	LSND limit compared to other published results	157
7.10	Comparison of other data and low sigma result .	158
7.11	Extrapolation for limits after another 4 month run.	159
A-1	Coordinate projections of volume used in other analysis	174
A-2	Approximate allowed region from positive result	175
A-3	Acceptance of the “flat” PID cuts as a function of energy	176
A-4	Gamma correlation in a particularly bad corner .	177
A-5	Y-Z coordinate projection of background events .	178
A-6	Y-X coordinate projection of background events .	179
A-7	Coordinate projections of claimed signal events .	180
B-1	Analytically calculated decay in flight spectrum .	193
B-2	Monte Carlo spectrum for π^\pm decay in flight . . .	193

Chapter 1

Introduction: The theory of neutrino oscillations

The Standard Model of electro-weak interactions in particle physics is generally presented in a form with the neutrino masses all identically set to zero, but it accommodates the input of non-zero masses for the neutral leptons. If these masses *are* finite, and if the mass eigenstates are not the same as the weak “flavor” eigenstates, the phenomenon of neutrino oscillation occurs.

1.1 A general overview

Neutrino oscillation was first suggested (before the advent of the standard model) by Pontecorvo [1] in 1957. After the

discovery of the phenomenon of oscillations in the neutral kaon system, it was proposed that the same thing could occur in the neutral lepton sector. The states that would oscillate in that scenario were the particle and anti-particle (or helicity) states for a single flavor of neutrino. In the present search, this particular mode is not addressed.

The change of basis from the (weak eigenstate) creation and detection basis to the (mass eigenstate) propagation basis is represented by transformation via a unitary matrix, \mathcal{M} , and one writes:

$$\begin{pmatrix} \nu_1 \\ \nu_2 \\ \nu_3 \end{pmatrix} = \begin{pmatrix} \mathcal{M}_{1,e} & \mathcal{M}_{1,\mu} & \mathcal{M}_{1,\tau} \\ \mathcal{M}_{2,e} & \mathcal{M}_{2,\mu} & \mathcal{M}_{2,\tau} \\ \mathcal{M}_{3,e} & \mathcal{M}_{3,\mu} & \mathcal{M}_{3,\tau} \end{pmatrix} \begin{pmatrix} \nu_e \\ \nu_\mu \\ \nu_\tau \end{pmatrix} \quad (1.1)$$

where $\nu_i, i = 1 - 3$ are the mass eigenstates, and $\nu_j, j \in \{e, \mu, \tau\}$ are the flavor eigenstates.

Under the assumption that the $(3,e)$ and $(3,\mu)$ elements of \mathcal{M} are small, (meaning physically that the ν_e and ν_μ states are not strongly coupled to the ν_τ state) the equation reduces to a two-state problem decoupled from a stationary

state, and one can write simply:

$$\begin{pmatrix} \nu_e \\ \nu_\mu \end{pmatrix} = \begin{pmatrix} \mathcal{M}_{1,e}^* & \mathcal{M}_{2,e}^* \\ \mathcal{M}_{1,\mu}^* & \mathcal{M}_{2,\mu}^* \end{pmatrix} \begin{pmatrix} \nu_1 \\ \nu_2 \end{pmatrix} \quad (1.2)$$

Such a matrix can be parameterized as:

$$\begin{pmatrix} \mathcal{M}_{1,e}^* & \mathcal{M}_{2,e}^* \\ \mathcal{M}_{1,\mu}^* & \mathcal{M}_{2,\mu}^* \end{pmatrix} = \begin{pmatrix} \cos(\theta)e^{-i\delta} & -\sin(\theta)e^{i\delta} \\ \sin(\theta)e^{i\delta} & \cos(\theta)e^{-i\delta} \end{pmatrix}$$

The one further assumption to simplify this is (mathematically) that the matrix can be made real, meaning physically that there is no CP violation in the effect.¹ For Dirac neutrinos in two flavor mixing, there can be no CP violating terms, so the assumption of no CP violation here (since 2-flavor mixing is already assumed) is equivalent to the assumption that the neutrinos are Dirac particles. Although the following steps of algebra are written out in several books (for example: [2, 3, 4]) it is useful to retrace them here for completeness. For the specific problem studied here, a beam of essentially pure ν_μ is produced, and

¹To see that the imaginary terms do represent CP violation, one can retrace the following steps of algebra keeping the imaginary parts, and see that terms varying as the sine of time appear. Since this function is odd in time, by the CPT theorem, there must also be CP violation.

oscillation is only detectable by the appearance of ν_e . The beam momentum is tens of MeV or more, and the presumed masses (because of independent cosmological constraints) are at most of order tens of eV.

In propagation, the ν_μ beam is initially $\begin{pmatrix} \sin(\theta) \\ \cos(\theta) \end{pmatrix}$, and since it is not in an eigenstate of the propagation (energy) operator, it time evolves as $\begin{pmatrix} e^{i\frac{E_1 t}{\hbar}} \sin(\theta) \\ e^{i\frac{E_2 t}{\hbar}} \cos(\theta) \end{pmatrix}$. Here, $E_{1,2}$ is the energy of the component state 1 or 2. At the detector, after time t , measurement corresponds to the amplitude:

$$\begin{aligned} \begin{pmatrix} 1 & 0 \end{pmatrix} \mathcal{M}^\dagger e^{i\frac{\hat{E}}{\hbar}t} \mathcal{M} \begin{pmatrix} 0 \\ 1 \end{pmatrix} &= \cos(\theta) \sin(\theta) \left(e^{i\frac{E_2 t}{\hbar}} - e^{i\frac{E_1 t}{\hbar}} \right) \\ &\approx \cos(\theta) \sin(\theta) e^{i\frac{pct}{\hbar}} \left(e^{i\frac{(m_2 c)^2 t}{2p\hbar}} - e^{i\frac{(m_1 c)^2 t}{2p\hbar}} \right) \\ &= \sin(2\theta) e^{i\frac{pct}{\hbar}} e^{i\left(\frac{\sum_{j=1,2} m_j^2 c^2 t}{2p\hbar}\right)} \sin\left(\frac{(m_1^2 - m_2^2)}{2p\hbar} c^2 t\right) \end{aligned}$$

where, since the mass is very small compared to the momentum, I have expanded $E = \sqrt{(pc)^2 + (mc^2)^2} \approx pc + \frac{m^2 c^2}{2p}$. Squaring to get a probability of measurement:

$$\text{Prob}(\nu_\mu \rightarrow \nu_e) = \sin^2 2\theta \sin^2 \left(\frac{c}{2\hbar} \Delta m^2 \frac{ct}{p} \right)$$

$$= \sin^2 2\theta \sin^2 \left(1.27 \Delta m^2 \frac{L}{E} \right) \quad (1.3)$$

where Δm^2 is expressed in eV^2 , L in meters, and E in MeV (or L in kilometers and E in GeV).

The measurable parameters are $\sin^2 2\theta$ and Δm^2 . (*I.e.*: the separate masses are not detectable in such an experiment, only the difference of their squares.) CPT invariance requires that the amplitude for $\bar{\nu}_\mu \rightarrow \bar{\nu}_e$ is the same as for $\nu_e \rightarrow \nu_\mu$. The assumption of no CP violation further requires that the amplitudes for oscillation between ν_μ and ν_e are the same as for between $\bar{\nu}_\mu$ and $\bar{\nu}_e$ *in either time order*, and in the limit that this assumption is correct, experimental limits on one process can be applied to the other. This also allows combination of data from oscillation searches in the $\bar{\nu}_\mu \rightarrow \bar{\nu}_e$ and $\nu_\mu \rightarrow \nu_e$ channels. (This is done in this work, but first separate limits are presented which do not rely on the assumption CP conservation.) ²

The theoretical framework just presented is the basis of

²A review of the theoretical aspects of CP violation is presented on pages 33ff of reference[5], noting why it is expected that if there is any CP violation in the neutrino sector it is small. The argument involves experimental limits on neutrinoless double beta decay, so quantitatively stronger statements are possible since the publication of that work, but the analysis is the same

the analysis done in this work. While a fuller treatment, allowing mixing among all three generations and CP violation is possible, limits presented with the assumptions stated above are relevant in their own standing, and facilitate the comparison of experiments by making the excluded parameter region “visual”.

1.2 Neutrino masses and the standard model

A question regarding the motivation for the previous discussion naturally arises: If all neutrinos are “left-handed”, isn’t a non-zero neutrino mass forbidden? There are two answers to this query: First, the observation that all neutrinos are “left-handed” may be only an approximation, good at some level indicative of the mass value. Second, there are possible mass terms in particle physics that would confuse the definition of particle and anti-particle in such a way that the right-handed neutrino is observed as an anti-neutrino.

1.2.1 “Normal” mass terms

All neutrinos that have been observed in charged current weak interactions are “left-handed.” If neutrinos have mass, left-handed neutrinos may be converted into right-handed neutrinos by a Lorentz boost. The couplings of the two to the weak charged current, however, need not be the same, as in the standard model the left- and right-handed electron do not couple to the W the same way. Consider the case where the right-handed neutrino is, like the right-handed electron, a singlet under the action of the weak $SU(2)$ symmetry. In the electron family, the representations of weak $SU(2)$ are then:

$$\begin{pmatrix} \nu_e \\ e^- \end{pmatrix}_L \quad (e^-)_R \quad (\nu_e)_R \quad (1.4)$$

Note that the only addition to the standard model is the right-handed neutrino, and this has no coupling to the charged current. The only way to create a right-handed neutrino by charged current processes in this case is to create a (normal) left-handed neutrino in a reference frame that is Lorentz boosted with respect to the laboratory

frame. If the neutrino mass is very small compared to the production energy, the boost needed to “flip” the apparent spin is large. In principle, the experiment that one would need to do to detect this apparent loss of neutrinos can be done. Since neutrino detection cross sections are so small (and not so very well known), the experiment is difficult, and while no conclusive evidence for the occurrence of this phenomenon exists, it is not strongly ruled out.

Another perplexing facet of this scenario is why the neutrino mass should be so much smaller than the masses of the charged leptons. Kinematic measurements of neutrino mass from observing beta decays imply that the dominant mass state component of the electron neutrino is at least four orders of magnitude lighter than the electron [3]. If the neutrino mass is generated outside the standard model in the same way as the electron mass this is a puzzle for theorists.

1.2.2 Other possible mass terms

The discussion that follows is given in more detail in chapter 5 of reference [3]. It is a somewhat formal treatment of mass terms in field theory and describes a way (outside of the standard model) mass might be generated for neutrinos in a different way than it is generated for charged leptons and quarks.

The general appearance of mass in the standard model particle Lagrangian is in terms $\bar{\psi}m\psi$. Lorentz invariance and Hermiticity of the lagrangian restrict the form of possible mass terms, however, other forms are possible. The possible bilinear terms in fields are:

$$\bar{\psi}m_D^{(1)}\psi, \bar{\psi}^cm_D^{(2)}\psi^c, \bar{\psi}^cm_M\psi, \bar{\psi}m_M^*\psi^c$$

for a field ψ and its CP conjugate ψ^c . Hermiticity of the Lagrangian requires that the first terms, if they appear, have m real, and that the second pair of terms, if they appear, occur together with the (possibly complex) “masses” the complex conjugates of each other; in fact, the two terms are not really distinct since each is the adjoint of the other. In a CP invariant theory, the two M_D are

the same, and there are only two independent terms here (but note each is of a two component object). (The subscripts “D” and “M” are used to suggest the connection to “Dirac” and “Majorana” mass terms. For the present discussion, however, it is only necessary that they are distinct real constants.)

It is useful to write the fields in terms of chiral projections: $\phi_{L,R} \equiv \left(\frac{1 \pm \gamma_5}{2}\right) \phi$ noting that $\bar{\chi}_L \phi_L = 0$ for any fields χ, ϕ . Also: $(\psi_{L,R})^c = (\psi^c)_{L,R}$ since the operation CP will reverse the chirality. In terms of the left and right chiral projections of the fields the distinct mass terms are:

$$\bar{\psi}_L \psi_R, \bar{\psi}^c_R \psi_L, \bar{\psi}^c_L \psi_R \quad (1.5)$$

(and their hermitian conjugates).

There are then three constants with the dimension of mass needed for the free field Lagrangian for the four component fields. If one write the fields as:

$$n_1 \equiv \frac{\psi_L + (\psi_L)^c}{\sqrt{2}}, \quad n_2 \equiv \frac{\psi_R + (\psi_R)^c}{\sqrt{2}}$$

the entire free field Lagrangian can be written:

$$\begin{aligned}
-\mathcal{L}_{free} = & (\overline{n_1}, \overline{n_2}) \gamma_\mu \partial^\mu \begin{pmatrix} n_1 \\ n_2 \end{pmatrix} \\
& + (\overline{n_1}, \overline{n_2}) \begin{pmatrix} M_L & M_D \\ M_D & M_R \end{pmatrix} \begin{pmatrix} n_1 \\ n_2 \end{pmatrix}
\end{aligned} \tag{1.6}$$

Denoting the fields that form the basis that diagonalizes the above “mass matrix” as ν_m , N_m , one sees that this is the free field Lagrangian for two independent particles with different masses. (The subscript m is put in to make explicit that these states are the mass eigenstates, not necessarily the flavor eigenstates.) Equation 1.6 can then be rewritten:

$$\begin{aligned}
-\mathcal{L}_{free} = & (\overline{\nu_m} \gamma_\mu \partial^\mu \nu_m + m_{\nu_m} \overline{\nu_m} \nu_m) \\
& + (\overline{N_m} \gamma_\mu \partial^\mu N_m + m_{N_m} \overline{N_m} N_m)
\end{aligned}$$

Each field has only two degrees of freedom (since the original Dirac spinor of which this is a generalization had 4 components) corresponding to two spin states. Also, the two fields n_1 , n_2 from which these two particles are constructed are CP eigenstates with degenerate eigenvalues, so each of ν , N are their own CPT conjugate.

For the present work, it is enough to say that mass terms are possible for neutrinos. However, it is useful to briefly present a mechanism for their generation to show that one does not need to go too far afield from the standard model of electro-weak interactions to find them. A useful class of extensions to the standard model is the so-called “left-right symmetric models”. In these theories, the usual weak charged current interaction still exists, operating on the multiplets shown in 1.4 via the usual W , now called “ W_L .” In addition, there is a new interaction mediated by the “ W_R ” which acts on multiplets:

$$\begin{pmatrix} \nu_e \\ e^- \end{pmatrix}_R \quad (e^-)_L \quad (\nu_e)_L$$

The full symmetry group of the theory is then

$$SU(2)_L \times SU(2)_R \times U(1).$$

Since at the energy scale of current accelerators the observed electroweak symmetry is only $SU(2)_L \times U(1)$, the $SU(2)_R$ symmetry must be broken at some higher scale. The spontaneous symmetry breaking of the $SU(2)_R$ symmetry at that scale (corresponding to the vacuum expect-

tation value of a scalar Higgs field) gives the W_R a mass of order the symmetry breaking energy scale. Since no effects of interactions via W_R are observed, this is expected to be large. (Note that this is *not* just from observations in the neutrino sector. Limits on the $m_{K_L^0} - m_{K_S^0}$ mass difference require that $m_{W_R} > \mathcal{O}(\text{TeV})$.)

The exact values expected for the mass matrix parameters in this model would depend on more detail than is given here, but in general one expects that since m_{W_R} , M_R will also be large. Also, since M_D is generated by the same mechanism as the charge lepton and quark masses, one expects $M_D \approx \mathcal{O}(m_{l, \text{ or } q})$ for the charged lepton or quark of the same generation. The arguments for a value of M_L involve observations of neutral current neutrino scattering, but on general “aesthetic grounds” one might expect that since it is the diagonal term for the “regular” neutrino mass, it must be small compared to the other terms. (The more rigorous arguments make it quite plausible that it is identically 0.)

For a mass matrix of the form in equation 1.6:

$$\mathcal{M} = \begin{pmatrix} M_L & M_D \\ M_D & M_R \end{pmatrix} \approx \begin{pmatrix} 0 & M_D \\ M_D & M_R \end{pmatrix} \quad (1.7)$$

if $M_R \gg M_D$ the eigenvalues are $m_{N_m} \approx M_R$ and $m_{\nu_m} \approx -\frac{M_D^2}{M_R}$. The negative mass eigenvalue can be avoided by considering the field $\gamma_5 \nu_m$ rather than ν_m . The result is a neutrino with a non-zero mass, the scale of which is set separately from that of the charged leptons, but predicted to be much smaller, and a new neutral lepton with a very large mass. The price for such a theory is the introduction of the new symmetry breaking Higgs fields and the new heavy neutral lepton. The mass relation derived (assuming universality of the $SU(2)_R$ coupling so that there is only one M_R) leads to a relation like: $m_{\nu_l} \approx \frac{m_l^2}{M_R \approx 10^{12-20} \text{eV}}$, so that

$$m_{\nu_e} : m_{\nu_\mu} : m_{\nu_\tau} :: m_e^2 : m_\mu^2 : m_\tau^2 :: 1 : 4 \cdot 10^4 : 10^7$$

For $m_{\nu_\tau} \approx 30\text{eV}$, which is a “cosmologically interesting” value, this would make $m_{\nu_\mu} \approx \mathcal{O}(0.1\text{eV})$, a value too small to be measured by LSND in the case that the heaviest neutrino is not strongly coupled to the electron and

muon neutrino. The case is made, however that there are mechanisms for the generation of small neutrino masses in relatively minor amendments to the standard model.

There are in fact other forms of amendments to the standard model to generate non-zero masses for the neutral lepton sector. The above case is presented only as an example to show that the idea is not too far afield from what is currently “standard.” In general, the introduction of neutrino mass terms requires the introduction of new neutral leptons, new Higgs fields, or both.

1.3 Some history; Previous related work

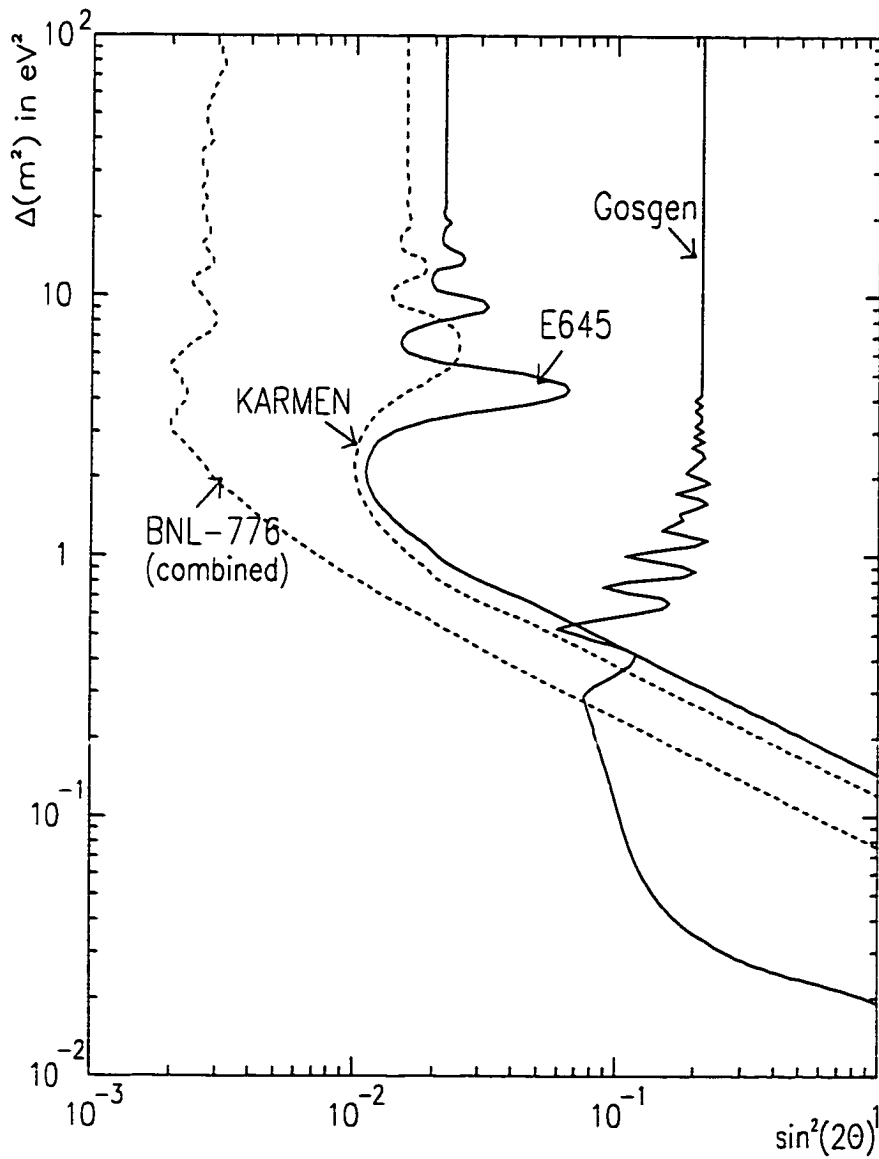
Previous experiments at accelerators and reactors have searched for neutrino oscillations in one or both of the channels studied in this work. Some existing limits on neutrino oscillation parameters are shown in figure 1.1. In particular, a previous experiment at LAMPF (E645) used some of the same equipment restored for LSND. It searched the same region of parameter space for $\bar{\nu}_e$ appearance in a $\bar{\nu}_\mu$ beam. KARMEN, (the **K**Arlsruhe-**R**utherford

Medium Energy Neutrino experiment) a currently running competitor of LSND, published the result shown here in 1994, but in later publication strengthened their limit to the one shown in figure 7.9. The experiment uses a proton beam on a heavy metal target to produce neutrinos from pion and muon decay at rest. The detector sits approximately 18m from the source. The BNL-E776 result shown here is for the combined $\nu_\mu \rightarrow \nu_e$ and $\bar{\nu}_\mu \rightarrow \bar{\nu}_e$ presentation published by that collaboration, but weaker limits from that group may be more robust [6]. The experiment was an accelerator experiment with a neutrino beam from pion decay. The average neutrino energy was approximately 1GeV, and the detector was 1km from the source. By running alternately with π^\pm the experiment was able to search for both $\nu_\mu \rightarrow \nu_e$ and $\bar{\nu}_\mu \rightarrow \bar{\nu}_e$. Gösgen is a reactor experiment looking for ν_e disappearance. It is continuing to produce stronger limits, but will never probe very low in $\sin^2 2\theta$.

This list of previously existing limits is not intended to be complete. With the exception of the previous LAMPF

experiment (which is put in only because it is basically a direct ancestor of LSND) the limits shown are the ones that will be directly relevant to how much new ground is covered in this work. BNL-E776 excludes the lowest values of $\sin^2 2\theta$, and Gösgen excludes lower values of Δm^2 than any of the others. The later result of KARMEN excludes a small region allowed by both of those experiments. The result presented in this work will surpass both the Brookhaven and KARMEN limits, providing a new bound in the region of parameter space $\Delta m^2 > \mathcal{O}0.1\text{eV}^2$.

Figure 1.1: Previous limits in the range of parameter space studied in this work. In each case the region above and to the right of the curve is “excluded” (i.e.: ruled out by the experiment) at the 90% confidence level. The text explains more about the experiments.



Chapter 2

The LAMPF neutrino beam

Los Alamos Meson Physics Facility (LAMPF) operated the 800MeV pulsed beam proton accelerator at 1mA of beam current in 1994. The protons are deposited on a number of targets, and finally a water cooled copper beam dump. In each of these components, they produce pions which subsequently decay (predominantly) to muons. Neutrinos from pion and muon decays comprise the beam for LSND.¹

¹A very small component of the beam comes from kaon production, and, while this process is included in the beam Monte Carlo and its contributions implicitly included in the distributions from that, such details are suppressed in the following discussion.

2.1 Physical configuration of the beam area

LAMPF accelerates protons to 800MeV kinetic energy in approximately 1/4 ns wide bunches every 4.96ns controlled by the 201.25MHz RF cavity. These “micro-pulses” ride on a structure of square waves, on for 650 μ s and then off for 7.7ms (120Hz). The numerical values of these parameters (except the RF frequency) were changed from time to time for various tests by the accelerator staff, but not the general scheme. A schematic drawing of this time structure is shown in figure 2.1. It is important to realize that the designation “beam on” for an event refers to one occurring at any time within the macropulse and until 10 μ s after (to account for the lifetime of the muon).² There are, of course, nuclear processes occurring in the beam stop and surrounding material that far outlive any time structure in the beam. For the purposes of background estimation in this experiment, they are equivalent

²Attempts to measure within the fine timing of the micropulses have been successful at some level with the large statistics measurement of the cross section of $\nu_\mu C \rightarrow \mu X$, [7] but are not refined enough to be used for the decay-in-flight oscillation search. Timing on such a scale is irrelevant to the decay at rest beam.

to cosmic rays or ambient radioactivity.

There are 3 targets in the proton beam line and a copper beam dump that all contribute to the neutrino flux at LSND. The two upstream targets (called A1 and A2) are carbon of 3 to 10cm thickness, depending on the running period. These degrade the average proton energy by only about 20 MeV, but more importantly, reduce the flux of protons by about 20%. The main target (nearest LSND) is the A6 water target. It is an oblong steel enclosure 30cm long full of water with several steel inserts to manage the water flow. There are also some small isotope production “stringers” along the line between the A6 water target and the beam dump. These are of very low mass and do not substantially affect the total neutrino flux, although their metal cases do contribute significantly to π^- production. The A1 target is about 120m from LSND’s center, A2 at 100m, and A6, from which the greatest flux comes, 30m. The beam dump, sitting 29m from the detector center, is made of plates of copper with water coolant running between. This is where 97.5% of pions from the A6 water

target come to rest and decay. The detector sits at an angle of 7.7° from the direction of the proton beam line, its cylindrical axis pointed approximately at the beam dump, but a few meters lower. A diagram of the path from A6 to LSND is shown in figure 2.2, and a map of the whole area in 2.3.

2.2 Processes for neutrino production

³About 85% of the charged pions produced in the A6 area are π^+ . Since by far most π^- capture in nuclei in the material of the targets or the beam dump, about 97.5% of the charged pions that decay are positive, and, since μ^- capture also, only approximately $7 \cdot 10^{-4}$ of the muons that decay are negative. Since π^+ decay is to $\nu_\mu \mu^+$ over 99.98% of the time, the neutrinos of from pion decay at rest are 29MeV ν_μ which is too low an energy to participate in charged current interactions. Those from pions decaying

³A first order estimate of the pion yields and of the pion decay-in-flight neutrino spectrum is made in appendix B. This chapter presents the results of full Monte Carlo simulations of the beam fluxes. The quasi-analytic arguments presented in the appendix are meant to elucidate the physics of neutrino beam production, and are not used for the expected event rate calculations presented later.

in flight, however, have sufficient energy to produce muons in the detector which have been the subject of two earlier theses from LSND[8],[7], and are the beam for one of the two oscillation searches that are the material of this thesis.

The A6 water target is only about 1.5 meters from the copper beam dump and the muon lifetime is $\frac{658\text{m}}{c}$ in the rest frame, so while some pions decay in flight, virtually all μ^+ come to rest in the beam stop and decay there. There are, therefore, two distinct useful beams: one of ν_μ from pions decaying in flight, and another of $\bar{\nu}_\mu$ from muons decaying at rest. Hereafter, these two beams will be referred to simply as “decay-in-flight” and “decay at rest”.

The beam Monte Carlo [9] for the LAMPF neutrino beam originally used measured pion fluxes from a previous experiments at LBL. This single measurement was the basis for the flux calculations for the earlier neutrino experiments at LAMPF. The pion flux distributions as a function of direction were measured in an experiment to improve the precision of the monte carlo predictions, [10]. The calculated kinetic energy spectrum for the pions pro-

duced in A6 extends to around 500MeV, and the resulting ν_μ energies therefor go up to about 300MeV. When looking at background, it will be important to note that the ($\mathcal{O}(10^{-4})$ of) ν_e produced via $\pi^+ \rightarrow \nu_e e^+$ are much higher in energy than the ν_μ made in the more common decay (for both processes from pions at rest). The decay-in-flight neutrino spectra for the four neutrino types ($\nu_e, \bar{\nu}_e, \nu_\mu, \bar{\nu}_\mu$) from pion decay in the A6 target area are shown in figures 2.5. (The fluxes shown are average fluxes calculated on a grid of 25 points throughout the tank. Event rate calculations done later for the signal expected use the local rates.) The Monte Carlo has also been used to calculate the decay-in-flight of pions from A1 and A2, and muon decay-in-flight from each source.

The decay of $\mu^+ \rightarrow \bar{\nu}_\mu \nu_e e^+$ is well understood theoretically [11], and the positron spectrum from this decay is well measured. (In fact, electrons from cosmic muon decay are the main source of data for the energy calibration presented later in section 4.1.2) The “Michel parameterized”

spectrum for a lepton momentum P_l is written

$$Prob(P_l = E) = \frac{E^2}{(E_0)^4} \left(12 \cdot (E_0 - E) + 8\rho \cdot \left(\frac{4}{3}E - E_0 \right) \right) \quad (2.1)$$

The diagram for muon decay is shown in figure 2.4. The “Michel parameter” ρ (sometimes ω in the literature [11]) is predicted to be $\frac{3}{4}$ for the positron and the $\bar{\nu}_\mu$, and 0 for the ν_e . (Effects of electron mass are too small to be measured in our experiment, and are ignored in later fits to this theoretical spectrum.)

$$\Rightarrow \frac{\partial \Phi(\bar{\nu}_\mu)}{\partial E_l} = x^2(6 - 4x) \left(\frac{1}{E_0} \right) \quad (2.2)$$

$$\frac{\partial \Phi(\nu_e)}{\partial E_l} = 12x^2(1 - x) \left(\frac{1}{E_0} \right) \quad (2.3)$$

These curves (together with the line spectrum representing ν_μ from π^+ decay at rest) are shown in figure 2.6. It is important to note that this is the produced neutrino spectrum, and that most relevant cross sections (for detection processes) are rising quadratically in this energy range. Hereafter, electrons from muon decay will often be referred to simply as “Michel electrons”.

2.3 The beam Monte Carlo

The beam Monte Carlo for the LAMPF neutrino beam is a collection of code local to the LSND collaboration[9]. It uses pion production cross sections and transport parameters from LAMPF E866[10].⁴ The decay at rest spectra for pions and muons are well known theoretical distributions; pion decay-in-flight involves only a Lorentz boost from this. Therefore, the main predictions from the beam Monte Carlo are the total flux at each target, and relative number of pions decaying in flight or at rest. The ν_e $^{12}\text{C} \rightarrow ^{12}\text{N}(\text{g.s.})e^-$ cross section is well measured [12], and so data for this process in the decay at rest energy range provides a good calibration of the total flux. Similarly, the decay-in-flight spectrum could be calibrated by the observation of ν_μ $^{12}\text{C} \rightarrow ^{12}\text{N}(\text{g.s.})\mu^-$, but in this case the total number of expected events (assuming reasonable detection efficiency) is only 15. A cursory analysis finds 13, which is very good agreement, but the errors are too

⁴The KARMEN collaboration uses essentially the same code for their beam monte carlo. It was written by a mutual collaborator with the plan that it would serve both experiments.

large to call this a calibration.

2.4 The neutrino beam spectra, a synopsis

The decay at rest beam for this experiment has a firmly predicted theoretical spectrum. The overall flux for neutrinos from muon decay at rest is calculated by Monte Carlo. The decay-in-flight beam has components from the A6 water target, and from the A1 and A2 carbon targets. These latter contribute significantly to beam contamination for the decay-in-flight oscillation search.

Both to accommodate adequate shielding from the beam stop area, and to give sensitivity to lower values of Δm^2 , the center of LSND is 30m from the A6 target area.

Figure 2.1: The timing structure of the LAMPF proton beam. There are approximately $1.3 \cdot 10^5$ micro-pulses in a macro-pulse. Times are designated as “beam on” for the duration of the macro-pulse, and $15\mu\text{s}$ after. The delay time in the tag is to account for the $2.2\mu\text{s}$ muon lifetime.

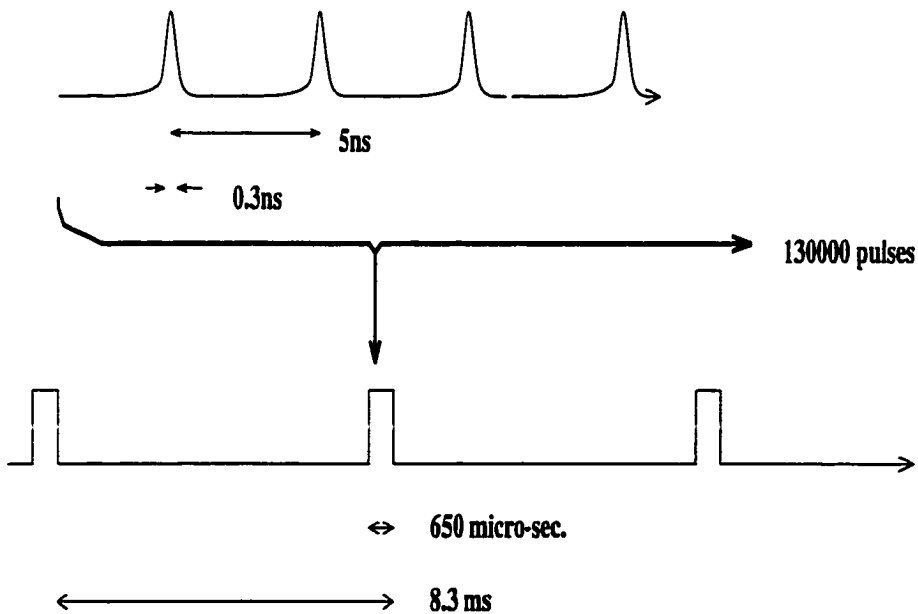


Figure 2.2: The relative position of the detector and beam.

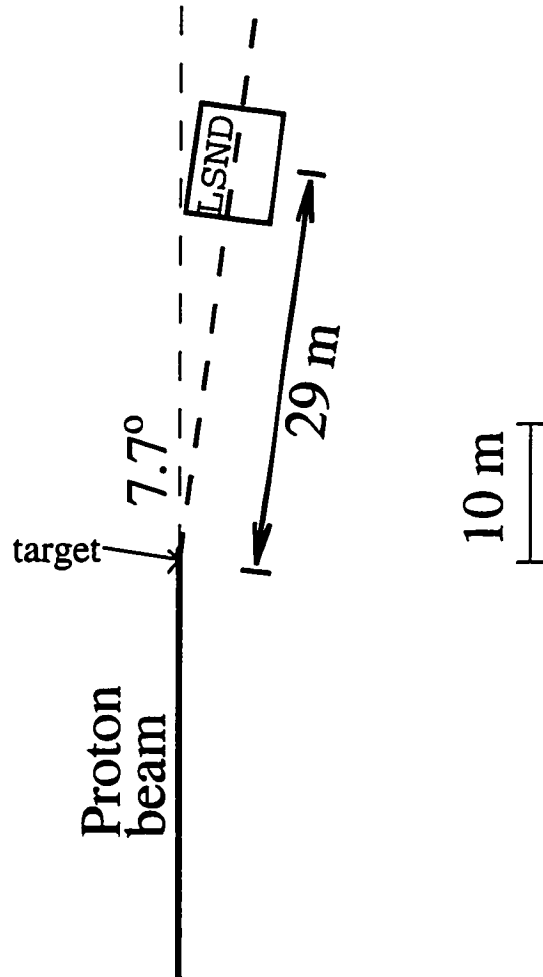


Figure 2.3: The whole LAMPF area. This figure is taken directly from [16]. The rectangle labelled "Neutrino Detector" in the middle right represents LSND, and the dotted line to it the path of the neutrino beam.

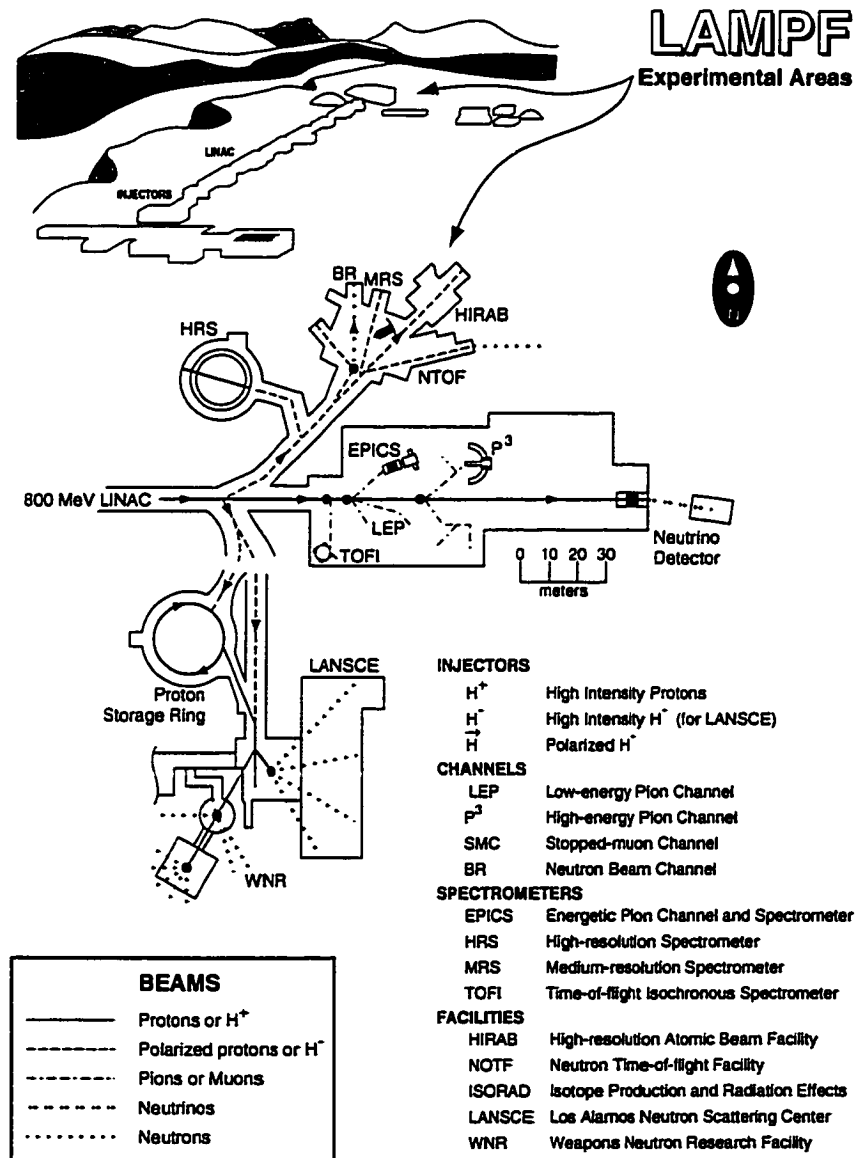


Figure 2.4: Feynman diagrams for μ -e scattering and for muon decay (Time increases to the right.)

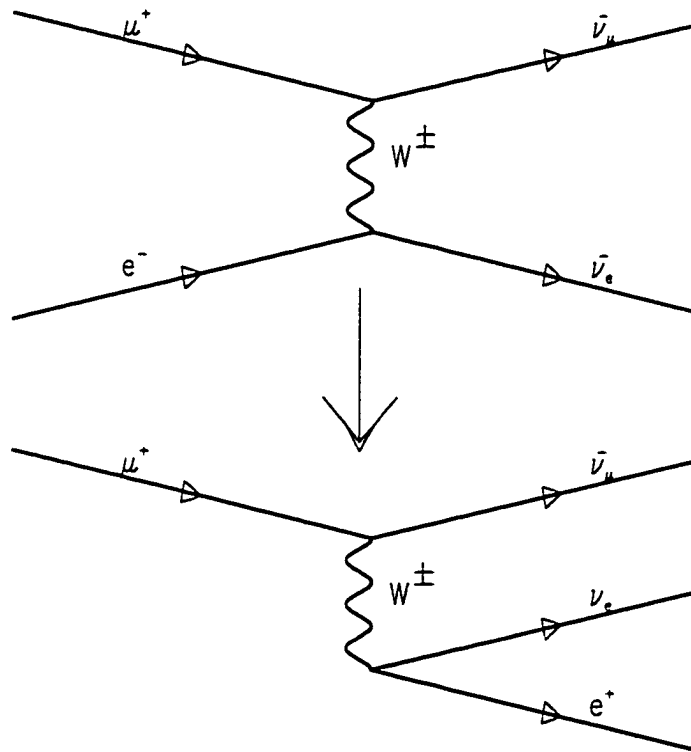


Figure 2.5: Monte Carlo calculated decay-in-flight neutrino fluxes for ν from pion decay in the A6 target box. The overall normalization is arbitrary here, but the relative normalization between the plots is calculated by the program. The various fluxes are calculated at a grid of points within LSND, and here averaged. Note the change in energy scale for the ν_e spectra.

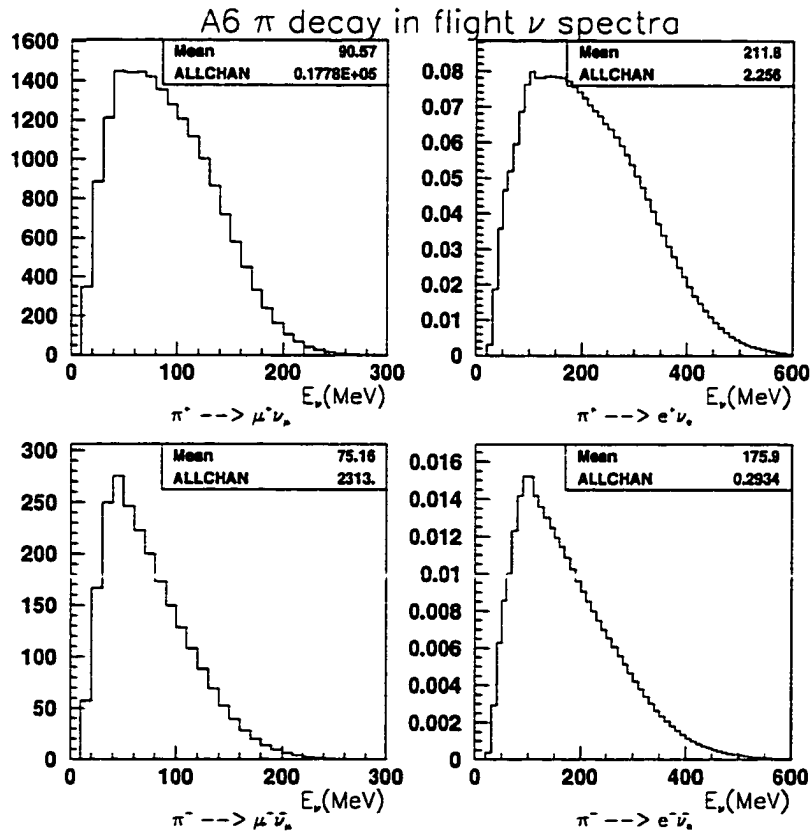
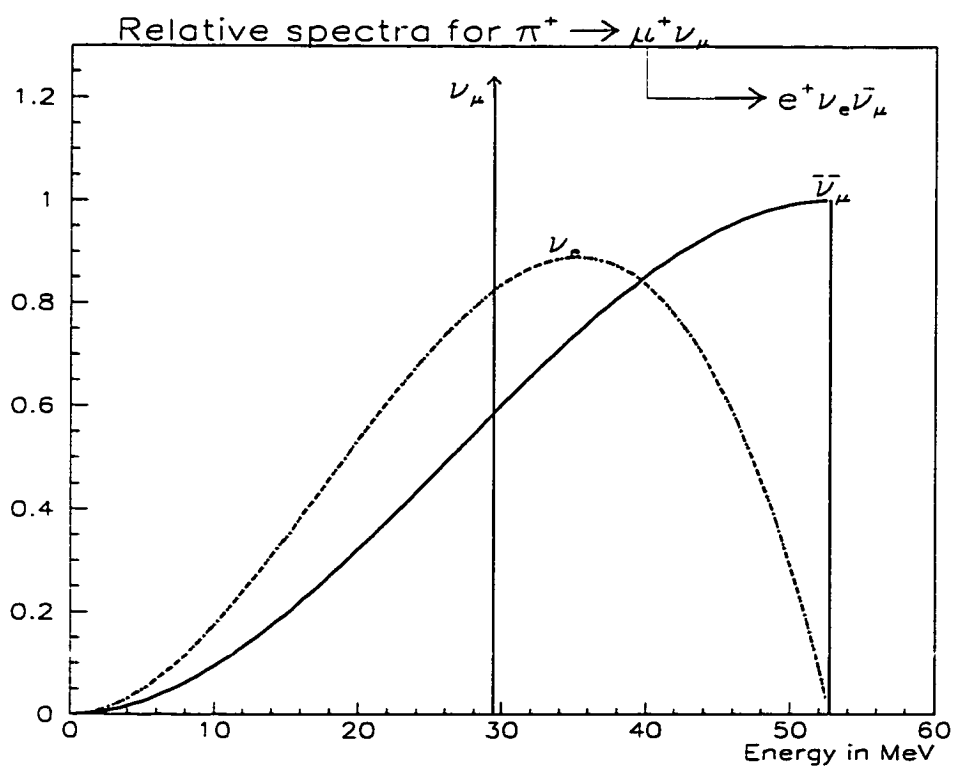


Figure 2.6: Theoretical neutrino production spectra for muon and pion decay-at-rest[11]



Chapter 3

The Liquid Scintillator Neutrino Detector, LSND

3.1 Charged particle detection for neutrino physics

Neutrino detection is only through the detection of electromagnetically interacting products of their interactions. The family of the lepton produced in a weak charged current process is the signature for the flavor of the interacting neutrino. Since the cross sections for weak processes at the LAMPF neutrino beam energy are low ($\mathcal{O}(10^{-40}\text{cm}^2)$), a large active volume is necessary for detection of these interactions. The desire to reuse existing hardware (specifically, the veto shield from LAMPF E645) provided an upper

limit on the size of LSND. To tag the neutrino flavor for an oscillation search, particle identification is necessary.

Two detector types that have successfully measured neutrino interactions are imaging liquid Čerenkov detectors, and scintillator detectors. LSND combines the features of the two types by dissolving a small amount of liquid scintillator in mineral oil, which acts also as a passive medium for the creation of Čerenkov radiation. The scintillator allows detection of particles below Čerenkov threshold. This mixture of isotropic scintillator light for all charged particles with directed light for relativistic charged particles provides the basis for particle identification discussed in section 4.3.

3.1.1 Čerenkov detection with mineral oil

Čerenkov radiation was used in detection of charged particles for neutrino physics in earlier experiments. Large water Čerenkov detectors have observed both atmospheric and solar neutrinos in Kamioka and in IMB. Mineral oil (essentially CH_2) has an advantage over water for Čerenkov

detection of low energy charged particles because its index of refraction is somewhat higher (1.5 compared to 1.33). This results in many more Čerenkov photons per MeV for radiating particles, and a lower threshold.¹ The low threshold is a useful feature for calibrating the muon energy scale. The enhanced light output helps in reconstruction (see section 4.2.1). Another advantage is that there are scintillators that are soluble in mineral oil.

3.1.2 Liquid scintillator and charged particle detection

Previous accelerator neutrino experiments at BNL have used liquid scintillator detectors. Detectors using scintillation light detection for charged particles are noted for excellent calorimetry. However, since scintillation light is isotropic, reconstruction of the direction of a particle track in a pure scintillation detector is only possible for long tracks, or in segmented detectors, and even then the an-

¹The energy radiated per unit length for emission of Čerenkov radiation is

$$\left(\frac{dE}{dx}\right)_{\text{rad}} = \left(\frac{e}{c}\right)^2 \int_{n(\omega) > (1/\beta)} \omega \left(1 - \left(\frac{1}{\beta n}\right)^2\right) d\omega \quad (3.1)$$

[13]

gular resolution is not as good as for Čerenkov detectors².

3.1.3 Combining Čerenkov and scintillator detectors

By using a dilute liquid scintillator dissolved in mineral oil, the advantages of both Čerenkov and scintillator detectors are available. LSND uses 0.031 g/liter of Butyl PBD scintillator to get about 4 times as much scintillation light as Čerenkov light for $\beta \approx 1$ particles. This allows detection of low energy muons and protons below Čerenkov threshold, while still providing information for angular reconstruction of relativistic particles, and giving data for particle identification via the ratio of isotropic scintillation light to directed, prompt light in the Čerenkov cone.

LSND is an approximately cylindrical tank 8m long and just over 5m in diameter with its cylinder axis pointing (almost) toward the A6 beam target. It holds 157m³ of mineral oil with dissolved scintillator which is viewed by 1220 8” Hamamatsu photo-multiplier tubes (hereafter PMTs). The PMTs cover 25% of the surface area, and except for

²The angular resolution for electrons at 50MeV in LSND is $\sim 10^\circ$. (For details on the angular reconstruction algorithm, see section 4.2.1.)

three very small cables running to $\frac{1}{2}$ liter flasks for the laser system described in section 4.1.1, have no obstructions between them and the active volume.

3.2 Passive shielding of the detector

Since neutrino interactions have small cross sections, the event rates expected in LSND are low. Cosmic rays and low energy gamma radiation from ambient materials have very high rates, so much shielding is necessary to detect neutrino interactions. One approach to solving this problem is to put the detector far underground. While this is reasonable for studies of solar and atmospheric neutrinos, it is impractical for an experiment like LSND with its source fixed above ground and providing a limited flux falling as $\frac{1}{r^2}$.

It is useful to consider the rates of neutrino events and cosmic rays in LSND.

The total number of carbon nuclei in the region of the detector viewed by the PMTs is approximately $5.5 \cdot 10^{30}$. An important process for ν_e onto C is $\nu_e \ ^{12}\text{C} \rightarrow \ ^{12}\text{N}(\text{g.s.})e^-$.

This process has a firmly predicted cross section which has been verified at the KARMEN experiment and accounts for approximately 50% of the total cross section for ν_e on carbon at LAMPF beam energies. (This process is used as a verification of the normalization of the beam flux predicted by the Monte Carlo, and also constitutes a background to the $\bar{\nu}_\mu \rightarrow \bar{\nu}_e$ search.) Taking the cross section of this process at 40MeV leads to:

$$\begin{aligned} 5.5 \cdot 10^{30} \cdot 10^{-41} \text{cm}^2 &= 5.5 \cdot 10^{-11} \text{cm}^2 \\ &= 5.5 \cdot 10^{-15} \text{m}^2 \text{ detector effective area} \end{aligned} \quad (3.2)$$

For $6000\text{C} \approx 3.7 \cdot 10^{22}$ protons (the extent of the 1994 run) of beam, with an effective neutrino yield around 9%, the expected total number of these events in this detector 30m from the beamdump is then:

$$\left(\frac{5.5 \cdot 10^{-15}}{4\pi \cdot 30^2} \right) \cdot 3.4 \cdot 10^{21} \approx 2 \cdot 10^3 \quad (3.3)$$

which does *not* take detection efficiency into account. Using a reasonable detection efficiency of approximately 10%, and assuming only 75% of the volume viewed by the PMTs is useful, one expects $\mathcal{O}(150)$ events from this process to

be detected in LSND.

On the other hand, the number of cosmic ray muons that cross the midplane of the tank in the same time is:

$$\underbrace{\left(2.2 \cdot 10^2 \frac{\mu}{s \cdot m^2}\right)}_{\text{cosmic muon rate[14]}} \cdot \underbrace{50m^2}_{\text{appr. area of tank midplane}} \cdot 10^7 \text{sec} \approx 3 \cdot 10^{11} \quad (3.4)$$

This potential ratio of signal to noise makes it necessary to use as much shielding as possible. LSND is covered by approximately $2 \frac{\text{Kg}}{\text{cm}^2}$ of shielding in the ambient rock and large steel shielding blocks on top.³ The estimated rate of entering cosmic rays is 4KHz, [15] about a factor of three below the above estimate. These same arguments that demand the use of as much passive shielding as possible necessitate both the use of an active veto system to reject cosmic rays on-line and the writing of histories of events of interest so that further off-line rejection can be made.

³In the beginning of the 1993 run, the steel overburden was still being laid. The rate of cosmic ray background fell a small but measureable amount during this process.

3.3 The active veto shield

LSND is surrounded except on the bottom by an active veto shield. (See figure 3.2.) This is a large tank of mineral oil with high light output scintillator “observed” by 292 5” PMTs. The barrel and one end of this anti-counter are in one piece, while the “upstream” wall, i.e.: closest to the beam production point, is a detachable part. (This was designed to allow disassembly of the anti-counter for service and possible reuse. The tanks were actually built for a previous experiment.[15]) Along the joint between the two pieces, and along the sides of the detector bottom, there are sheets of solid scintillator with a pair of PMTs for each which are used as “crack counters” to add extra information for the veto system. In much of what follows, the large shield and the crack counters will be referred to together as the “veto system”, and with very few exceptions the details of the separate treatment of the two components will be suppressed.

The veto system serves three purposes: First, cosmic ray events detected entering through the veto shield are ve-

toed. (I.e.: not recorded as primary events. They may still enter the data stream in recorded histories of later events.) Under certain conditions, subsequent events are also vetoed. (— Again, in the sense of not being accepted as primaries; they do not necessarily carry the veto flag.) Finally, the hit tube information from the veto shield is used in the reconstruction of vetoed events that are recorded in the data.

The detector has been run with various software veto conditions. The version used in the taking of the data used here is described in section 3.5. The inefficiency of the veto can be measured by counting the number of very high energy events in the detector, almost all of which are presumably cosmic rays. Using the raw veto rate as an upper bound on the number of cosmic ray muons entering the detector, the veto inefficiency is (roughly stable, and) $\mathcal{O}(10^{-4})$. Many events in the veto shield are presumably not related to muons entering the detector at all. Low level radioactivity in the veto system itself and cosmic rays which cross part of the veto but not the detector account

for a large number of events. Assuming the prediction for the rate at which muons enter the detector is correct, the inefficiency is at most $\mathcal{O}(\text{few} \cdot 10^{-5})$.

3.4 Front end electronics

The information needed from the PMTs for the reconstruction of an event is the charge deposited in the photocathode, and the time it was deposited for each PMT in which there was a signal. The charge is measured by depositing it on a capacitor, the voltage of which is read out at regular intervals. (The information from the veto system is processed the same way.) The time is calculated by extrapolating the voltage readings (read at the same regular intervals) on another capacitor, the constant charging of which is initiated by the passing of a discriminator level by the PMT backplane signal. An example of the signals which are used in this scheme are sketched in figure 3.3. The “hold-off discriminator” signal is a feedback to the backplane to prevent the pile-up of timing ramp starts. The time interval between readouts is regulated by a glob-

ally synchronized clock at 100ns intervals.

A schematic of the front end electronics for the reading of data from tubes to be processed by the trigger is shown in figure 3.4. The “flash analog–digital converter” (FADC) component is shown in figure 3.5. This can convert the analog PMT output (for charge or time information) to a digital signal useful for the trigger software in a few nanoseconds with a reasonable dynamic range since it uses 8 bits of information. The resistances used were chosen so that 8 ADC counts of charge in a PMT hit corresponds roughly to one photo-electron. This assures that the single p.e. peak can be distinguished (important for verifying detector performance), while giving (about) 32 p.e. dynamic range. The typical “occupancy” (*i.e.* : $\frac{\# \text{p.e.}}{\text{PMT hit}}$) is of order a few for most events of interest.⁴

The measurements done for the charge and time readings are all stored in dynamic dual-ported memories 2Kb deep. This memory is essentially a circular buffer, so af-

⁴In the 1993 configuration the charge and timing circuits were on hand wired boards. This was changed between the 1993 and 1994 runs, and the charge response of the boards was made more linear.

ter 2K clock ticks ($204.8\mu\text{s}$) the data is overwritten. The data addresses within this structure are the lowest order 11 bits of the global clock, and are thus referred to as “time stamp addresses” (TSA). When the global trigger decides that a given time is “interesting”, the TSA data is read from the dual ported buffers into first-in, first-out (FiFo) memory chips to be sent to the event builder and permanently recorded.

The same discriminator that initiates the timing voltage ramp also sends a signal to a card on which the total number of PMT signals in a given clock tick delimited interval is calculated, and sent to the trigger. (Actually, there are local sum cards for individual electronic crates, which in turn send output to global sum cards in the trigger crate.) The total number of PMT signals in some time interval can be interpreted as a (coarse, and non-linear) measure of event energy. It is on the basis of these global sums that the trigger decisions about whether to read out an event are made.

3.5 The event trigger subsystem

The logic for the trigger software is shown in the flow chart in figure 3.6.⁵ The hardware collects data continuously (see section 3.4) sending events with associated histories when the software trigger calls for them. Events are classified as “primaries”, “previous activities of primaries” (hereafter called activities), and “gamma primaries” (which are recorded with no activities of their own).

Though data is read on the channels every 100ns, the sum cards, and all triggering decisions based on them look at overlapping 200ns intervals. This makes the acceptance for events near any PMT multiplicity threshold essentially unity. (This makes the reasonable assumption that the light all arrives to the PMTs in a time small compared to 200ns.) If the decisions were made based on sums done at every cycle, there would not be full acceptance for events near threshold that were spread across two windows.

Events with 18 PMT signals in the tank or 4 in the veto

⁵The trigger logic for the 1993 configuration of the software is explained in reference [8], with a similar flow chart shown on page 28 of that reference.

within some 200ns period are classified as trigger activities and may be written into the data stream. If the 4 veto tube threshold is passed, this event is vetoed. If a further threshold of 6 veto tubes is passed, then this event *and* any event occurring in the next $15.2\mu\text{s}$ is also vetoed (but may still be in the data as an activity)⁶. The point of vetoing future events is to remove from the data stream decay electrons from cosmic muons that stop in the tank. $15.2\mu\text{s}$ is (about) 7 muon lifetimes, so this lowers the rate of such events by a factor of about 1000. (Decay electrons from stopped cosmic muons account for a large number of events in the data stream and constitute an important background to the $\bar{\nu}_\mu \rightarrow \bar{\nu}_e$ oscillation search.) Those muons that outlive the $15.2\mu\text{s}$ veto time provide a large sample of electrons in the energy range of decay at rest signal events. Since the vetoed events preceding these are written into the data stream, they are not a serious background to the search, and in fact serve to provide en-

⁶The four veto tube threshold was not in place in the 1993 run. None of the analyses done on that data considered events with 4 veto PMT hits useful as primary candidates, and the elimination of events with 4 or more veto hits from the sample of primaries allowed us to lower the (later explained) threshold for opening a gamma window.

ergy calibration (see section 4.1.2) and a study sample for particle identification (see section 4.3).

If an event is not vetoed and has more than 100 detector PMT signals in the 200ns window, it is a primary. It is recorded along with up to 4 activities occurring in the past $51.2\mu\text{s}$. (If there are more, the most recent four are kept.) In addition, it “opens a gamma window” for the following millisecond, in which any event with 21 to 100 tank PMT signals and less than 6 veto system signals is recorded as a special primary which is written without the previous history buffer. (If another primary with 100 hits enters the data stream in this window, the gamma window remains open until 1ms after that.)⁷

Every 200,000th vetoed event is written to the data stream as a special primary (with a complete history). The next vetoed event is also taken as data, along with its history buffer. These “veto prescale events” are used as

⁷This configuration is different from the operation in 1993, when only primaries with at least 300 PMT hits initiated a gamma window. During the 1994 run, the logic of the trigger with respect to the gamma window was changed back to the 1993 version, but the “gamma window threshold” was at only 125 PMT hits. The effective difference between this and the logic shown in figure 3.6 is irrelevant for this analysis since all primaries of interest will pass the 125 hit PMT threshold.

diagnostic tools to measure detector performance. (*E.g.*: deadtime due to the $15\mu\text{s}$ veto condition; the free rate of veto events is counted in integer multiples of 200,000.) There is also one other class of special event which is a primary generated to appear in the data stream at some pre-defined time after the leading edge of the beam macro-pulse. This is used to determine the time of an event within the pulse structure, and as a diagnostic to verify the validity of the beam gate flag. Another special condition which forces triggering is the generation of a laser pulse used for calibration. The nature of this pulse and its use are discussed later in section 4.1.1.

Figure 3.1: Cross sections of the main detector. There are 1220 8" PMTs lining the walls of the almost cylindrical tank shown. It is full of mineral oil with a very small concentration of Butyl-PBD.

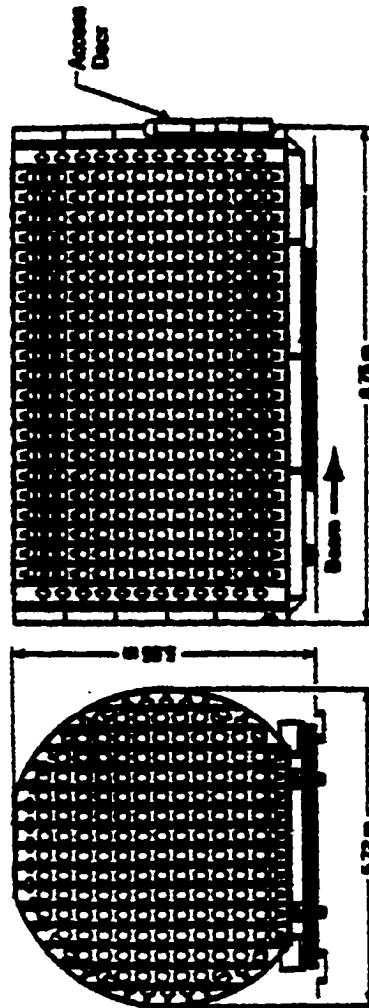


Figure 3.2: Cross section of the active veto shield. There are 292 5" PMTs viewing a thin layer of high light output liquid scintillator. Sheets of plastic scintillator line the sides of the bottom along the train rails.

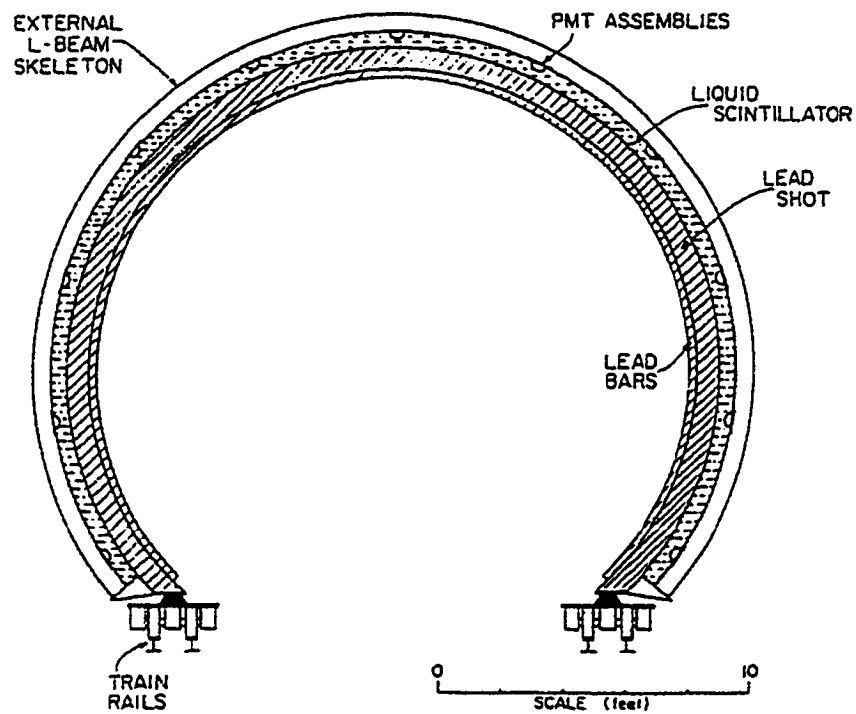


Figure 3.3: Signals in the front end electronics. The fine timing for PMT hits is derived from the voltages read at 100ns intervals.

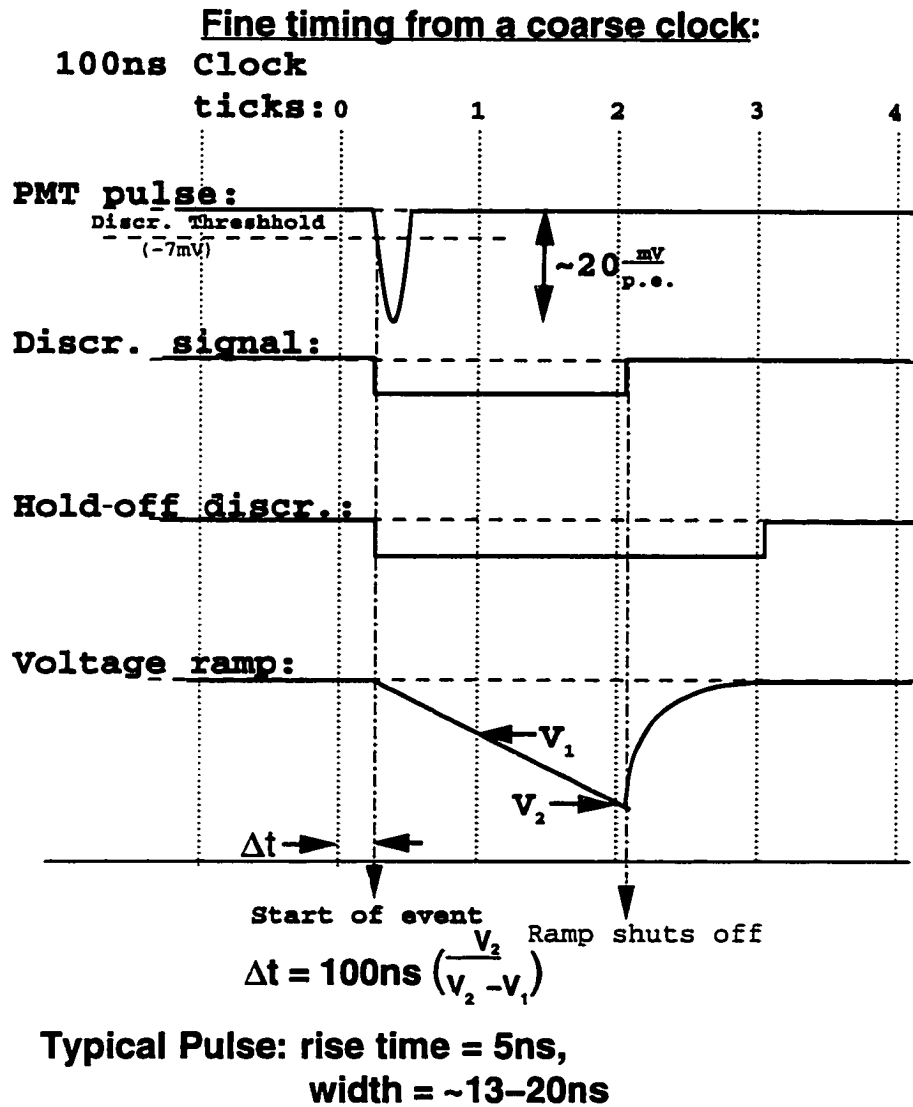


Figure 3.4: The detector front end electronics. "Discr" is the discriminator mentioned in figure 3.3. "FADC" is the analog-to-digital converter chip shown in detail in figure 3.5 (and the "8" near it is electronics jargon to denote that it passes 8 bits of information.) The globally synchronized clock and " Σ PMT" circuits are further explained in the text.

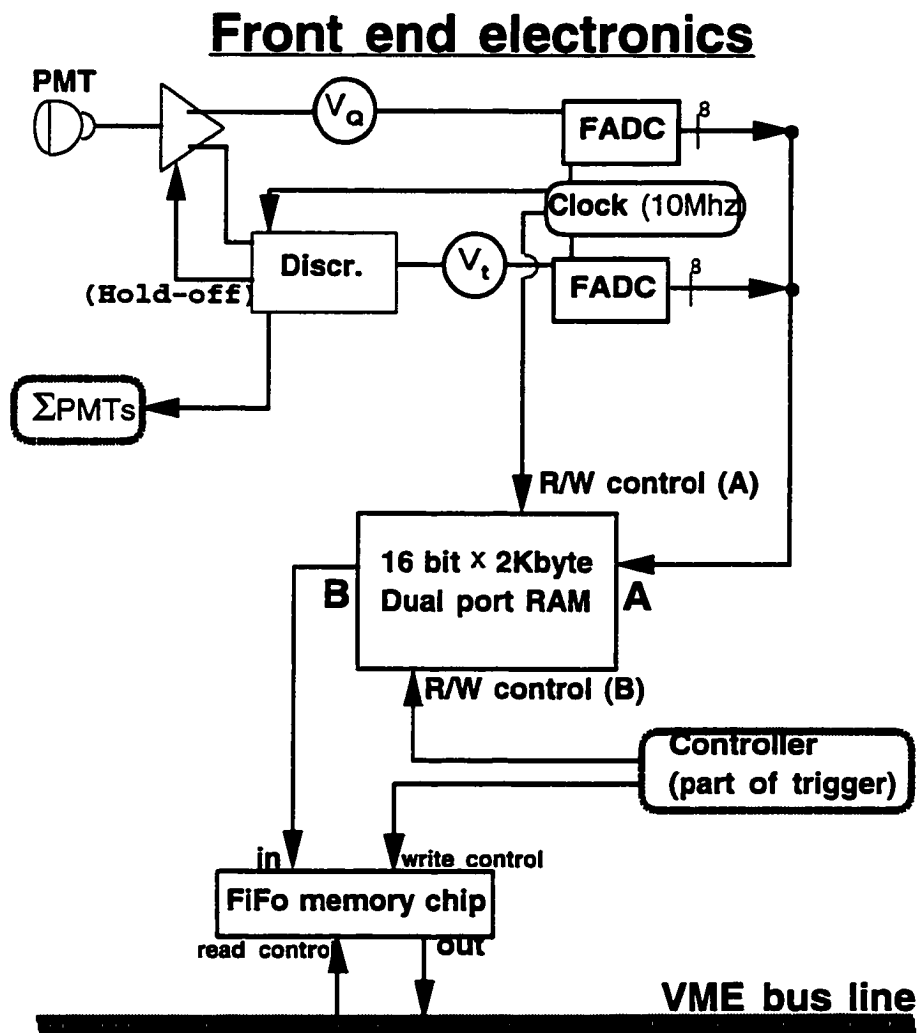


Figure 3.5: The "Flash" ADC chip.

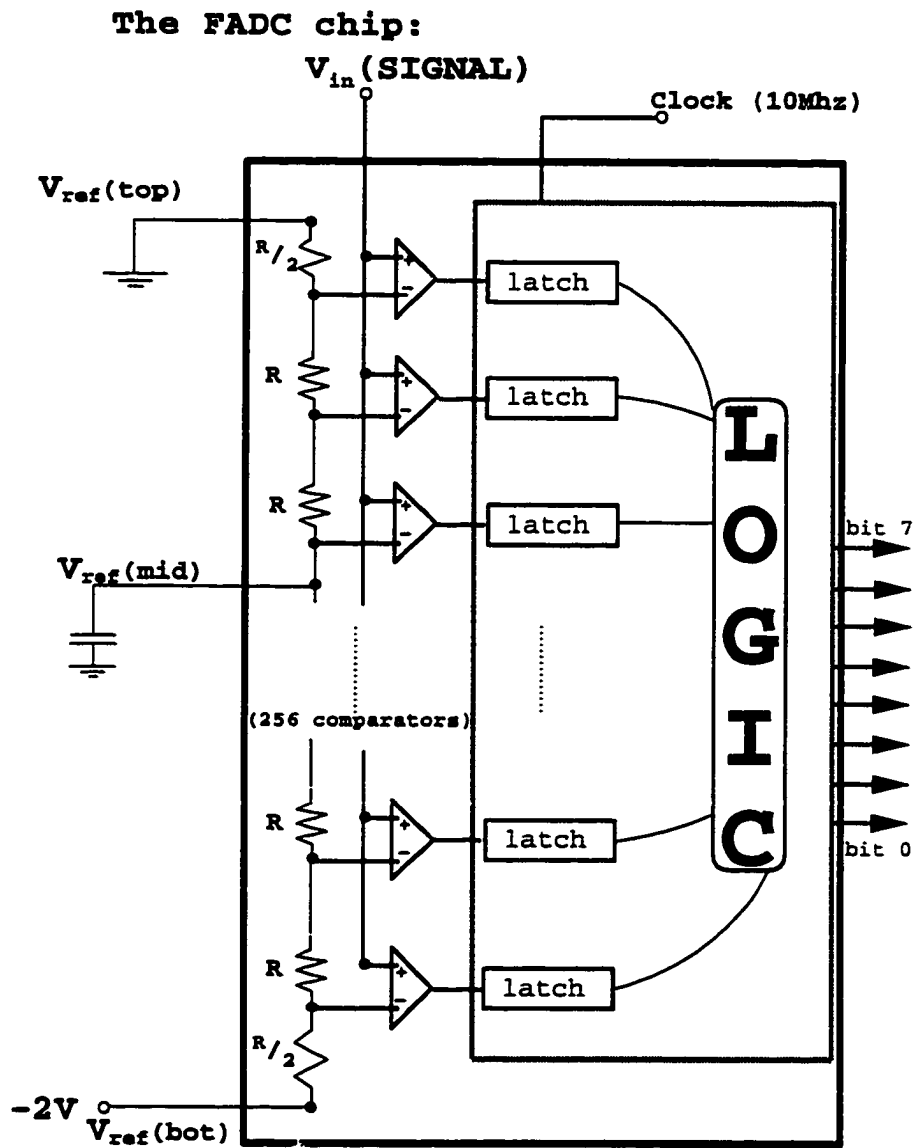
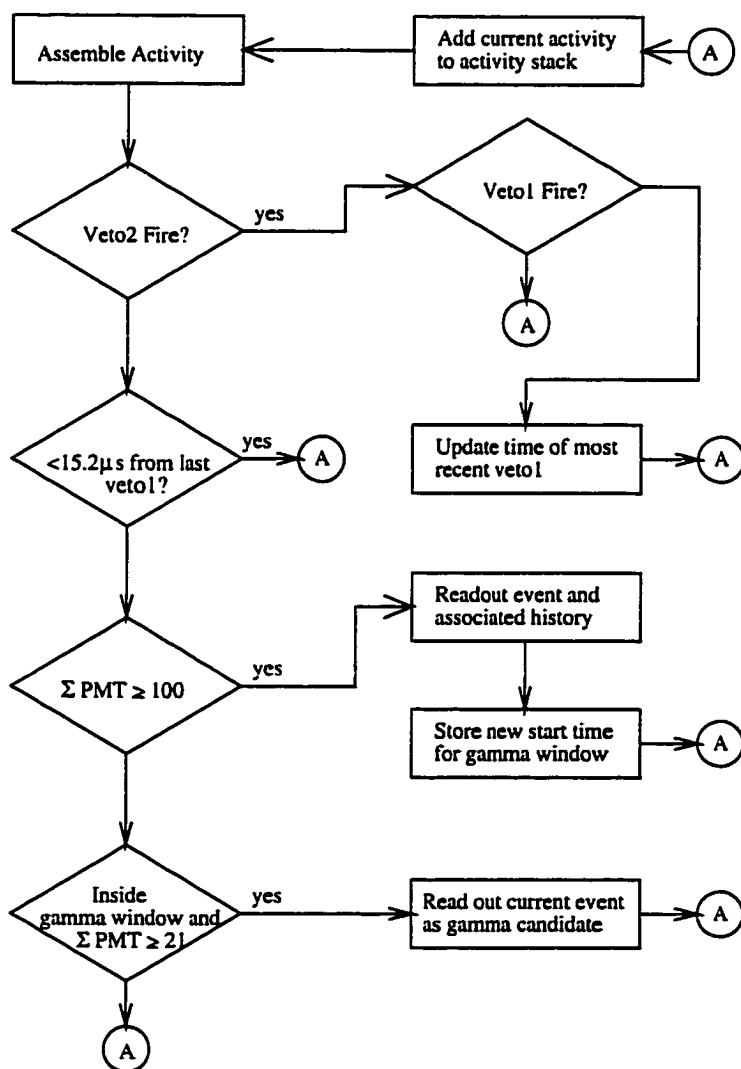


Figure 3.6: Flow Chart for the basic trigger logic. The special cases for veto prescale and beam timing events have been suppressed for the sake of clarity, as have distinctions about the separate veto subsystems. The circle labelled "A" is the "acquire state" in which the trigger waits for one of the detector or veto global sum logical bits to be asserted. The box marked "Assemble Activity" is described in detail in figure II-8 of [8]. Certain changes in the logic between 1993 and 1994 running conditions can be noted by comparing this to figure II-9 in [8].



Chapter 4

Events in LSND

This chapter addresses the general topic of how events occurring in the detector are characterized. First, the issue of calibration is discussed, both in the context of general calibration of the electronics, and in the specific context of the conversion of PMT signals to energies for electrons and for gammas. Then, the reconstruction algorithms and their performance for these two types of events are briefly described. After that, the particle identification parameter used for electrons is described and discussed. Finally, a short “tour through the data” is given, describing how the initially huge data set is pared down to a manageable size.

4.1 Calibration

The general designation “calibration” refers to two separate topics: calibrating the instrument (and its components) so that the signals from the PMTs are uniformly interpreted; and mapping the measured sets of PMT signals to energy for specific particles. These topics are now addressed in that order. Since there is a two-fold signature for the $\bar{\nu}_\mu \rightarrow \bar{\nu}_e$ oscillation search, there are separate subsections on energy calibration for electrons and low energy gamma rays.

4.1.1 Laser calibration

The LSND detector has a built-in hardware calibration mechanism in the form of three laser fired flasks hung in the body of the detector.¹ When the laser is fired, a bit is set in the trigger header for the event to denote this. The laser was run continuously through the accelerator run period, and the data from laser events extracted and analyzed

¹The one laser resides in a secondary electronics hut near the detector. Light from it is routed through either of three fiber optic cables into the detector and down to the flask, which is filled with a suspension of microscopic teflon balls to diffuse the light.

periodically to update calibration parameters. Runs were done with the laser intensity at various levels to get different information. Low intensity laser flashes identify the single photo-electron peak in the PMTs. Reconstruction is performed on the laser events to set time offsets for the electronics channels, as well as time slewing corrections.² This is iterated until the reconstruction of these events does not improve, where improvement is defined by a decrease in the variance of the offsets for all tubes. The position reconstruction error for a large set of laser events is plotted in figure 4.1. These events were chosen to have about the same amount of light (measured by the PMTs) as electrons in the 35 to 65 MeV range. Unlike electrons, the laser flashes emit light nearly isotropically, and are always well within the tank volume. Still, this gives a general idea of the quality of the vertex reconstruction.

²Time slewing is the effect that pulses of the same shape but different amplitude will take different times to drive a discriminator above threshold.

4.1.2 Electron energy calibration from muon decay

The large background of cosmic ray muons that come into the tank provide a good sample of easily tagged decay electrons. By looking for events with a broadcast history event that was vetoed, such a sample can be gathered in an almost³ unbiased way. To be more sure that the tagged pair is correlated, the sample chosen for this work have exactly one broadcast history event.⁴ The only other requirements are a fiducial cut (50cm from the surface defined by the phototube faces – an explanation for this choice will be given later in section 4.2.1.), a tighter in-time veto requirement than the hardware requires, and a (very loose) selection on the number of tank PMTs with signals. The very high rate of β activity in the tank would create a background of accidental coincidences (just because of the high statistics of that phenomenon). The sample thus gathered has about half a million events, the decay time distribution of which is shown in figure 4.2. The fitted

³The region near the bottom of the detector, where the veto is weaker, might be under-represented, but nearly all cosmic rays come from above, so this is a high order effect.

⁴Relaxing this would not dirty the sample too much, but the gain in counts would only be 15% or so.

function displayed in the plot is exponential + constant. This shows under 2% background using the full sample. For studies requiring a purer sample, this background can be reduced by cutting the correlation time requirement, or statistically compensated by looking at the longer time events separately.

The spectrum in photo-electrons for these events is fit to a theoretical Michel spectrum with Gaussian smearing to find the charge/MeV calibration and uncertainty. The fractional uncertainty is assumed to fall as $\frac{1}{\sqrt{E}}$ (since this is essentially a counting problem for the photoelectrons⁵). This prescription gives about 8% resolution at the Michel endpoint (52.8MeV). Since there was a change of the (more basic) electronic calibration in the middle of the 1994 run, this sample is split in two and analyzed separately. The energies referred to later all account for this discrete change in calibration. The data spectrum and fitted function for

⁵Recent work by collaborators in Santa Barbara suggests that the running of the energy uncertainty as a function of energy may be somewhat slower, $\propto E^{0.2-0.3}$. Comparing the fit here to the fit for the ^{12}B β decay endpoint agrees with the hypothesis of the uncertainty running as $E_e^{1/3}$. This is not too important for any of the work here, since the energy range in the decay at rest search is small, and the calibration is only useful in its gross properties for the decay-in-flight candidates.

the latter part of the run are shown in figure 4.3.

Electronic non-linearities are not important in this energy domain because the average “occupancy” (i.e.: p.e. per hit tube) is always well above one, but far below saturation. There is some dependence on position and direction of the event, but this is small and figures into the uncertainty. To attempt to correct for this would introduce the error of the reconstruction of those quantities into the energy calibration. Also, if correlation with reconstructed properties of the event are considered in energy calibration, then the converse correlations should also be taken into account so that there is not any enhancement of geometrical biases.

We also check energy calibration in a much lower energy range by similarly fitting the ^{12}B β spectrum endpoint. (^{12}B is produced by the capture of cosmic μ^- in ^{12}C nuclei.) A sample of these decays is chosen by a strong fiducial requirement (80cm from the PMT faces) and a requirement of no broadcast previous activities. Since the lifetime of Boron-12 is 16ms, the loss by this cut is negli-

gible. Figure 4.4 shows the fitted spectrum for the same part of the run as the muon decay electrons in figure 4.3. The crucial feature is that the overall calibration of photoelectrons to MeV is (within the large error of this fit to a beta spectrum) the same.

4.1.3 Low energy gamma calibration

Since 2.2MeV gamma rays are part of the signature for $\bar{\nu}_\mu \rightarrow \bar{\nu}_e$ oscillation event candidates, a verification of the Monte Carlo prediction for the energy calibration and uncertainty for low energy gammas is also needed. Since the LSND veto shield is not very massive, its efficiency for rejecting cosmic neutrons is not nearly so good as that for muons. This allows many high energy neutrons to enter the detector. These high energy neutrons will often interact strongly with a proton in the mineral oil before coming to rest, and thus lead to enough light to initiate a gamma window. This gives a sample of real neutron captures to study. Since the accidental rate is high, it becomes more convenient (and more accurate) to get a statistically ar-

rived at distribution rather than try to tag a pure sample. This is done by looking in the late part of the window to identify presumably random gammas, then subtracting the appropriate binned distribution from a corresponding "early window" distribution. The results of this are compared to a sample chosen by tight time and distance cuts for the sake of completeness.

Figure 4.5 shows the time distribution for a large sample of events with exactly one gamma candidate in their window taken throughout the run. The useful variable for energy measurement at such low energies is the number of PMT signals in the tank (rather than their accumulated strength). The peak of the spectrum for 2.2MeV capture gammas from cosmic neutrons is 33 hit tubes, and its width is about 7, in good agreement with the Monte Carlo. The same data shown in figure 4.5 is shown again later in figure 5.7 along with plots representing the relative distance between primary and gamma vertices. That figure has marks to show the selection criteria actually used for (discussed in section 5.7) for neutron capture gamma

rays in $\bar{\nu}_\mu \rightarrow \bar{\nu}_e$ candidate events.

4.2 Event reconstruction

The on-line analysis uses different reconstruction algorithms for three identifiably different types of processes that occur in the detector. Cosmic muons, identified by the firing of the veto shield in coincidence with the tank, are reconstructed assuming they pass through the tank. Gamma rays from radioactivity or neutron capture on hydrogen, identified by the multiplicity of PMT signals, are reconstructed by a faster algorithm than is used for electron candidates, and an angle fit is not attempted. Other events are reconstructed on-line as electrons. Since no information from the cosmic muon fit is ever used in the analysis here, only the electron and gamma reconstructions are discussed.

A driving consideration in the choice of algorithms is the event rate. For the rates typical of the 1994 run, each algorithm has to be performed about 10 times each second to keep up with the data on-line. Since electron recon-

struction is most critical, some precision in the gamma reconstruction was sacrificed to speed up the whole process.

4.2.1 Electron reconstruction

Reconstruction of the position and time of an electron event is performed by minimizing the function:

$$\chi^2_{(\vec{x},t)} = \sum_{i \in \{\text{hit tubes}\}} Q_i \cdot \left((t_{rec} - t_i) - \frac{|\vec{x}_{rec} - \vec{x}_i|}{c/n_{oil}} \right)^2 \quad (4.1)$$

for only those tubes where $(t_{rec}^{(0)} - t_i^{(0)}) < 12ns$ from the initial pass described as follows: The initial time guess is the average of the times for the tube hits which are no more than 100ns after the mean time, minus a constant offset which was determined by optimizing performance on Monte Carlo events. Tubes with less than 4 photo-electrons deposited are then assigned the earliest time of any hit in their “nearest neighbor cluster” of hits for all subsequent steps. The first guess for position is the weighted average of the “corrected positions” of the hits. The weight assigned is the square of the charge deposited,

and the corrected position is the tube's position shifted along the line to the tank center by $\frac{c/n_{\text{oil}}}{\text{corr time}}$, where “corr time” is the time of a particular hit relative to the initial guess for time.

The angle fit for direction is done by minimizing the function:

$$\chi_{\text{angle}}^2(\hat{p}) = \sum_{i \in \{\text{prompt tubes}\}} \mathcal{W}(\theta_i) \hat{p} \cdot 0.5 \left(\frac{\theta_i - \theta_{\check{c}}}{\theta_{\text{rms}}} \right)^2 \quad (4.2)$$

where θ_i is the angle between the ray from vertex to the PMT (i) and the direction of the track. The weighting function \mathcal{W} is written out in reference [16]. It is an *ad hoc* discontinuous function which weights the datum more highly if it is near the Čerenkov angle. The object is to do this fit only if the Čerenkov cone is prominent, and try to use only Čerenkov light in the fit, so only hits with corrected times less than 4ns are used. The minimization for this function is started with a simple “grid search” over a pre-defined set of 26 directions from the fitted vertex.

Some idea of how good these reconstructions are can be gotten directly from the data by looking at the cosmic muon decay electron sample. Assuming that the muon

entry point is well known and that its path is linear and its energy loss constant, the stopping point (at which the decay occurs) is constrained. These are quite fair assumptions, but the constraint is not strong since it depends on knowing the muon energy accurately. Depending on the exact path on which it enters, the light detected may differ significantly. Apart from this, a scatter plot of the distance the muon travelled versus its energy should show events on a line with appropriate slope to represent its energy loss. The width of the distribution around this line comes from the uncertainty in the muon energy and the reconstruction uncertainty in the electron vertex and muon entry point. Reference [8] (page 34) used this argument to obtain upper bounds on both the electron vertex reconstruction, and the muon energy calibration uncertainty.

One expects that the reconstruction must degrade as events get very close to the PMTs. This degradation can be measured by looking at a cosmic muon decay sample. Figure 4.6 shows the reconstructed distance from the PMT faces for a set of muon decay electrons gathered from a few

weeks of data. The comparison to geometrical phase space shown in the figure indicates some reconstruction effect or loss of efficiency⁶ at distances less than $\frac{1}{2}$ meter from the PMT faces.

4.2.2 Gamma reconstruction

The gamma reconstruction algorithm is used on events with less than 100 tank PMT and less than 4 veto PMT signals. It is a simple “one pass” algorithm much like the first guess method for electrons; there is no minimization performed. Although the threshold for not using this fit is 100 PMTs, most events it is used on have only 21-30. The general idea is to take the average position of all PMTs with signals after correcting for a time of flight.

⁶Detailed monte carlo studies favor the hypothesis of systematic reconstruction error. Both effects are probably present. For the search for neutrino oscillations, the distinction is not so important; events too near the wall are suspect in origin or character, and should not be included.

4.3 Particle Identification

The primary task in both oscillation searches is to identify an electron in the detector. The essentially distinguishing feature of electrons is that they are highly relativistic at all energies of interest here, while, except at the highest energies relevant, muons are not.

The essential information for particle identification thus lies in the ratio of Čerenkov to scintillation light emitted by a particle. This can be measured by looking at the distribution of light in space and time. The angle fit converges well only for events with sufficient light in the Čerenkov cone, so the χ^2 for this fit is an appropriate variable to identify relativistic particles. A simple measure of the time distribution for light is the fraction of charge deposited in PMTs after some designated time. To make use of the information from both these data in a single parameter, the product of the direction fit χ^2 and a late charge fraction is taken. To remove ambiguous events in which all of the reconstructions are questionable, the χ^2 for the track position fit is also used as a factor in this overall particle

identification parameter. Monte carlo work done before data were taken in LSND suggested this combination as a variable which separated muons from electrons well. The definition of the parameter is:

$$\chi_{PID} \equiv \left(\frac{1}{30}\right) \cdot \chi_{direction}^2 \chi_{position}^2 \frac{\textit{charge after 30ns}}{\textit{total charge deposited}}$$

Figure 4.7 shows the distribution of this parameter for signal and background events in the Michel electron sample. The separation is made by taking events with $\Delta(t_e^\mu) < 30\mu s$ for signal, and those with $\Delta(t_e^\mu) > 35\mu s$ as background. This should give less than 1% background in the “signal” sample, and a few percent “signal” in the background sample. Figure 4.8 shows the “signal” data again in a scatter plot of χ_{PID} versus energy. (So the top plot in figure 4.7 is the y-axis projection of figure 4.8.) Since an energy dependence of the parameter is observed, a correction is made to compensate. Figure 4.9 shows the same data as figure 4.8, but with the energy correction applied to the particle identification parameter. To get the proper energy dependence, data from the electron sample was binned by energy, and the raw parameter histogrammed

for each energy band. The means and rms deviations of the different histograms were then plotted and fit to a reasonable parameterization⁷. The definition of this energy corrected parameter is (in terms of the raw parameter):

$$\chi_{\text{PID}}^{\text{cor.}} \equiv \frac{\chi_{\text{PID}} - (0.89/(1 + 0.014 * \text{energy}))}{(0.18/(1 + 0.013 * \text{energy}))}$$

Figure 4.10 is a reprise of figure 4.9 except that it uses the energy corrected version of the parameter. The behavior of this parameter is not quite gaussian, but clearly characterized for these signal-like events. The separation of the two peaks in the lower plot of figure 4.10 is somewhat better than in figure 4.7. Equally important, this parameter is presumably useful in the energy range of the decay in flight neutrino oscillation search.

⁷The parameterization chosen was $\frac{\text{Par}_1}{1 + \text{Par}_2 E}$. This behaves as one would expect the particle identification parameter might at low and high energies. One can either make an energy dependent cut on the raw parameter, or correct the parameter for each event and make a constant cut on the corrected variable. The two procedures are identical. Later, when showing invariance of the final result under changes in selection, it is most useful to think of the procedure as applying a constant cut to the corrected value of the variable. (If comparing this work to other analyses of this data, it is most convenient to think of the above procedure as using an energy dependent cut on the raw parameter.)

4.3.1 Monte Carlo predictions

Particle identification in general, and the specific parameter used here for that, rely heavily on knowing the details of the time distribution of light within an event. (This is true of the χ^2 parameters as well as the fraction of late light, since the fits done must use timing information for the individual PMT signals.) An attempt was made to measure the detailed timing characteristics of light from Butyl-PBD in a test beam experiment [17] done by the collaboration before the detector was operational. While this provided much valuable information, it turns out that the monte carlo results for values of particle identification parameters are not in agreement with the data, and seem too sensitive to changes in the detail time behavior of scintillator light. All results concerning electrons in this work, with the exception of claims of the accuracy of reconstruction, are based on studies of the decay electrons from cosmic muons.

It should be emphasized that while *a priori* calculations cannot properly predict the exact behavior of the par-

ticle identification parameter, its distribution for signal like events is well understood. Since, in the absence of robust simulation predictions, it is difficult to accurately characterize correlations between different particle identification parameters, this work relies on only this one parameter.⁸

⁸By using several correlated parameters, one forfeits the ability to study *systematically* the effect of variation of selection of events.

4.4 A tour through the data

Figure 4.11 shows the detector PMT signal multiplicity for all events entering the data stream in a file covering about 80 minutes (real time) in November. The large peak near 0 is mainly from events that are written because the veto shield initiated an activity which was recorded because of a later detector event. (See section 3.5 for a review of the trigger operation.) The peak above 20 PMT signals (the threshold during the 1ms gamma window) is due to both low energy gammas in the tank, and cosmic events. The vast majority of events with more than 100 tank PMT signals are from beta decay electrons from ^{12}B produced by muon capture on carbon nuclei. At the high end of the spectrum, there are cosmic events, some of which are vetoed, and enter the data stream either because the muon outlives the $15\mu\text{s}$ veto condition, or because an accidental follower occurs 15 to $52\mu\text{s}$ later. Others in this peak are cosmic events which evaded the veto. (In section 3.3, it was mentioned how such events are used to measure the veto inefficiency.) Finally, above the tail of the β spectrum, one

can see the shape of the spectrum of decay electrons from cosmic muons.

$3 \cdot 10^8$ events analyzed in 1994 run

$\sim \frac{1}{3}$ of them as histories and $\sim \frac{1}{3}$ as gamma candidates

Applying lower bound on energy (above β spectra): $\sim 1.5 \cdot 10^7$

An upper bound to reject cosmics gives another factor of 2 suppression

Requiring that the reconstructed track is within the tank reduces this by another factor of 2 – 3, and a (mild) further past activity cut gives a factor of 4.

Note that no particle ID has been used (except that convergence for vertex reconstruction is implied).

Also, the beam status tag has not been inspected.

This leaves $\mathcal{O}(\text{few} \cdot 10^5)$ events, including any oscillation candidates. Now, it is time to start looking at the selection criteria in more detail. The next two chapters will explain the selection of signal event candidates for each of the two oscillation searches.

Figure 4.1: Reconstructed position error for a large set of laser events. The abscissa is taken as $(\Delta r)^2$ to factor out phase space. These events span the full time of the 1994 run, and are chosen only by the laser tag and their having deposited as many photo-electrons as a decay at rest signal event (7 events are overflows, past $(\Delta r)^2 = 1000\text{cm}^2$). The RMS reconstruction error is only about 13cm.

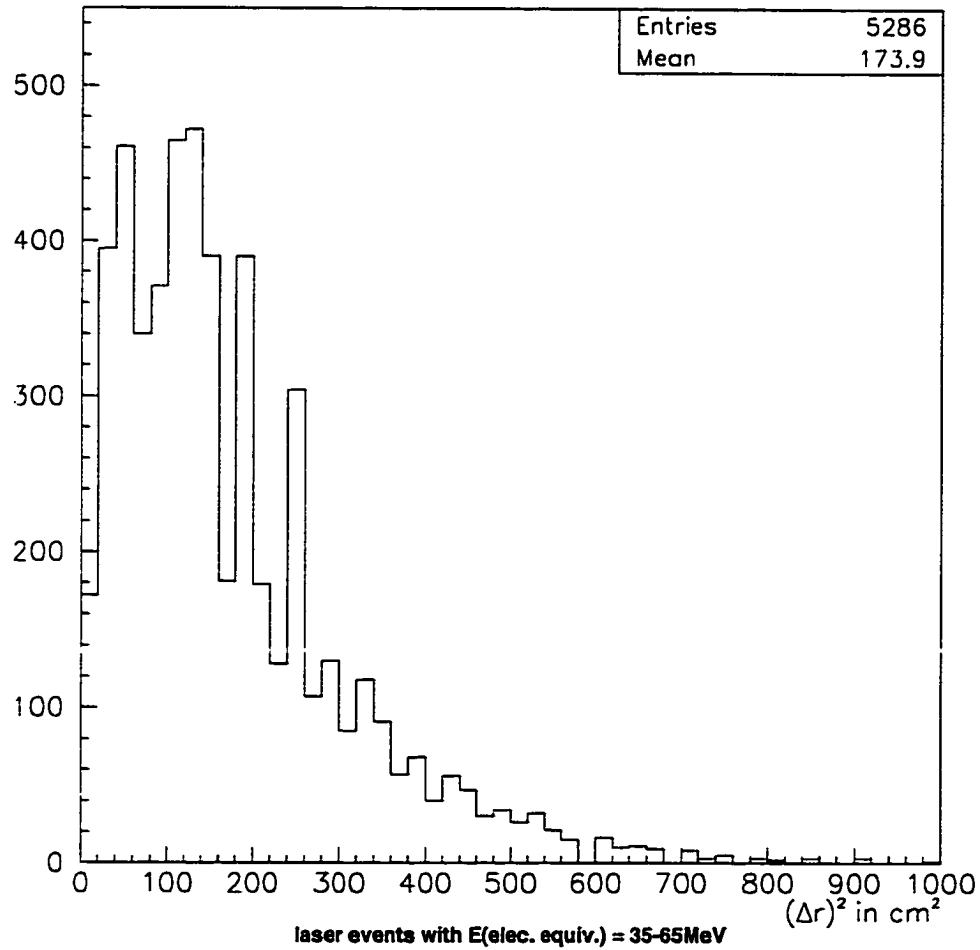


Figure 4.2: Decay time for a sample of vetoed cosmic ray muons. The fitted decay time (shown as parameter 2) is $2.147 \pm .007 \mu\text{s}$. This sample represents the full 1994 run. The level of background from the fit is about 1.8%. Note that this is *before* applying the PID cuts. By fitting instead to the sum of two exponentials with known lifetimes, one finds the cosmic ray muon “charge ratio” to be 1.3 ± 0.1 . The normalization of either fit shows that approximately $7 \cdot 10^8$ muons decayed in the volume used here.

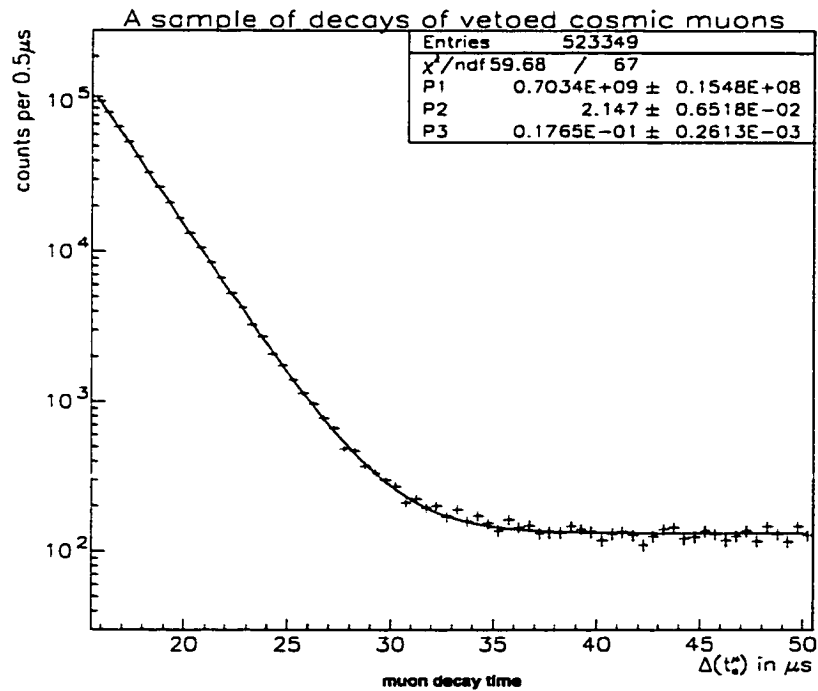


Figure 4.3: Spectrum of electrons from stopped muon decay. This covers the second calibration period of the 1994 run, and only candidates with decay time $< 30\mu\text{s}$ are taken, giving under 1% background. The fit parameters are: P1 = calibration in $\frac{\text{p.e.}}{\text{MeV}}$, P2 = endpoint uncertainty as a fraction of energy, and P3 = an overall normalization.

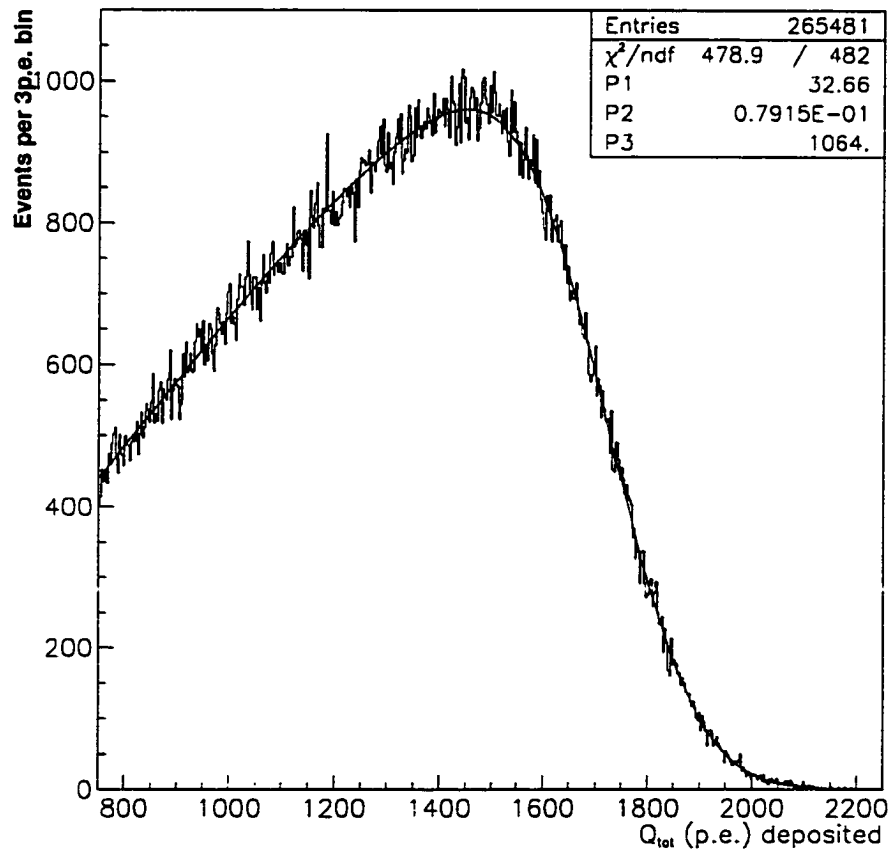


Figure 4.4: β spectrum tail with calibration fit. The run period covered the same as that for the muon decay spectrum shown in figure 4.3. The calibration (parameter 1 of the fit) agrees to 2% with the calibration at the muon decay endpoint. The endpoint uncertainty ($P1 \cdot P2$) scales as $(E_e)^{1/3}$ from the muon decay endpoint.

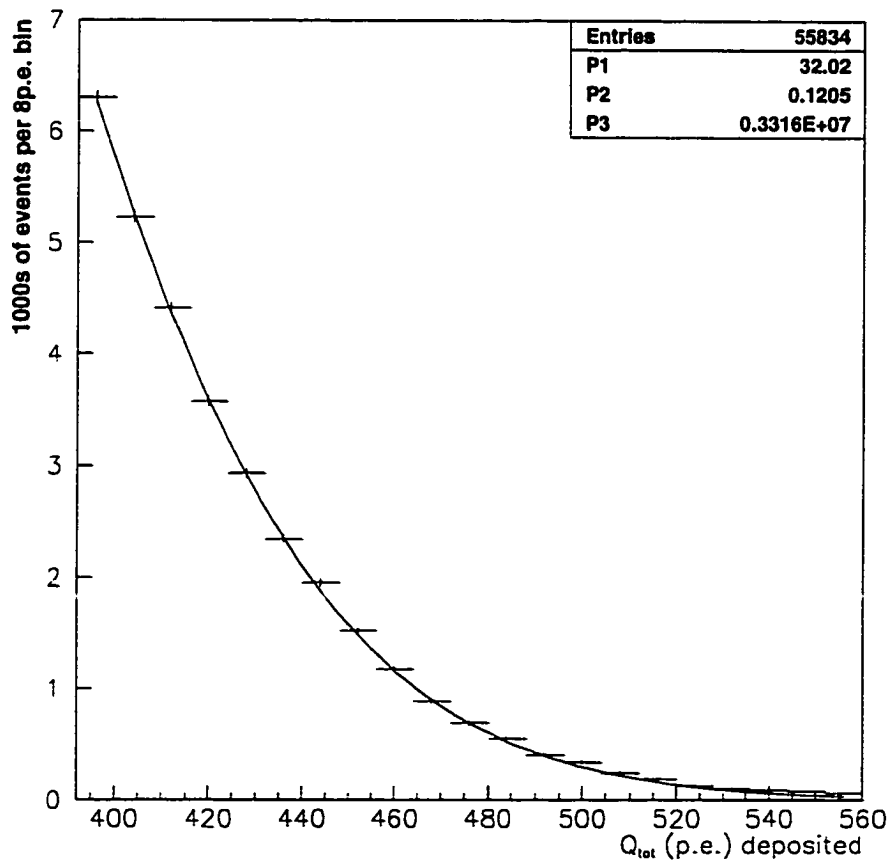


Figure 4.5: Gamma properties for a sample from the full run. The top histogram is the time from primary to gamma. The fit to exponential + constant shows the predicted capture time of $186\mu\text{s}$ (shown as "P2"). The gammas in the last quarter of their window are taken as characterizing accidental coincidences. The spectrum in PMT multiplicity for neutron capture gammas is gotten by subtracting the distribution for the accidental gammas from the corresponding distribution for the first quarter of the window.

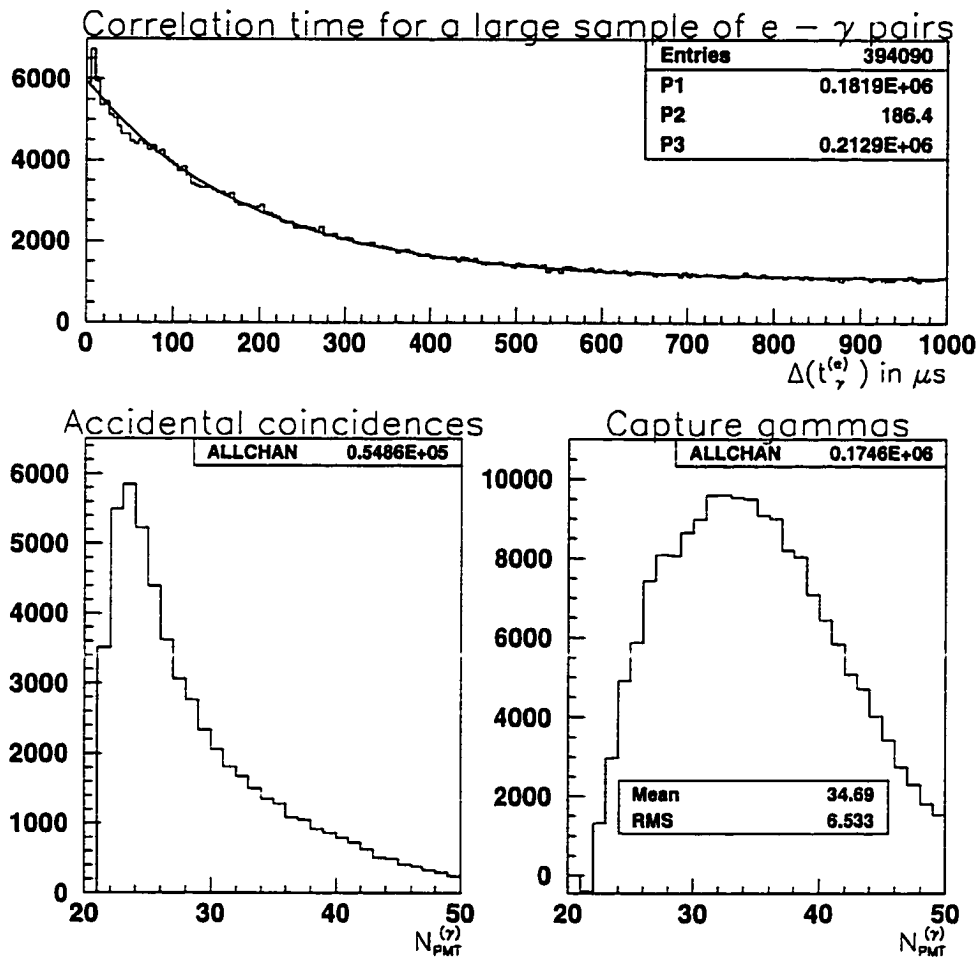


Figure 4.6: Fiducial distance (d_e^{PMT} in cm) for a sample of electrons from muon decay. The entries are chosen by time after a vetoed activity event (with a fiducial cut at $d=0$ for the electron) and a lower bound on energy. The phase space histogram is normalized to match the data at 50cm.

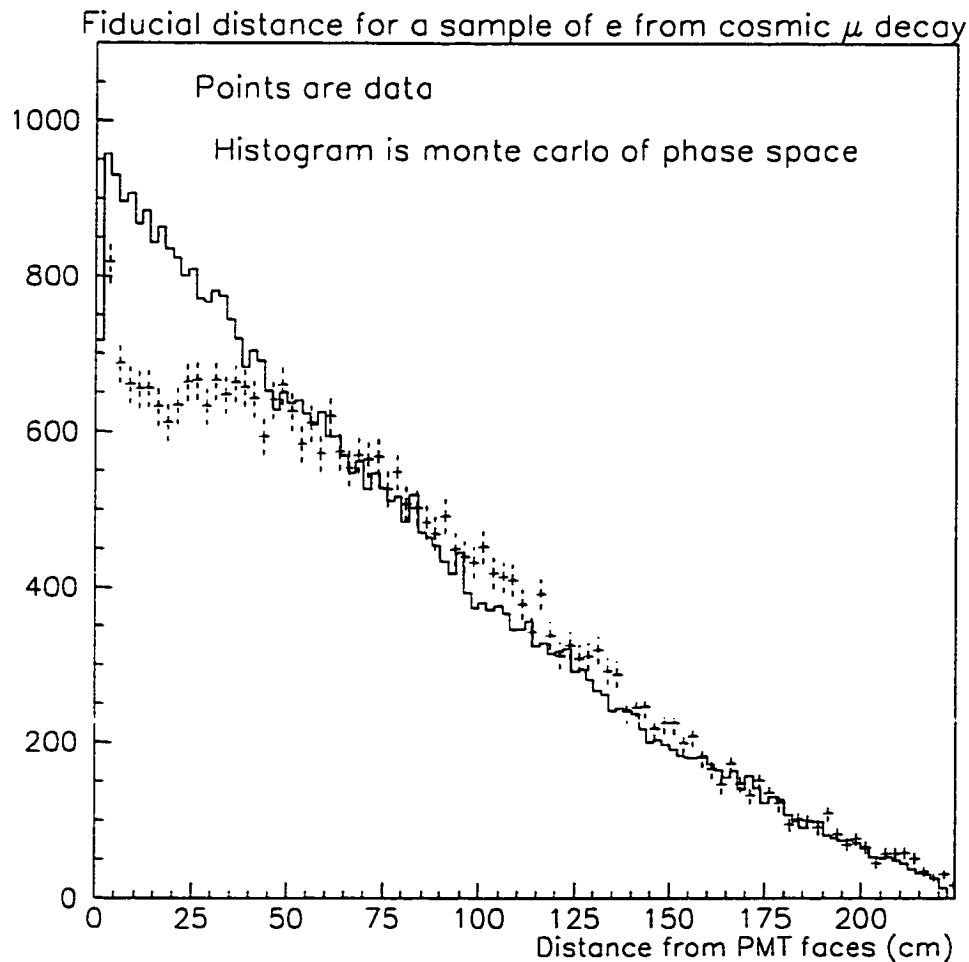


Figure 4.7: Raw particle id. parameter for events in the 25 to 65MeV range from the muon decay sample. The top plot uses only events with $\Delta(t_e^\mu) < 30\mu s$; the bottom uses only those with $\Delta(t_e^\mu) > 35\mu s$.

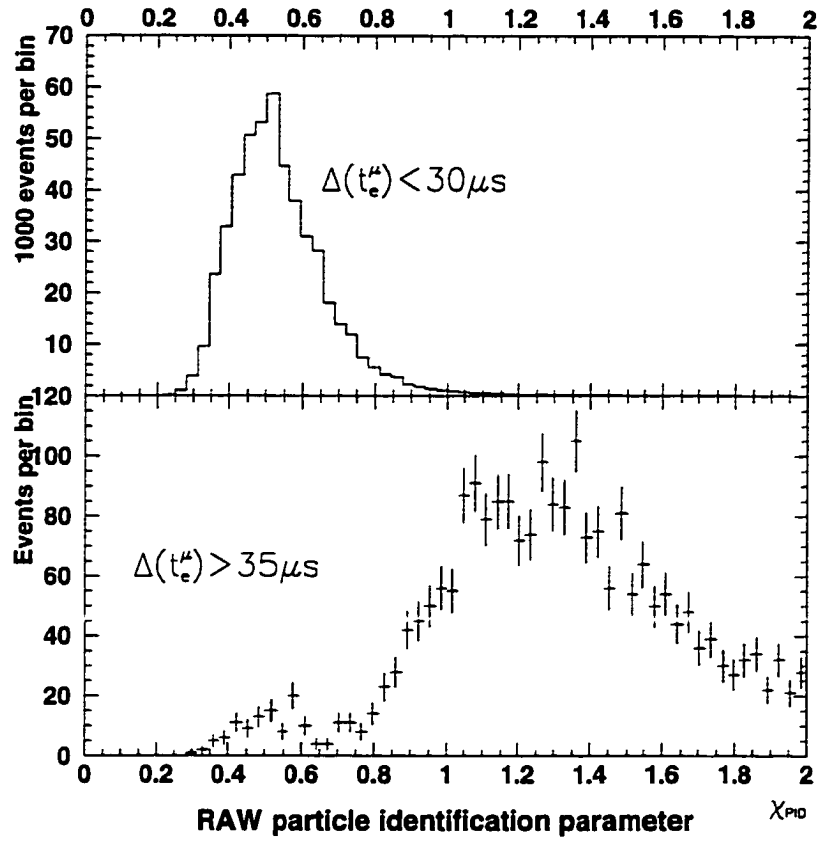


Figure 4.8: Raw particle identification parameter as a function of energy for electrons. The sample covers the whole run. The energy range below 35MeV is only relevant for background studies, and for extra data on the energy dependence of the particle identification parameter.

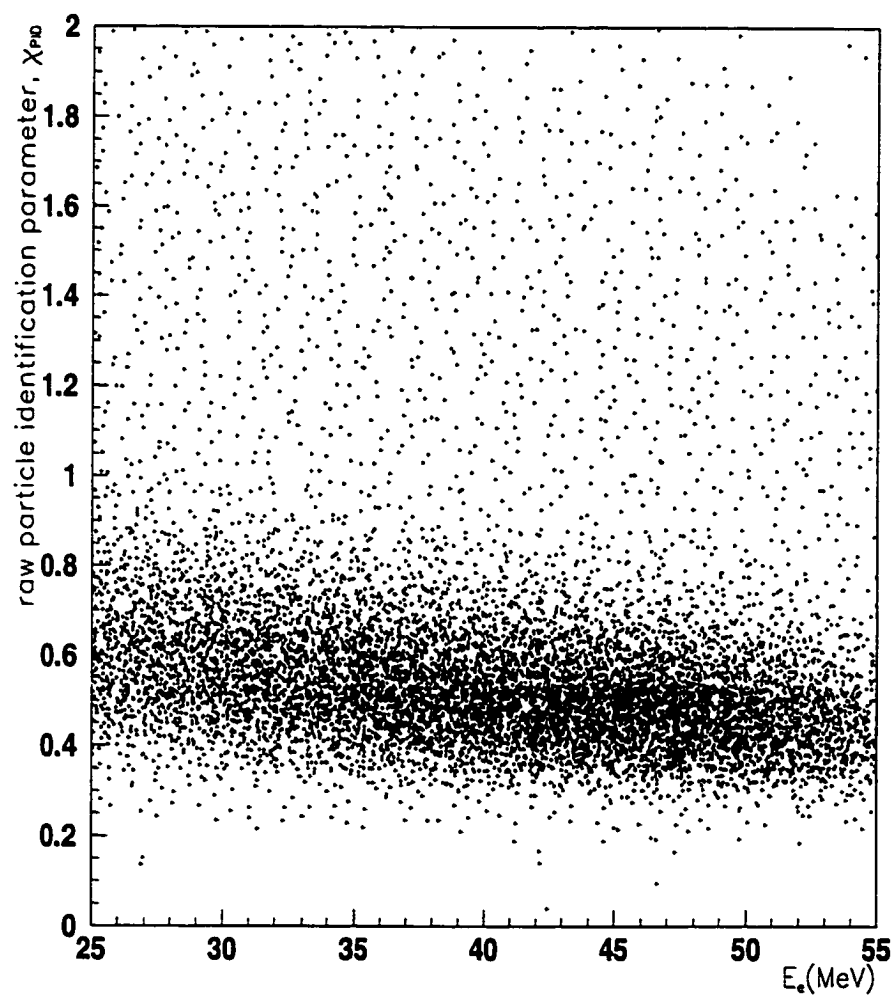


Figure 4.9: Energy corrected particle id. parameter versus energy for electrons from cosmic ray muon decay. These are the same data as figure 4.8, but here the energy correction is applied. The upper bound for event selection is a constant in this representation.

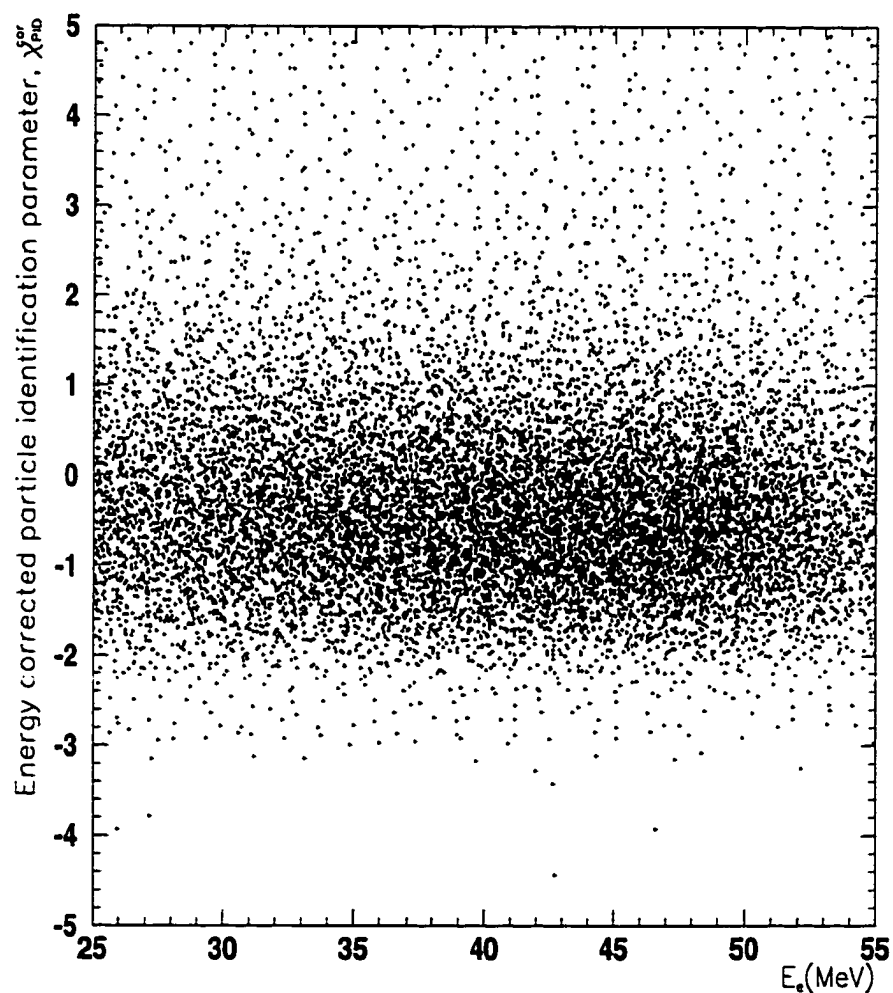


Figure 4.10: Energy corrected particle id. parameter for events in the 25 to 65MeV range from the muon decay sample. The top plot uses only events with $\Delta(t_e^\mu) < 30\mu s$; the bottom uses only those with $\Delta(t_e^\mu) > 35\mu s$.

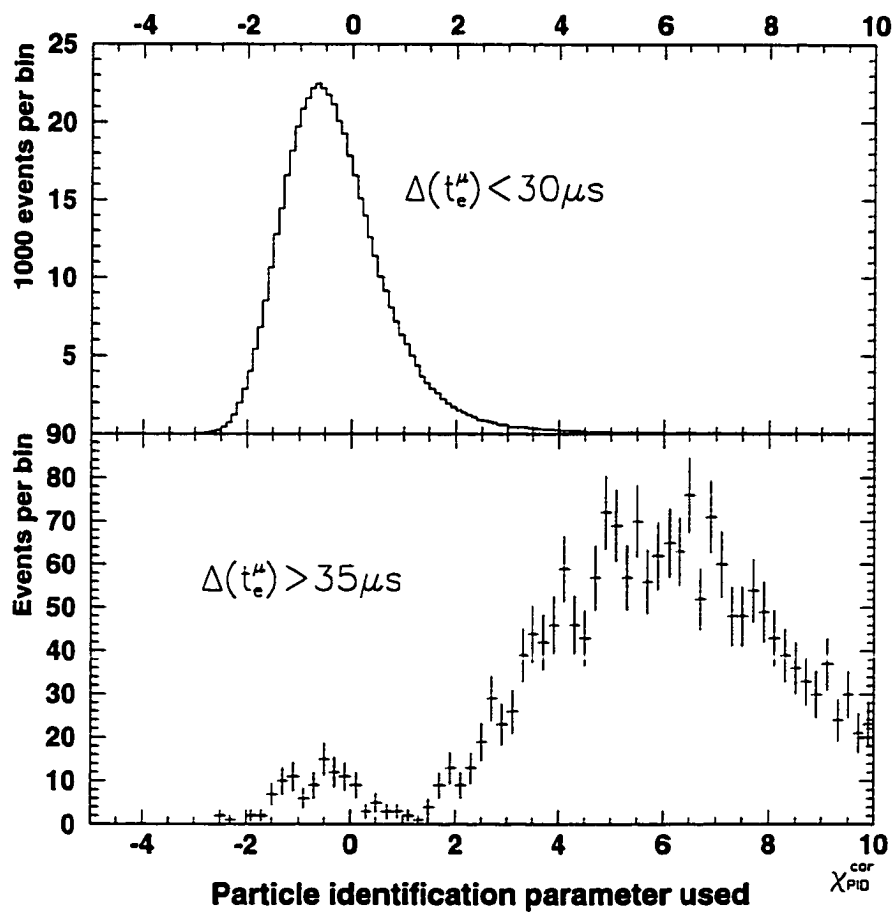
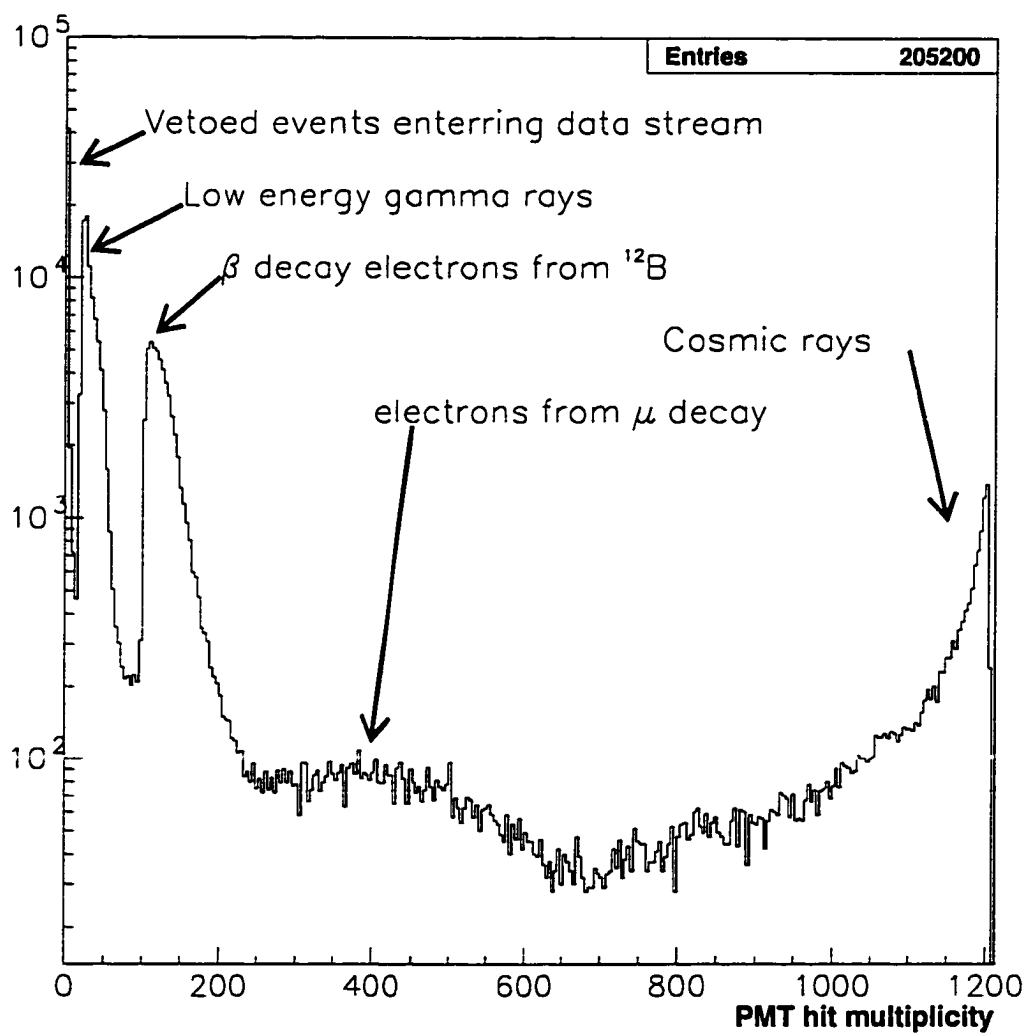


Figure 4.11: Detector PMT multiplicity for all events in some 80 minute period in November. Notes on the figure point out some important features. (There are 1220 PMTs in the detector, but 15 electronics channels were not functional at the time this file was written.)



Chapter 5

Selection of $\bar{\nu}_\mu \rightarrow \bar{\nu}_e$ event candidates

In this chapter, the final event selection for $\bar{\nu}_\mu \rightarrow \bar{\nu}_e$ event candidates is explained. First, the signature of signal events are explained. Then, the various criteria for selection of signal candidates and their efficiencies are presented. After that, signal event rates and some background calculations are presented, and the effect of the various selection criteria on them are discussed. The basic form of the selection criteria are presented in tabular form in table 5.2. Variations on these final selection criteria are explored in the last section, with emphasis on the stability of the results against changes, and tabulated in tables 5.4 and 5.5.

5.1 Signal event signature

The specific reaction observed for the detection of $\bar{\nu}_e$ from oscillations of $\bar{\nu}_\mu$ is the production of a positron from a free proton. Thus, the primary signature for these events in LSND is the detection of an isolated electron type event. The positron will have energy close to that of the incident neutrino¹. The remaining neutron will soon capture on another hydrogen atom, (The capture time is $186\mu\text{s}$; see section 4.1.3 and figure 4.5.) emitting a 2.2MeV gamma ray (the binding energy of deuterium), thus giving a delayed time coincidence.

5.2 The fiducial region chosen

Reconstruction effects discussed previously in section 4.2.1 limit the useful volume to a region at least a half meter from the surface tangent to the PMT surfaces. Within this region, however, there are severe anisotropies in the

¹The proton – neutron mass difference takes 1.2MeV. For ν from near the endpoint of the spectrum, the neutron recoil is, in the reaction rest frame, about $\frac{p^2}{2m_n} \approx \frac{50^2}{2 \cdot 940} = 1.3\text{MeV}$.

density of backgrounds, especially for the $\bar{\nu}_\mu \rightarrow \bar{\nu}_e$ search. Figure 5.1 shows the spatial distribution for a set representative of the background for the final decay at rest candidate sample. All the electron selection used in gathering this sample are looser than those for the final signal candidate sample by small amounts, and there is no requirement for a coincident gamma. The beam status flag is de-asserted for the positron candidates selected. The upper plots show the positions of the chosen positron candidates. In the lower set of plots in the same figure, the positions of all associated gamma candidates found in the 1ms windows after these events are shown. The left pair of plots show the X-Y projection of the detector, with the surface tangent to the PMTs shown as the thin arcs, except at the top and bottom, where it is the frame of the histogram. In the Y-Z projections (right plots) this surface is everywhere denoted by the histogram frame. Each shows a high density along the bottom of the tank, and toward negative \hat{z} .

An important background to any oscillation search is

the presence of beam unrelated processes while the beam is on, particularly, decay electrons from stopped muons in the case of the $\bar{\nu}_\mu \rightarrow \bar{\nu}_e$ search. Since data is taken irrespective of the beam status, the beam unrelated backgrounds can be measured accurately. Once the selection criteria are specified, one counts the number of events passing these cuts with the beam flag de-asserted, and scales by the duty factor. This simple procedure should work exactly in the limit of high statistics. When there is not a coincidence required, the issue of background density variation is not so crucial to the selection criteria. The regions of high density are fairly represented in the background that is subtracted. Beam related backgrounds are an entirely separate issue then, and can be calculated or measured independently. However, for the $\bar{\nu}_\mu \rightarrow \bar{\nu}_e$ oscillation search, there is a coincidence required and the background density gradients described above present a subtlety. Beam related backgrounds that would pass selection for one component of the tag can be drawn into the signal sample by beam unrelated processes providing random coincidences. The

case of interest here is when there is a real beam associated electron (from ν_e elastic scattering, or $\nu_e \text{ }^{13}\text{C} \rightarrow e^- X^2$ for example) in accidental coincidence with a random gamma. If the distributions of the random gamma rays are not the same throughout the detector, the definition of a “properly chosen cut” must account for this. Figure 5.2 shows the distribution of distance correlation for $e-\gamma$ pairs that were chosen by time and gamma energy to be almost certainly accidentals. There are three solutions to this gross variation of the distribution of random gamma rays:

One can (with enough statistics) characterize the exact spatial dependence of the distributions, and use these distributions as a function of position to describe a likelihood.

One can require that *all* of the characteristics of a candidate coincidence be “acceptable”.

One can simply avoid the regions where there is a significant departure from “average behavior”

² Approximately 1% of all carbon is ^{13}C . Its binding energy is only 2MeV more than that of ^{13}N , so electrons quasi-elastically scattered from it can carry off almost all of the energy of the incident neutrino.

of the distributions.

The path taken here is to follow both the second and third solution. The fiducial region used for the decay at rest search used in this work is shown in projection in figure 5.4. It is defined by the surface 50cm from the PMT faces, except in the Y coordinate, where it is bounded below by the plane $Y=-50\text{cm}$.

This choice of the exact value for the lower bound is not yet made clear from the data. Jumping ahead a bit, figure 5.5 shows the Y coordinate distribution for all the beam off events that pass all selection criteria for the final sample *except that on Y coordinate*. With the data histogram, there is a histogram of the phase space (basically just the shape of the tank) which is normalized so that the integrated number of events passing the Y cut ultimately used matches the number in the data. The error bars on the phase space histogram are the square root of the bin contents at each point. $Y = -50$ appears as the place where the background assumes a phase space distribution.

Concievably, there could be systematic reconstruction

effects which make the acceptance of a cut in the Y variable other than unity. This is tested by checking the distribution (compared to phase space) of the events at slightly lower energy from $\nu_e C$ quasielastic scattering.³ To first order, they should be distributed in Y as phase space. (The asymmetry from the relative position of the tank and beam is a less than 1% effect.) The results of this test are shown in table 5.1. They imply a less than 1σ effect in the fraction of events that fall in the upper part of the volume (above the $Y=-50$ cut). Since this is not a statistically significant effect no adjustment in the acceptance for signal is made, but the systematic error on the overall acceptance used in calculation of results takes this possible variation into account.

5.3 Selection based on previous events

For the decay at rest search, since there is a large (albeit beam unrelated) background from cosmic ray muon decay electrons, it is useful to make a stronger cut on previous ac-

³These events represent the largest sample of neutrino events that can be identified in LSND without requiring a coincidence.

tivity in the detector than the trigger requires. Also, since there are some thousands of $\nu_\mu C \rightarrow \mu^- X$ (and on order of $\frac{1}{10}$ that many $\bar{\nu}_\mu C \rightarrow \mu^+ X$) events induced by neutrinos from the pion decay-in-flight beam, cutting out electrons with unvetted previous activities is necessary. The trigger and data acquisition give enough information to allow precise cuts on only events with previous activities near in position as well as time, but a simpler, more conservative approach is to make a sufficiently strict cut on time alone so that involved arguments are not necessary. (The reconstruction for low energy muons is not as accurate as that for electrons.) The choice for a value of this time to any previous event is motivated by looking at the decay time plot for electrons with *detected* previous cosmic ray muons shown in (figure 4.2). This shows that (at least for the selections used for it) any background from detectable muons should be lower than constant random events in the detector after $35\mu s$. Therefor, making a cut at a larger value will affect signal and background the same way.

The efficiency for accepting signal type events for cuts

on previous events can be measured from the data. (Recall from section 4.1.1 that) There are laser events generated within the tank that are independent of any physics events.⁴ Like neutrino induced events, whatever occurs before them in the tank must be uncorrelated. One can apply the same cuts that will be used in the event selection to a sample of laser calibration events to measure the efficiency accurately. 65% of laser events pass the previous activity cut used for decay at rest oscillation candidate selection. (This same method is used to study the cuts on in-time veto shield activity with an event.)

5.4 Rejection for in-time veto system activity

The trigger condition that vetoes events from inclusion in the data stream is made as loose as possible without flooding the acquisition. To unambiguously tag neutrino events, a much stricter condition is required. Since the laser events allow deep studies of the effect of such cuts,

⁴To insure that the events taken are really laser generated events, a cut on distance to the nearest laser flask is used in addition to requiring that the tag be set.

the efficiencies are known quite accurately. (It is assumed in this argument, and in the numbers that follow that the dead-time due to on-line vetoing is dealt with separately.) Requiring no more than one veto system PMT signal within the 500ns window of an event is 87% efficient for acceptance of laser events.⁵ Reducing this to allowing none within the event reduces the efficiency to 58%. The standard criterion for electron selection used in this work will be “at most one” in-time veto system PMT. (The effect of tightening this will be presented also.) For correlated gamma candidates for the decay at rest search, up to 2 are allowed (93% acceptance).

5.5 Particle identification selection

The particle identification parameter used, and its energy dependence were discussed in section 4.3. The selection used for positron candidate events is that $\chi_{\text{PID}}^{\text{cor}} < 1$. This cut is 89% efficient for accepting signal like events,

⁵This assumes that the hardware efficiency has already been accounted for. This result is confirmed by studying the decay electrons of cosmic ray muons.

and about 99% efficient at rejecting non-relativistic backgrounds.

5.6 The choice to include only 1994 data

A large part of the choice to include only 1994 data in this analysis has to do with the energy dependence of the particle identification parameter. Figure 5.6 shows $\chi_{\text{PID}}^{\text{cor.}}$ versus energy for decay electrons of cosmic ray muons for some 1993 data. (This is an exactly analagous plot to figure 4.9, the only difference being when the data were taken.) There appears to be an energy dependence of the data for the *corrected* particle identification parameter.⁶ One could make a separate correction for data from each year (just as different energy calibrations are used for different sections of the data), but since there were only 30% as many protons on target in 1993 as in 1994, the simpler solution of independently analyzing the two years seems well motivated.

⁶This is understandable, at least qualitatively, since there were changes to the charge integrating circuits. The charge deposited in individual PMTs is the basis of the reconstruction fits, and therefor of $\chi_{\text{PID}}^{\text{cor.}}$ since it is constructed from the quality of fit parameters.

There were also small changes in the veto system between the two years, especially with respect to the bottom of the detector (as mentioned in section 3.3). The plastic scintillator “crack counters” that line the bottom edge of the detector were added between the two years. (— In part this was because the enhanced activity at the bottom was seen in 1993. The counters along the seam in the veto shield at the upstream end were in place during both runs.) The inclusion of these new counters forced some minute changes in the trigger logic to accomodate the new section of the veto system, and account for about $\frac{1}{2}\%$ of all the data written in 1994. Also, not all of the passive shielding was in place for the full 1993 run. These changes *should* not have noticeable effects on a low statistics search, but also provide some inclination to separate results from the two years.

One thesis has already been done (on the decay-in-flight search) using the 1993 data, [16]. This presented a result giving an upper bound of 0.023 on $\sin^2 2\theta$ at high Δm^2 , and $\Delta m^2 > 0.48\text{eV}^2$ for $\sin^2 2\theta = 1$.⁷ The conclusion of

⁷These values are from the plots in the conclusion of that work. The numbers given in

that work discusses possible bounds attainable with the statistics of the 1994 data set, in fair agreement with what is presented here for that channel.

5.7 Selection of correlated gamma rays

2.2MeV gamma rays from neutron capture on Hydrogen are selected based on the space and time correlation with the positron candidates, and on the visible energy of the gamma, as determined by the number of PMT signals in the detector for the gamma. In addition, there is a requirement that there be less than three veto system hit PMTs in time with the gamma, and no vetoed event occurring between (in time) the positron and the gamma. (This last requirement is to remove any ambiguity about the origin of the gamma. A conceivable scenario is that, after the positron candidate, a cosmic neutron enters the tank and is captured emitting a real 2.2MeV gamma ray. This is unlikely to pass the correlation cuts, but since it has the right energy, the associated accidental rate is dif-

the abstract are in error,[18].

ferent from that of truly random coincidences. The loss of acceptance due to this cut alone is very small, and is here given as part of the dead time.)

Figure 5.7 shows the average (over fiducial volume for electrons and over time throughout the run) properties for random coincidences and for capture gamma rays from cosmic neutrons. The distributions for accidental coincidences are gotten by histogramming the properties of the gamma rays occurring in the last quarter of the 1ms window (where the time distribution is flat). To study the properties of the capture gamma rays, the corresponding histograms are made for the first quarter of the millisecond, and the distributions subtracted (bin by bin). (The time and energy distributions shown here are the same as in figure 4.5.) In each plot, the vertical line represents the cut used in this analysis. The specific values of the selection criteria are: $d_{\gamma}^{(e)} < 2.4\text{m}$, $t_{\gamma}^{(e)} < 750\mu\text{s}$, and $N_{\text{PMT}}^{(\gamma)} \geq 25$. These cuts are 95, 98, and 90% efficient, respectively. The measured probability of having an accidental coincidence pass these criteria is 12%.

5.8 Signal event rates

The acceptances of the above listed cuts are all summarized in table 5.2. The overall efficiency for acceptance of signal is 25% within the 59m³ fiducial volume. The total flux of ν_μ produced at the beam dump is known to within 7% based on monte carlo calculations, and the spectrum at production known essentially exactly. Since the source is stopped muons, the “beam” is isotropic.⁸ The cross section for signal interactions is known to within 10%. (This is an interaction on a free nucleon; the cross sections for bound nucleons are considerably more difficult to model accurately.) The cross section as a function of neutrino energy can first be integrated over the range of “passing” positron energies separately to input into the integral.

For any point in the parameter space of $(\Delta m^2, \sin^2 2\theta)$ the number of expected events can be calculated by integrating the known flux of produced neutrinos times the oscillation probability times the cross section over energy

⁸The exact truth of this statement relies on the fact that the muons are unpolarized. This is the case, since the proton beam is unpolarized.

and distance. This can easily be integrated numerically, and then by multiplying the integral by the acceptance, the result is the expectation value for the measured signal level.⁹ A useful number to represent the result for rates is that if all $\bar{\nu}_\mu$ produced in the beam stop were instead $\bar{\nu}_e$, 1480 signal events would be detected with the selection presented here. Another way to say this is that at high Δm^2 if $\sin^2 2\theta = 1$ there would be 740 expected signal events detected.

5.9 Major $\bar{\nu}_\mu \rightarrow \bar{\nu}_e$ background sources

The numerically largest background for either oscillation search is the occurrence of beam unrelated events in time with the beam macro-pulse. The expectation level for this background is well measured since the beam status is not used for triggering. (See section 3.5.) 43 events occur with the beam off (as recorded in the status flag for the electron event) that pass all the selection criteria for $\bar{\nu}_\mu \rightarrow \bar{\nu}_e$ os-

⁹The variation in acceptance at the edges of the energy cut are also taken into account in the calculation. Since the integral is done numerically, this is a trivial change, but irrelevant to the general explanation.

cillation signal event candidates. The time with the beam flag asserted in the data set analyzed is 7.6% of the time with it de-asserted, so this implies 3.3 events with a statistical error of 0.5 is the background expectation for the beam on sample from this source. There is a systematic error of less than 0.05 event because there is some ambiguity about the exact duty factor for the data analyzed.

The second largest background in this search occurs when a neutrino (beam) induced electron occurs in accidental coincidence with an unrelated gamma ray in the detector. Several beam related processes contribute to this: Approximately 1% of all carbon is ^{13}C which has a binding energy of only about 3MeV. The quasi-elastic process $\nu_e \text{ } ^{13}\text{C} \rightarrow \text{e}^- \text{ } ^{13}\text{N}(\text{g.s.})$ has an endpoint near 50MeV, like that of oscillation signal events. Elastic scattering of electrons can occur from neutrinos from pion decay-in-flight or muon decay at rest giving electrons in the right energy range. There are other processes that also contribute, but they need not all be enumerated. The background for this type of source can be *measured* from the data by sim-

ply multiplying the beam excess of events with no gamma requirement by the measured probability of having an accidental coincidence with the given selection criteria. (For the selection used, this is 12%.)¹⁰ The measurements of these numbers give a background expectation of 2.5 ± 0.9 events. (The error is so large because there are many errors combined: measurement of numbers going into the accidental rate calculation; the beam on events seen without gamma rays are only 32; the beam off number; and finally the small systematic error on the duty ratio has been included added linearly to the rest.)

The expectation value for total background with the standard selection criteria applied is 6.2 ± 1.5 events. Table 5.4 shows the backgrounds predicted for several variations on the selection.

¹⁰With this definition, any true oscillation events with the neutron capture gamma undetected, but with an accidental coincidence would also be considered background. This is a self-consistent treatment since the efficiency of gamma detection is a factor in the acceptance of signal events.

Table 5.1: The effect of the “Y cut” on the $\nu_e C$ sample within $d^{\text{PMT}} < 50\text{cm}$. The fraction of events passing $Y > -50$ is found to be 0.68 ± 0.09 . The fraction of the volume represented is 0.72. A similar analysis of $\nu_\mu C$ quasielastic events finds 0.77 ± 0.07 passing the cut. The $\nu_e C$ sample is used because it is the largest sample of neutrino beam induced events in the data that can be selected without a coincidence requirement.

Region	# beam ON	# beam OFF	excess
Any Y value	472	3160	232 ± 22
$Y > -50$	209	661	159 ± 15

\Rightarrow fraction above cut = 0.68 ± 0.09 (stat. error)

(Phase space predicts 0.72)

Table 5.2: Synopsis of standard decay at rest candidate cuts. The effect of varying these selection on the results is shown in tables 5.4 and 5.5.

Total acceptance for final samples		
Cuts applied on	Acceptance	Definition
Fiducial region	59m ³	$d_{\text{e}}^{\text{PMT}} > 50 \text{ \& } y > -50$
Energy	(<i>definition of signal</i>)	$37 < E_{\text{e}} < 65\text{MeV}$
previous activity	65%	$\Delta(t)_{\text{prev. event}} > 35\mu\text{s}$ & $N_{\text{prev. evt.}(52\mu\text{s})} \leq 1$
in-time veto	87%	$N_{\text{PMT}}^{\text{veto system}} \leq 1$
Particle ID	89%	$\chi_{\text{PID}} > 0.1 \text{ \& } \chi_{\text{PID}}^{\text{cor.}} < 1$
Live time	81%	
Total for e \pm events	40%	(within this volume)
γ distance correlation	95%	$d_{\gamma}^{\text{e}} < 2.4\text{m}$
γ time correlation	98%	$t_{\gamma}^{\text{e}} < 750\mu\text{s}$
γ energy	90%	$N_{\text{PMT}}^{(\gamma)} > 25$
in-time veto for γ	93%	$N_{\text{PMT}}^{\text{veto system}}(\gamma) < 3$
Live time	80%	
Total for coincidences	25%	(within volume used)

Table 5.3: Major $\bar{\nu}_\mu \rightarrow \bar{\nu}_e$ backgrounds. Section 5.9 of the text has details on how these are measured or calculated. Note that the two largest, which account for over 90% of the total, are measured.

Source of neutrino	reaction in LSND	Expected #
Beam-unrelated background		3.3 ± 0.5
Beam induced e^\pm with accidental γ		2.5 ± 0.9
$\bar{\nu}_e$ contamination of $\bar{\nu}_\mu$ beam		
$\mu^- \rightarrow \nu_\mu \bar{\nu}_e e^-$	—	0.3 ± 0.1
$\pi^- \rightarrow e^- \bar{\nu}_e$	—	< 0.01
Miscellaneous backgrounds		
$\pi^- \rightarrow \mu^- \bar{\nu}_\mu$ in-flight	$\bar{\nu}_\mu p \rightarrow \mu^+ n$	0.04
$\pi^+ \rightarrow \mu^+ \nu_\mu$ in-flight	$\nu_\mu C \rightarrow \mu^- n X$	0.03
Total		6.2 ± 1.5

Table 5.4: Qualitative stability against changes in the decay at rest e^\pm selection. In each section of the table, one cut is varied while the others are left at their standard values (given in table 5.2). Errors on the background calculations and measurements are shown only for the standard case.

variable	cut used	# beam ON	backgrounds
Y coord.	$> -100\text{cm}$	7	8.8
	> -75	5	7.0
	> -50	5	6.2 ± 1.5
	> -25	5	4.9
	> 0	4	4.4
$d_{(e)}^{\text{PMT}}$	$> 35\text{cm}$	8	7.9
	> 50	5	6.2 ± 1.5
	> 75	3	2.6
	> 100	2	2.1
$\Delta(t_{\text{prev.}}^{(e)})$	$> 25\mu\text{s}$	27	30.
	> 35	5	6.2 ± 1.5
	> 52	4	4.7
$\chi_{\text{PID}}^{\text{cor}}$	< 1.5	8	9.3
	$< 1.$	5	6.2 ± 1.5
	< 0.5	5	4.7
	< 0	4	3.7
E_e	$> 35\text{MeV}$	7	7.4
	> 37	5	6.2 ± 1.5
	> 40	3	4.9
Veto PMT	≤ 1	5	6.2 ± 1.5
	$= 0$	4	5.0

Table 5.5: Qualitative stability against changes in the decay at rest gamma selection. See the previous table caption for an explanation.

variable	cut used	# beam ON	backgrounds
$N_{\text{PMT}}^{(\gamma)}$	$> 20(\text{no cut})$	8	9.2
	≥ 26	5	6.2 ± 1.5
	≥ 30	5	4.5
$t_{\gamma}^{(e)}$	$\leq 1\text{ms}(\text{no cut})$	6	8.0
	$\leq 750\mu\text{s}$	5	6.2 ± 1.5
	$\leq 375\mu\text{s}$	1	3.9
$d_{\gamma}^{(e)}$	<i>(no cut)</i>	17	15.1
	$\leq 2.4\text{m}$	5	6.2 ± 1.5
	$\leq 2.0\text{m}$	3	4.5
	$\leq 1.5\text{m}$	3	2.5
	$\leq 1.0\text{m}$	2	1.5

Figure 5.1: Projections of positions of background events. The fiducial requirement to get into this sample is only that the electron be reconstructed at least 30cm. from the PMT faces. For the gammas associated there is no fiducial cut.

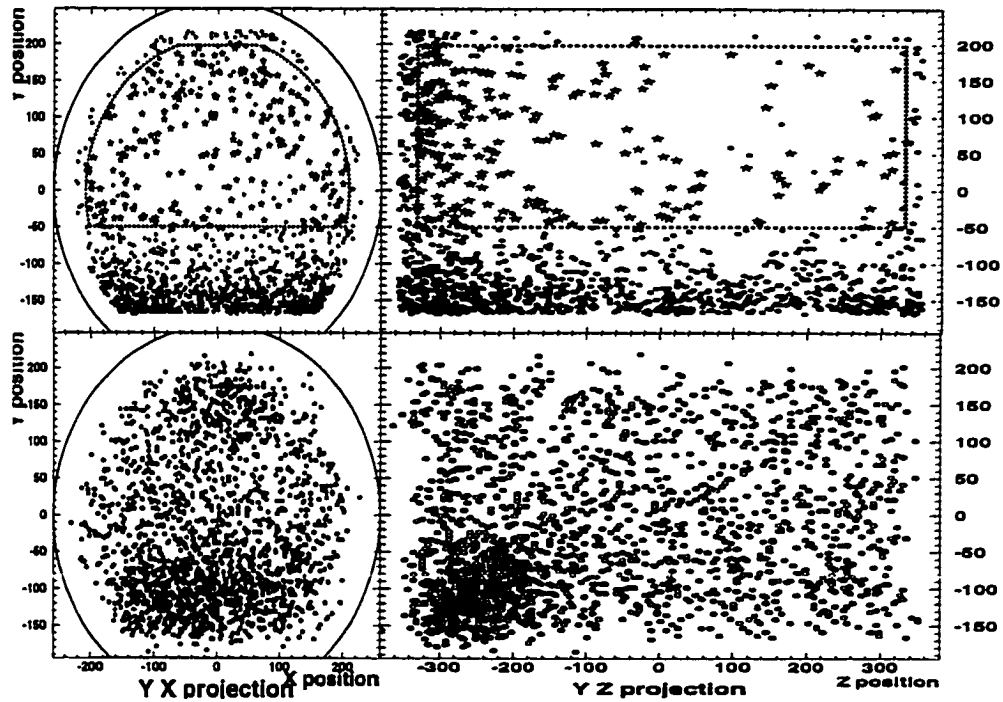


Figure 5.2: Electron - gamma correlation distance for accidental coincidences at several positions within the detector. The sample used to generate these distributions was one of primarily low energy beta decay primaries. The gammas are chosen by $t_{\gamma}^{(e)} > 700\mu s \& N_{PMT}^{(\gamma)} < 27$. The regions corresponding to each histogram are displayed in figure 5.3. The absolute rates shown here are irrelevant, but their relative values are meaningful.

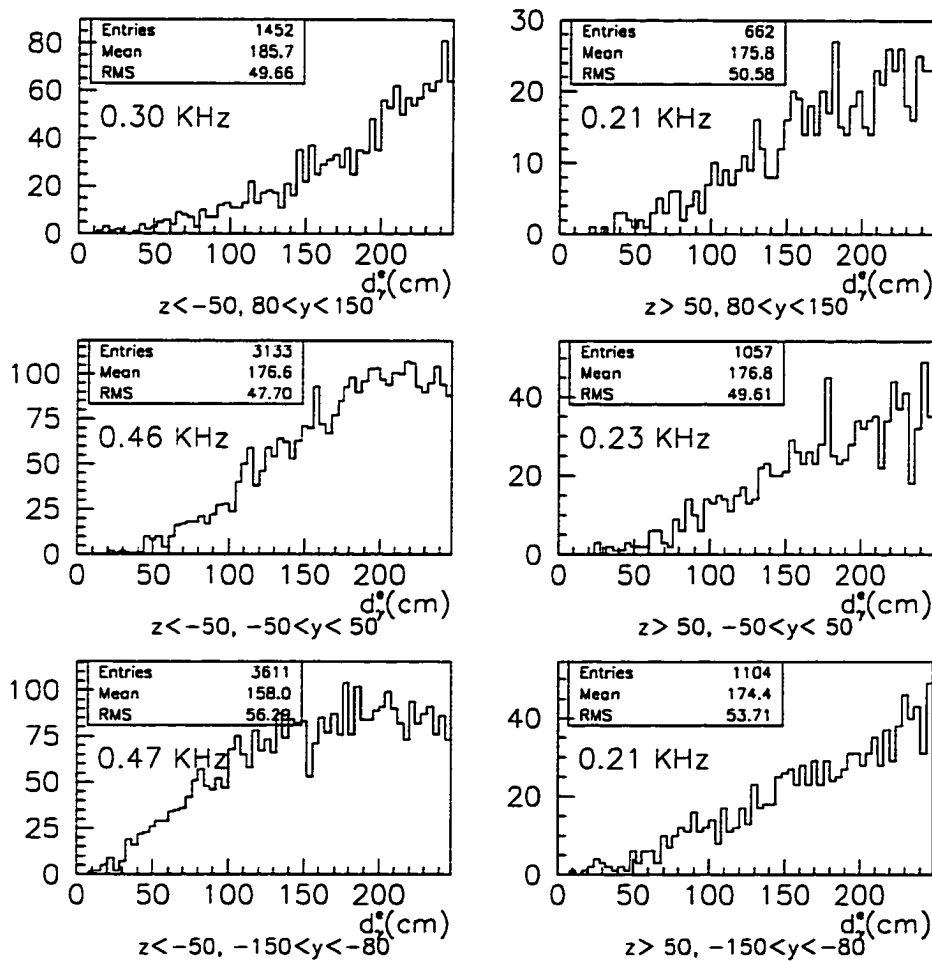


Figure 5.3: Regions used in figure 5.2 are the unshaded portions of this plot. The dots are the positions of the background gammas for the large background sample. (This is the same plot as figure 5.1, except for the shading.) Note that the selection is made on the *electron* position, not the gamma.

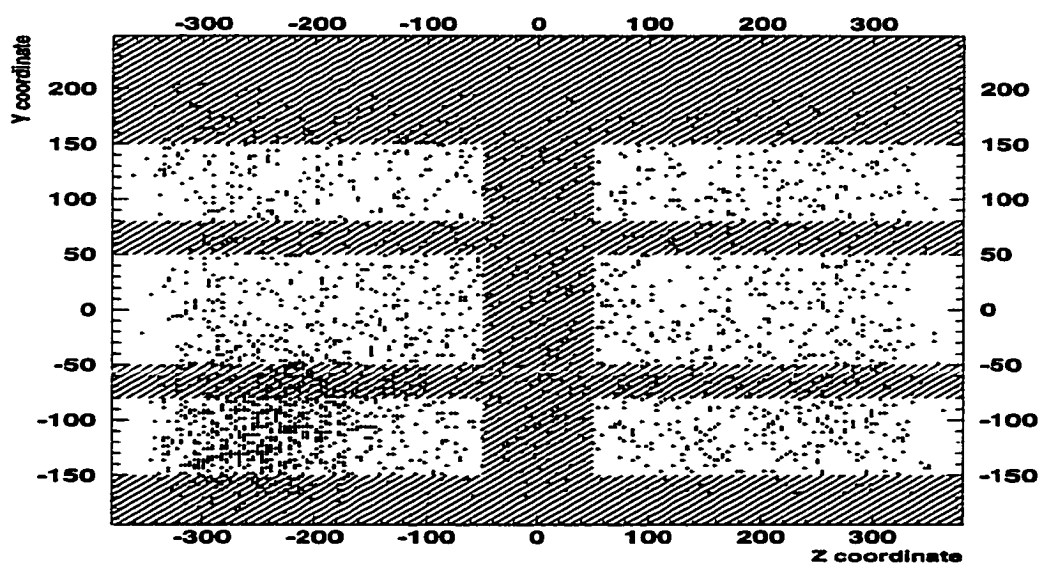


Figure 5.4: Fiducial region used for event selection in the decay at rest search. The two views are the Y-Z projection, and the Y-X. Remember that the beam is along $-0.17\hat{y} + 0.985\hat{z}$.

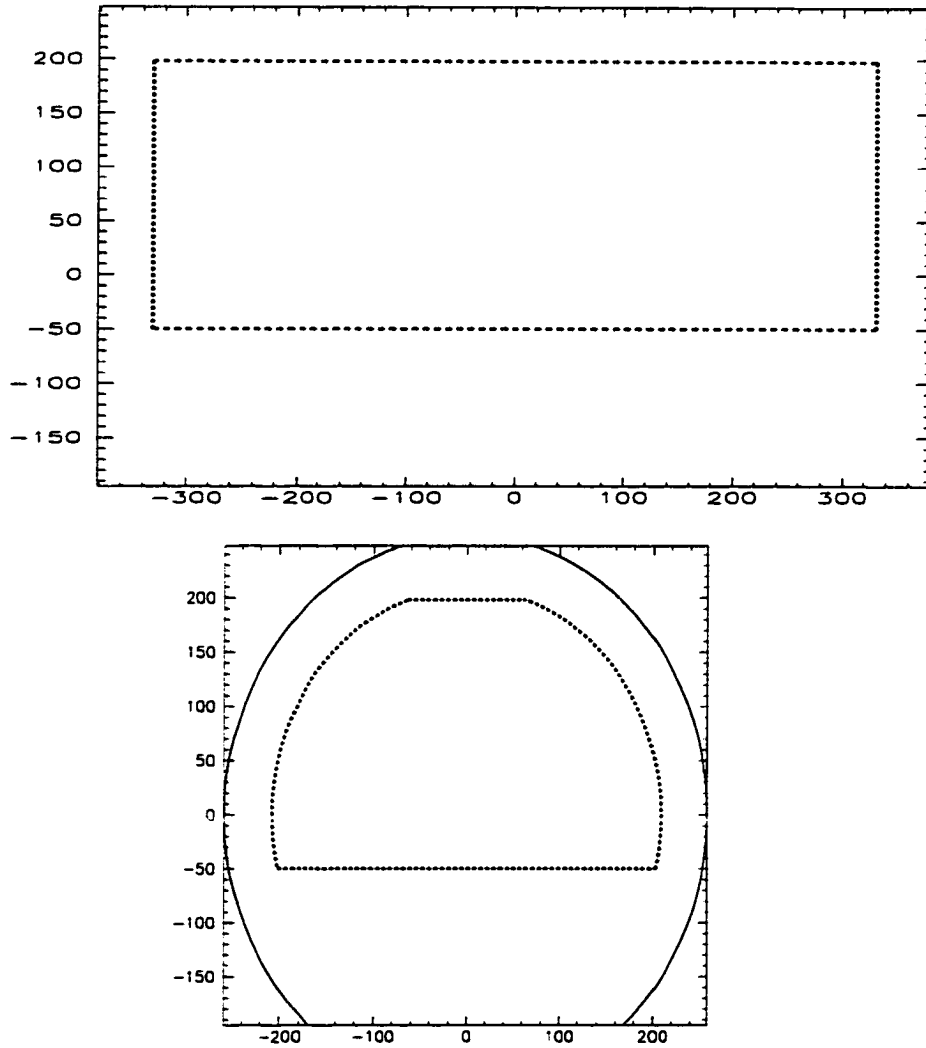


Figure 5.5: Y coordinate distribution for decay at rest background events. These events pass all final selection criteria (including gamma correlation requirement) except the cut on Y.

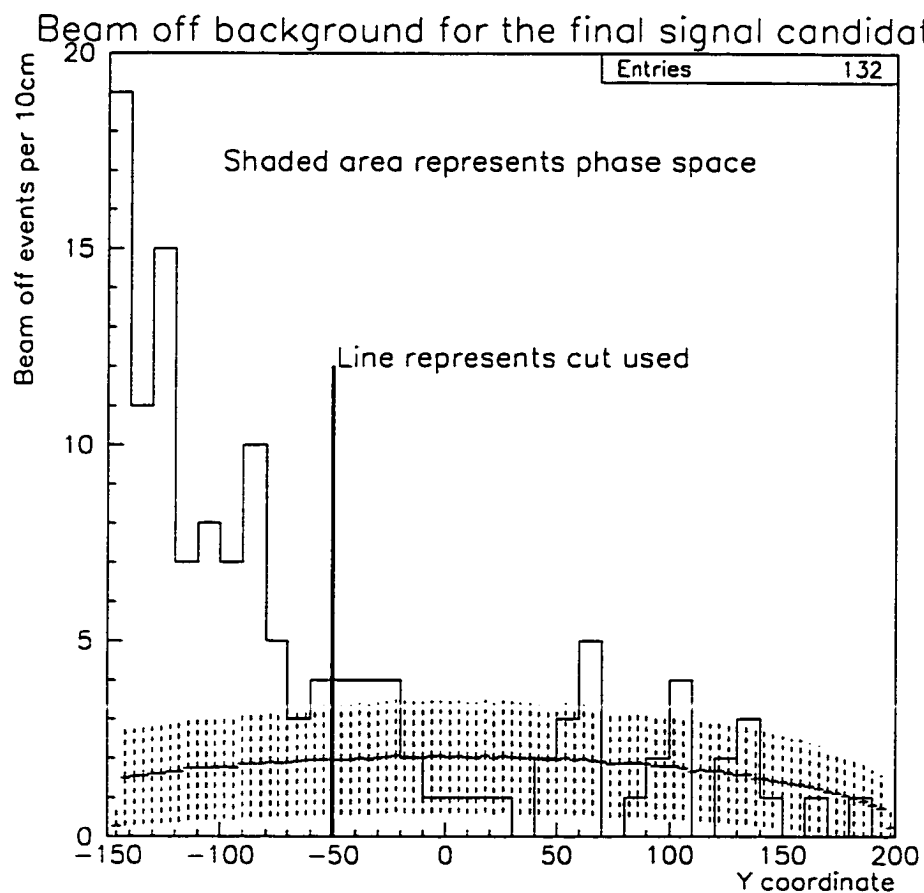


Figure 5.6: Decay electrons from cosmic ray muons in the 1993 data, showing the energy corrected particle identification parameter used in this analysis versus energy. Again, the cut used is shown as a solid line. A cut on the uncorrected parameter to get into this sample evinces itself as white space in the upper left. This figure should be compared to figure 4.9.

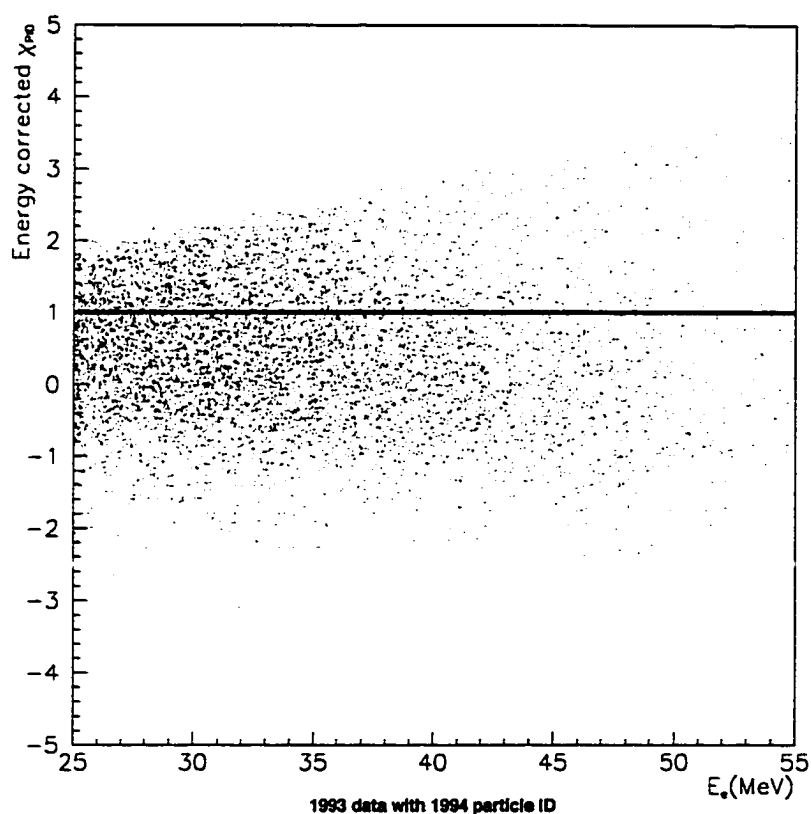
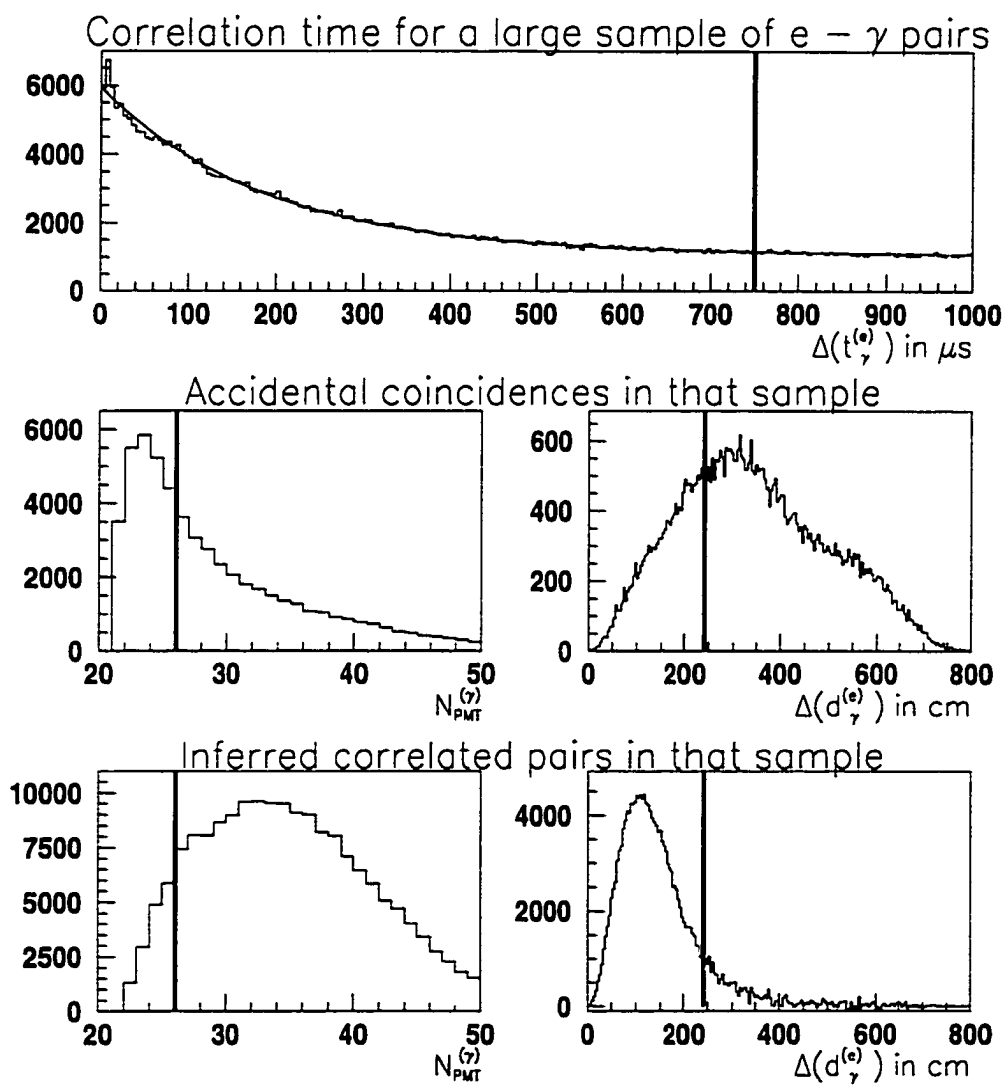


Figure 5.7: Average gamma properties used for selection. The top histogram shows the correlation time distribution for a large set of primary – gamma pairs. See text (page 100) for a description of how the capture gamma properties are derived.



Chapter 6

Selection of $\nu_\mu \rightarrow \nu_e$ event candidates

Here the final event selection criteria for $\nu_\mu \rightarrow \nu_e$ candidates is presented. The order of material will be similar to that of chapter 5, concluding with tables 6.1 and 6.3 to enumerate the exact criteria used, and show the invariance under perturbations of them. Since much of the motivation for cuts was explained in the previous chapter, the exposition will be somewhat briefer here.

6.1 Signal event signature

The reaction observed in the case of $\nu_\mu \rightarrow \nu_e$ oscillations is $\nu_e C \rightarrow e^- X$ for high (85 to 220MeV) energy neutri-

nos. The signature for these events in LSND is an isolated electron type event in the right energy range. Since the reaction occurs within the carbon nucleus, the kinematics is not as simple as in the decay at rest oscillation search and a model for the nuclear interaction must be employed. The nuclear interaction model used for cross section calculations is the (coulomb corrected) Fermi gas model which has been verified experimentally at lower energies by both LSND [19] and KARMEN [12].¹

The event signature is not as clear in this case as in the case of the decay at rest search. There is no coincidence required, and nuclear effects may obscure the nature of actual signal events. Even the acceptance for signal of the particle identification is not certain because of the extrapolation of the behavior from lower energy and because the nuclear effects occurring in signal interactions may make the final state unidentifiable. The general thrust of the

¹The application of the Fermi gas model for ν_e interactions on carbon in light of the published LSND result for ν_μ interactions on carbon [8],[7] is not an inconsistency. The high Q^2 value required for the production of the muon makes the reactions too different to compare. There is no compelling reason to expect the same model to apply to both. The experimental results are not a strong verification of the model, but are consistent with it.

analysis of this channel is to rely on the high statistics afforded by the loose definition of signal and the high cross section at this energy.

6.2 The fiducial region chosen

It was noted in section 5.2 that the main motivation for restricting the y coordinate of the fiducial region in the decay at rest oscillation search was the use of the coincidence tag between the positron and the neutron capture gamma. In this search, since there is no coincidence required, a larger volume is available to study. In this energy range, there is no direct evidence derivable from the data to guide the choice of a region at all. Monte carlo studies again imply that 50cm from the PMT faces is a reasonable fiducial boundary. This boundary encloses approximately 82m^3 . There seems to be an inward bias in the reconstruction at these energies, but only at the few percent level. This boundary encloses approximately 82m^3 .

6.3 Selection based on previous events

Since the endpoint of the muon decay spectrum is at only 52.8MeV there is no large background of micro-second time scale physics events, and strict cuts on time to previous event are not necessary. As in the decay at rest search, the requirement that there be at most one previous event in the 52 μ s history buffer is applied to require that the general state of the detector is “clean”. The acceptance is measured, as before, by checking the efficiency of the same requirement on laser events. It is 81%.

6.4 Rejection for in-time veto system activity

The same criterion for in-time veto activity is applied as for the low energy oscillation search: no more than one veto PMT signal in the time of the electron candidate. There is no evidence that the number of veto PMT signals in an event isolated within the main detector is energy dependent, so the acceptance for this criterion is the same as for the $\bar{\nu}_\mu \rightarrow \bar{\nu}_e$ search, 87%.

6.5 Particle identification selection

The same (energy corrected) particle identification parameter used for $\bar{\nu}_\mu \rightarrow \bar{\nu}_e$ oscillation candidates is used in the high energy search. (The point of the energy correction is that the acceptance for isolated electron type events is constant as a function of energy.) Figure 6.1 shows a scatter plot of the particle identification parameter versus energy for a large superset of the selected sample of $\nu_\mu \rightarrow \nu_e$ signal event candidates, and for the cosmic ray muon decay sample on the same plot. (The two data sets have been scaled for clarity.) The selection boundary is the horizontal line at $\chi_{\text{PID}}^{\text{cor}} = 1$. A lower bound on the uncorrected parameter was used for initial selection of the sample, and it is shown as a lower bound in the figure.² The high energy set is shown alone, projected on the $\chi_{\text{PID}}^{\text{cor}}$ axis in figure 6.2. The background is mostly non-relativistic (presumable hadrons). The separation between particles does not appear to be as good in this energy range be-

²This was to eliminate events for which no angle fit was done. Such events have $\chi_{\text{PID}}^{\text{cor}} = 0$, so a cut was made at 0.1.

cause muons emitting as much light as a 70MeV electron are relativistic, but not for as long as an electron. This creates a class of semi-relativistic backgrounds populating the intermediate values of the parameter.

There is possible new effect because the signal interaction is a nuclear interaction in carbon, and may produce an electron accompanied by nuclear material. If there is significant scintillation light from the accompanying particles, the Čerenkov cone and the fine time distributions will both contribute to make $\chi_{\text{PID}}^{\text{cor}}$ higher than for the isolated electron case. Since there is no other source of these interactions, one has to rely on the predictions of simulations and related but different processes. The relevant related process is $\nu_e \text{ }^{12}\text{C} \rightarrow e^- X$ where X is *not* the ground state of ^{12}N . This is the same reaction as the signal, but when initiated by the neutrinos from muon decay at rest is much less likely to have significant scintillation light from nuclear ejecta. (This is not only a statement about the nuclear physics; it is also a detector artifact. If there is only 35MeV to share among all the particles, since

protons emit about $1/3$ as much light as electrons of the same energy, events with a significant amount of energy in the proton are less likely to be seen at all.) The only possible indication that the particle identification might have lower acceptance than for isolated electrons is that the measured cross section for this process is about 20% lower than the Fermi Gas model predicts. This is within errors of the prediction, though, and very close to what KARMEN measures. On the basis of this, the efficiency of the particle identification is assumed unaffected (at a measurable level) by nuclear effects.

6.6 Signal event rates

The rates are calculated for this channel in essentially the same way as for the $\nu_\mu \rightarrow \nu_e$ search, but with some more complications taken into account. The energy dependence of the flux for neutrinos from the decay of pions-in-flight *is* a function of position in the detector. The neutrino fluxes are calculated in the monte carlo at a grid of points within the detector, and for this work they are av-

eraged over slices in Z coordinate over which the distance integration is done in calculating expected signal levels. Because of the high cross section at these energies and the large efficiency and fiducial volume, if all the pions that decayed-in-flight produced ν_e instead of ν_μ , 10,800 electrons would be detected as the signal. This is sufficient statistics so that this analysis is already background limited. Neutrinos from the decay of pions from the upstream targets are accounted for in the monte carlo fluxes used in calculating this rate, and are about 5% of the total.

Although the results presented will use the event rates calculated by a coulomb corrected Fermi gas model, alternative results using artificially lowered cross sections will also be shown. The production of muons through quasielastic neutrino scattering in this senergy range is observed to be about 1/3 of the prediction of the Fermi Gas model. The mass difference between the electron and the muon makes this a very different problem, but it is still a reasonable question to ask what would happen to the limits presented here if the electron production cross

section were also low by some factor from the model prediction. Data from KARMEN suggest that the predicted inclusive ν_e ^{12}C cross section is accurate to 20% in the energy range of neutrinos from muons decaying at rest. The average energy of ν_μ produced by pions decaying-in-flight at LAMPF is about 3 times as high, so it is conservative to assume that the cross section relevant to the $\nu_\mu \rightarrow \nu_e$ search cannot be more than a factor of two lower than the predicted value. This treatment of the uncertainty as “truly systematic” for this part of the analysis will be taken as a substitute for artificially enlarging the predicted error bars on the signal flux. The assumption that the Fermi gas model does not predict the correct cross section for the detection process will also affect some of the neutrino background calculations. For the work here, only the case of Fermi Gas model will be presented in detail, but the final result of the “low cross section model” will be presented for both the decay-in-flight channel search alone, and for the combined limit.³

³[20] uses values of cross sections reflecting half the Fermi Gas prediction. This accounts for the main difference between limits presented here and in that work.

6.7 Major $\nu_\mu \rightarrow \nu_e$ background sources

Except for the rather large background from beam unrelated processes, the main sources of background in this oscillation search are beam contamination sources. Since LSND cannot distinguish electrons from positrons, any source of ν_e or $\bar{\nu}_e$ in the right energy range is a beam contaminant. For some of these it is useful to give first order estimates here, although more precise calculations based on monte carlo fluxes and calculated cross sections are used in the final results and tabulated in table 6.2. In chapter 7, when final results are presented, a plot will be shown for the extreme case of considering only the beam unrelated background for this channel so that the results of the beam modelling are only necessary for the prediction of signal level.

The simplest limiting background for any experiment designed like this one is the pion decay channel $\pi \rightarrow \nu_e e$, which has a branching ratio of $(1.218 \pm 0.014) \cdot 10^{-4}$. Unless there are sufficient statistics to measure spectral deviations, this branching ratio defines an absolute lower limit

on the mixing level that can be detected. Scaling the predicted rate for signal presented above by this branching fraction, one expects about one event of this background to pass the selection used here.

Muon decay-in-flight results in high energy electron neutrinos also. If the spectrum and flight path were the same for the muons decaying in flight as for their parent pions, one would expect that the flux of ν_e from this background would be approximately $\frac{\tau_\pi}{\tau_\mu} \approx 0.01$. Since the muons have a shorter available flight path, and also have a broader angular distribution than the pions, the number of neutrinos that can come from μ decay-in-flight is somewhat less than this 0-order prediction. Also, the fact that the muon spectrum is softer, and their angular distribution more spread out makes the resulting neutrino angular distribution much more nearly isotropic. This means many fewer neutrinos from muon decay in flight reach LSND (since it is near the forward direction). The exact rate is sensitive to the details of the geometry of the beam stop area, and cannot be correctly calculated by such crude es-

timates. Using the monte carlo prediction for the neutrino flux from muons decaying in flight in the A6 area, 2.2 ± 0.5 events are expected from this background.

Pions and muons that are produced in the upstream target areas also contribute to the decay-in-flight neutrino fluxes. The only way to estimate the level of these backgrounds is to rely completely on the output of the beam monte carlo. The expectations calculated are 0.05 for events induced by neutrinos from decay of pions produced in the upstream targets, and 0.3 for those from muons. (The very long forward decay region available makes the probability of a muons decay in flight much higher in the upstream area.)

The total predicted background is 33.6 ± 2.5 events using the selection criteria described. The several variations of the selection presented in table 6.3 are presented with the total background prediction for each case.

Table 6.1: Synopsis of standard decay-in-flight candidate cuts. Results of varying the selection are shown in table 6.3.

Total acceptance for final samples		
Cuts applied on	Acceptance	Definition
Fiducial region	82m ³	$d_{\text{e}}^{\text{PMT}} > 50$
Energy	<i>(definition of signal)</i>	$70 < E_{\text{e}} < 200\text{MeV}$
previous activity	81%	$N_{\text{prev. evt.}}(52\mu\text{s}) \leq 1$
in-time veto	87%	$N_{\text{PMT}}^{\text{veto system}} \leq 1$
Particle ID	89%	$\chi_{\text{PID}} > 0.1 \ \& \ \chi_{\text{PID}}^{\text{cor.}} < 1$
Live time	81%	
Total	51%	(within this volume)

Table 6.2: Major $\nu_\mu \rightarrow \nu_e$ backgrounds. The “beam contamination sources” are all backgrounds the level of which depend on the Fermi Gas model cross section calculation.

Beam contamination sources	
Source of neutrino	Level expected
μ^\pm decay in A6 area	2.2 ± 0.5
$\pi^\pm \rightarrow e\nu_e$	$1. \pm 0.2$
μ decay in upstream areas	0.3 ± 0.1
π decay in upstream areas	0.05 ± 0.02
Other processes in detector	
reaction in LSND	Level expected
$\nu e \rightarrow \nu e$	0.5 ± 0.2
π^0 production	0.03
Beam unrelated background	
	29.6 ± 1.5
Total	33.6 ± 2.5

Table 6.3: Qualitative Stability against changes in the decay-in-flight electron selection. The same comments apply here as in table 5.4.

variable	cut used	# beam ON	backgrounds
$d_{(e)}^{\text{PMT}}$ Y coord.	$> 30\text{cm}$	47	44
	> 50	33	33.6 ± 2.5
	> 75	21	22
	<i>no cut</i>	33	33.6 ± 2.5
	$> -100\text{cm}$	28	24
	> -50	21	18
	> 0	17	13
$\chi_{\text{PID}}^{\text{cor.}}$	< 2	48	50
	< 1.5	42	41
	$< 1.$	33	33.6 ± 2.5
	< 0.5	19	25
	< 0	12	19
$\Delta(t_{\text{prev.}}^{(e)})$	<i>no cut</i>	33	33.6 ± 2.5
	$> 15\mu\text{s}$	31	33
	$> 25\mu\text{s}$	29	29
	> 52	21	21
E_e	$> 65\text{MeV}$	45	45
	> 70	33	33.6 ± 2.5
	> 80	27	27
	> 100	24	22
E_e	$< 250\text{MeV}$	45	44
	< 200	33	33.6 ± 2.5
	< 150	21	23
Veto PMT	≤ 1	33	33.6 ± 2.5
	$= 0$	23	22

Figure 6.1: $\chi_{\text{PID}}^{\text{cor}}$ versus energy for both electrons from muon decay, and a superset of the decay in flight oscillation candidates. The upper and lower cut boundaries are shown as solid lines. Figure 4.10 showed the behavior of this parameter for electrons and for other events in the range from 25 to 65MeV.

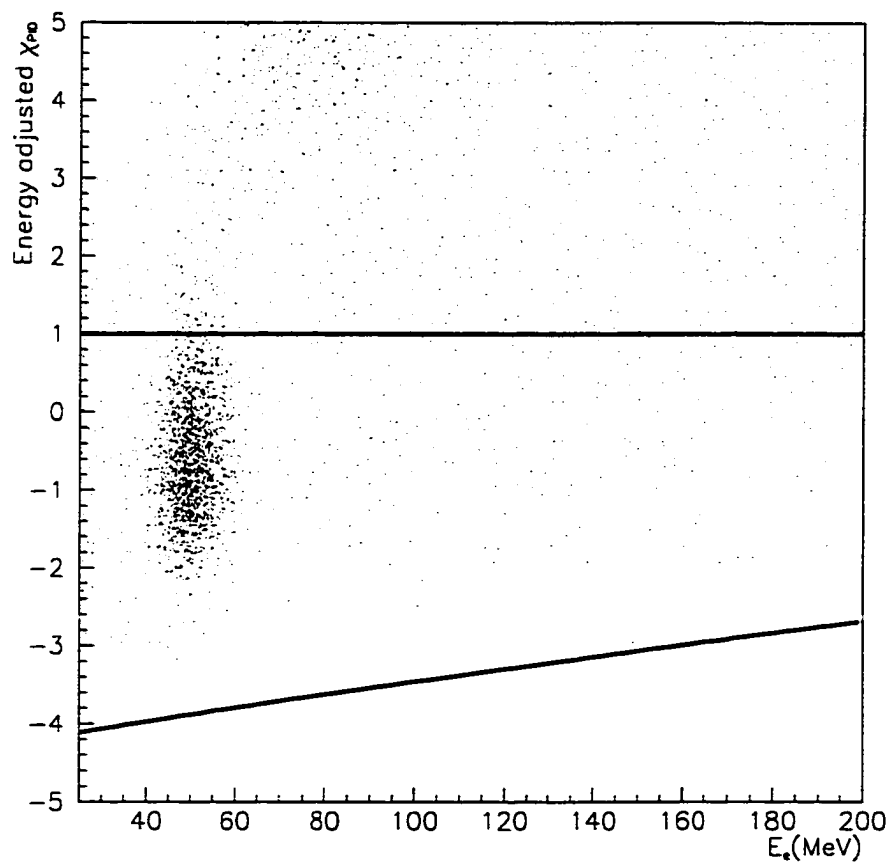
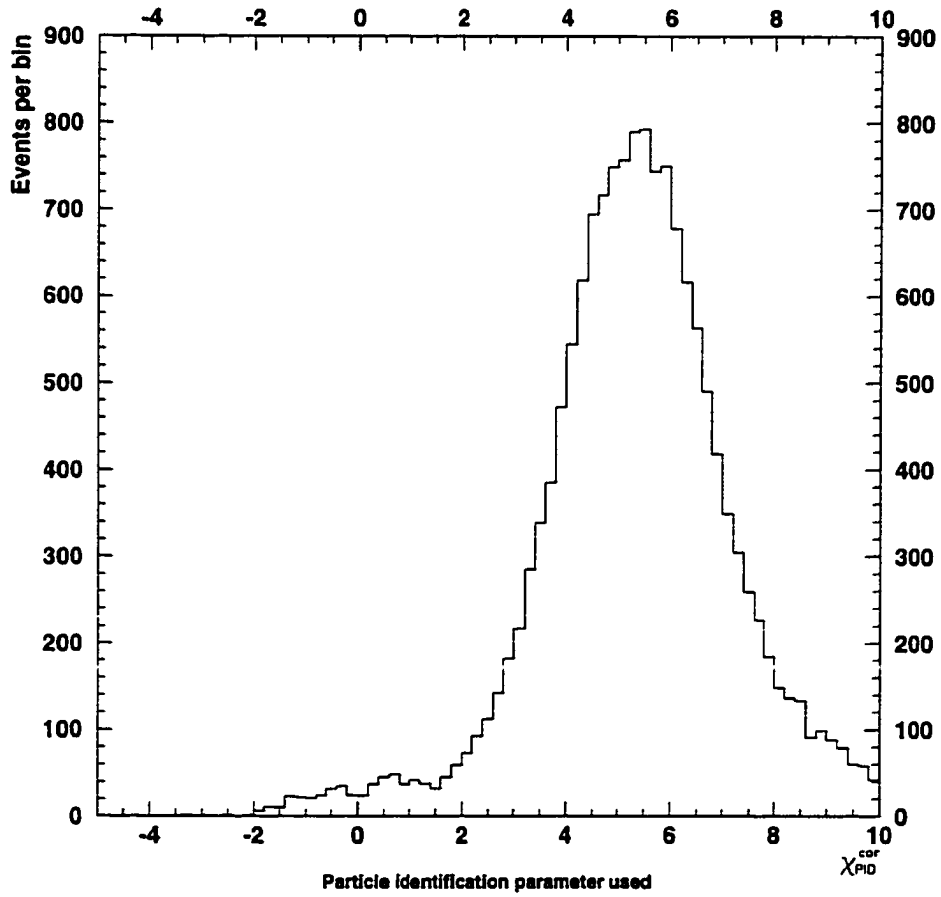


Figure 6.2: $\chi_{\text{PID}}^{\text{cor}}$ for a superset of the final $\nu_\mu \rightarrow \nu_e$ candidates. The value used as an upper bound on this variable in event selection is 1.



Chapter 7

Data analysis and results

In this chapter, after reviewing the statistical methods used, we first present the limits on the level of signal in the two oscillation search channels in an (almost) model independent way. These are then expressed as separate limits on the mixing parameters Δm^2 , and $\sin^2 2\theta$. Then, the two measurements are treated as part of a single experiment, and the resulting excluded region of parameter space is presented.

7.1 Statistical methods

For analysis of each of the separate channels, the approach outlined in the Particle Data Book [14] for Poisson

statistics can be used to derive a limit on the total number of $\bar{\nu}_e$ or ν_e induced events observed. This limit can be interpreted directly as a limit on the branching ratio for the lepton family number violating decay $\mu \rightarrow \nu_\mu \bar{\nu}_e e$ in the case of the $\bar{\nu}_\mu \rightarrow \bar{\nu}_e$ search. Similarly, the results for the $\nu_\mu \rightarrow \nu_e$ search can also be applied to place limits on the decay $\pi \rightarrow \nu_e X$ or $\pi \rightarrow \bar{\nu}_e X$. That prescription reduces to solving the following equation for $\mathcal{S}(\Delta m^2, \sin^2 2\theta)$:

$$\begin{aligned} (1. - \text{C.L.}) \sum_{i=0}^{\mathcal{O}} \frac{\mathcal{B}^i}{i!} \\ = e^{-\mathcal{S}(\Delta m^2, \sin^2 2\theta)} \sum_{i=0}^{\mathcal{O}} \frac{(\mathcal{B} + \mathcal{S}(\Delta m^2, \sin^2 2\theta))^i}{i!} \end{aligned} \quad (7.1)$$

where \mathcal{O} is the observed number of (possibly signal) events, and $\mathcal{S}(\Delta m^2, \sin^2 2\theta)$ and \mathcal{B} are the predicted signal and background numbers respectively.

This prescription “automatically” takes care of statistical errors, but has no built in mechanism for dealing with systematic errors. In the limit of large statistics, (although the fractional error from statistics will be small) the absolute value of the statistical error will dominate any systematics, and this procedure will be correct. An improvement

for low statistics is to integrate each side of equation 7.1 over the “background” variable, weighting by the relative probability of that value for background. The simplifying assumption used for implementing this technique is that the systematic error on the background is gaussian. This is seldom a good assumption, but still an improvement over ignoring the systematic errors altogether. For both the results given here this improvement turns out to be numerically negligible. Another way to address the systematic errors (which is perhaps less mathematically well motivated, but more intuitive) is to just repeat the analysis with the backgrounds all artificially lowered by the stated systematic error. Results thus derived will be shown for each oscillation search.

A different approach to the same data is to construct a χ^2 variable as a function of the point in parameter space considered. A simple least squares method gives for either oscillation search:

$$\chi^2(\mathcal{S}) = \left(\frac{\mathcal{S} + \mathcal{B} - \mathcal{O}}{\text{total error}} \right)^2$$

$$\approx \frac{(\mathcal{S} + \mathcal{B} - \mathcal{O})^2}{(\sigma_{\mathcal{S}} + \sigma_{\mathcal{B}})^2 + \mathcal{O}} \quad (7.2)$$

This assumes gaussian errors on the signal and backgrounds, and on the observation. (This is wrong for the signal and observation because at low levels Poisson errors should be used. However, even for 6 events (the background level for the decay at rest search), a Poisson distribution converges toward gaussian and since the largest errors will dominate the approximation is never bad.) The great power of this technique is that it is immediately applicable to the combination of data sets. Under the (physical) assumption that the sets can be combined meaningfully, limits in the two parameter space of Δm^2 and $\sin^2 2\theta$ are set by drawing contours in:

$$\chi^2(\Delta m^2, \sin^2 2\theta) \equiv \sum_{channel} \frac{(\mathcal{S}(\Delta m^2, \sin^2 2\theta) + \mathcal{B} - \mathcal{O})^2}{(\sigma_{\mathcal{S}} + \sigma_{\mathcal{B}})^2 + \mathcal{O}} \quad (7.3)$$

Here, the 2 “channels” summed over are the 2 oscillation searches done, and of course the signal, background, and observation are all different for each element of this sum.

Since there are two (almost) independent measurements and two parameters for the fit, there are 0 degrees of freedom, and the confidence levels are defined by:

$$\chi^2(\text{C.L.}) = \chi_{\min}^2 - \log(1 - \text{C.L.}) \quad (7.4)$$

More conservative limits are obtained by considering this as having one degree of freedom (since the two parameters appear only as a single combination) as in [21]. The results of treating the χ^2 as having one degree of freedom will be shown for comparison as well,¹ and used in comparisons to the data of other experiments.

The only necessary improvement to this prescription for the derivation of confidence levels is the incorporation of the off-diagonal elements of the error matrix to account for the correlations in the beam flux calculation. The estimates for uncertainties in the total muon decay at rest flux and the pion decay-in-flight flux are essentially perfectly correlated. Each flux is the product of the total magnitude of pion production times the fraction of either pions that decay-in-flight, or those that do not. The frac-

¹Numerically, there is not much difference between the results of the two methods.

tion that decay in flight is (to first order) independent of the total pion flux.

7.2 Two separate limits

Here the formulae in section 7.1 are used to get quantitative limits on the observed numbers of signal events in each neutrino search. While mention is made of the application of these limits to the branching ratios of certain lepton number or lepton family number violating decay modes of pions and muons, the main emphasis is kept on oscillation bounds.

7.2.1 Mixing limit for $\bar{\nu}_\mu \rightarrow \bar{\nu}_e$

The selections presented in chapter 5 left 5 candidate events for $\bar{\nu}_\mu \rightarrow \bar{\nu}_e$ oscillation signal. Applying equation 7.1 to the observation of 5 events with the predicted background of 6.2 excludes theories that predict more than 4.6(5.8) events at the 90(95)% confidence level. The effect of integrating over a gaussian smearing of the background is insignificant at this precision. This excludes a branching

ratio of $> 3(4) \cdot 10^{-3}$ for the decay process $\mu \rightarrow \nu_\mu \bar{\nu}_e e$, if the $\bar{\nu}_e$ spectrum from the decay is the same as the $\bar{\nu}_\mu$ spectrum in the conventional decay. If the spectrum is that of the ν_e in the regular mode (*I.e.*: the Michel spectrum of parameter 0), these limits are higher by a factor of 1.8 because of the rising neutrino quasielastic cross section.²

To draw the 90% confidence level exclusion plot for this limit, the contour $(4.6 + 6.2 =)10.8$ is plotted for the generated surface of predicted signal + background as a function of $\sin^2 2\theta, \Delta m^2$). This contour and the corresponding 95% confidence level are shown in figure 7.1. Figure 7.2 shows the result of the naive approach to dealing with systematic errors in this search. The limits shown are calculated using the same measured signal and predicted flux, but with a background of $(6.2 - 1.5 =)4.7$. The result here is shown to illustrate that even a significant miscalculation of the background gives a similar result in the parameter space. (Even treating the channel as though there were no background, and solving 7.1 for the level of excluded

²These limits are significant compared to what is currently in the Particle Data Book listings, but the new results from KARMEN,[23] are more strict.

signal puts the 90% exclusion curve at $\sin^2 2\theta < 1.2 \cdot 10^{-2}$ for large Δm^2 .)

7.2.2 Mixing limit for $\nu_\mu \rightarrow \nu_e$

The selection of chapter 6 for the $\nu_\mu \rightarrow \nu_e$ search left 33 events in time with the beam as possible signal candidates. Equation 7.1 with 33 observed events and 33.6 background excludes theories predicting more than 10.5(12.7) at the 90(95)% confidence level. The resulting exclusion curves are shown in figure 7.3. Figure 7.4 shows the result of repeating the analysis with the neutrino backgrounds all ignored (which is numerically similar to lowering the total background by one standard deviation).

The final special case to consider in this channel is the effect of a lower cross section for the neutrino quasi-elastic scattering. Figure 7.5 presents the limit obtained by assuming the number of signal events predicted for any point in parameter space is 1/2 of its calculated value. Most of the backgrounds are also lower by the same assumption, so the effect is slightly different from the effect of *just* scaling

the predicted signal flux.

There are lepton family number violating decays of pions that have never been observed, and the branching ratios of which may be further bounded by these data. In particular, the Particle Data Book gives (90% confidence) limits on the branching ratio for $\pi^+ \rightarrow \mu^+ \nu_e$ of $8 \cdot 10^{-3}$. The limit on this branching ratio from these data is exactly half of the high mass splitting limit shown in the oscillation parameter exclusion plot, 10^{-3} if the Fermi Gas model cross section is correct.

7.3 The combined limit

The data from the two searches are combined using equation 7.3 to produce exclusion curves for mixing between muon and electron type Dirac neutrinos in the limit that tau type are decoupled from them. Figure 7.6 shows the 90 and 95% confidence levels using contours corresponding to 0 degrees of freedom. The more restrictive statistical treatment of using 1 degree of freedom yields the limits shown in figure 7.7. The “low cross section model”

for the decay-in-flight search can be used together with the decay at rest data to give combined limits also. (Since the decay at rest detection is via scattering on a free nucleon, the Fermi Gas model is not used in the cross section calculation, and this data does not change.) The result of combining these data are shown in figure 7.8. By combining the two results, the values of Δm^2 that were less sensitive in either search are more strongly represented, and the high Δm^2 limit is strengthened by the increase in statistical significance. The Fermi Gas model cross section limit is shown again in figure 7.9, along with limits published by KARMEN and BNL-E776.

7.4 Improving on these limits

The effect of more data can easily be explored by scaling the backgrounds for the data at hand, and adding this number of events to both the background and the observation. Figure 7.11 shows the region probed with twice the data analyzed here. If there is no new observation of signal, this will be the limit derived by repeating

the present analysis. More carefully stated, the curves show the region of parameter space that will be probed by the addition of more data (since this data has nothing to say about whether the parameters in the “predicted excluded region” might be the physical parameters of neutrino oscillations.) The effect is basically to increase the ratio of predicted signal events for a given point in parameter space linearly, while (assuming no signal and constant backgrounds) increasing both the observation and background linearly. This, in the limit of gaussian errors (which is not a bad approximation) effectively moves the contours of the exclusion plots to lower values of $\sin^2 2\theta$ as the square root of the amount of data.

Another approach to enlarging the region of parameter space which LSND is capable of probing is to move the detector. (This idea has been discussed by the collaboration several times.) This allows the experiment to probe lower values of Δm^2 . At the lowest values of this parameter accessible to an experiment, the term in the equation for oscillation probability (equation 1.3) that depends on

Δm^2 can be approximated by replacing the sine with its argument:

$$\sin^2 2\theta \sin^2 \left(1.27 \Delta m^2 \frac{L}{E} \right) \approx \sin^2 2\theta \left(1.27 \Delta m^2 \frac{L}{E} \right)^2$$

giving a term rising quadratically in distance from source, which exactly cancels the $\frac{1}{r^2}$ loss of flux. This means that while the neutrino backgrounds for the $\bar{\nu}_\mu \rightarrow \bar{\nu}_e$ search are becoming suppressed, any potential signal is not, so not only is the region of parameter space probed extending to lower values of Δm^2 , the search is getting cleaner. At great distances, this might even allow lowering the energy threshold for the search, thus probing even lower values of Δm^2 . In principle, this applies to any distance, as long as Δm^2 is “small” for that distance.³ (*I.e.*: $1.27 \Delta m^2 \left(\frac{L}{E} \right) \ll \frac{\pi}{4}$.) To have a realistic detection, however, other neutrino events should be detectable so that the systematic detector effects are still credibly under control. More than tripling the distance makes statistically significant detection of $\nu_e C$ events from neutrinos from muon decay at rest impossible

³For $\Delta m^2 \approx \mathcal{O}(10^{-5} \text{eV}^2)$, $\sin^2 2\theta \sim 1$, near the “large angle solution” for the solar neutrino problem, a few events from the LAMPF neutrino beam might be seen in LSND if it were moved to the present KARMEN site.

without more than a year's run. Since the decay at rest beam is isotropic, one could move LSND *down* underground so there is increased shielding against cosmic rays. This is not realistically foreseeable because of the cost of excavation. Reactor experiments can explore this region of parameter space much more cheaply (but are constrained to be $\bar{\nu}_e$ *disappearance* searches, and must rely totally on calculated fluxes for any result). Whether using a reactor for a disappearance experiment, or LSND (or something like it) for an appearance experiment, the effect of moving far from the source is to probe lower values of Δm^2 , but at the expense of statistics at higher values which are what allowed the probing of low values of $\sin^2 2\theta$.

The strength of LSND that drove the proposal was its ability to study values of $\sin^2 2\theta$ nearly as low as the branching fraction $\frac{\Gamma_{\pi \rightarrow \nu e}}{\Gamma_{\pi \rightarrow \nu \mu}}$. With another 4 month run, it will still be almost an order of magnitude from this limit, but have nearly exhausted its potential for improvement in that parameter. The limit it sets is already useful (in the sense that it is stronger than existing limits), and it

has contributed to the general understanding of neutrino interactions [8, 7].

Figure 7.1: Excluded region of Δm^2 vs. $\sin^2 2\theta$ for the decay at rest channel when considered as a single measurement. (I.e.: integrated over the spectrum.) The two curve shown are the 90 and 95% confidence levels for exclusion of parameters. The region above and to the right of the curves is ruled out.

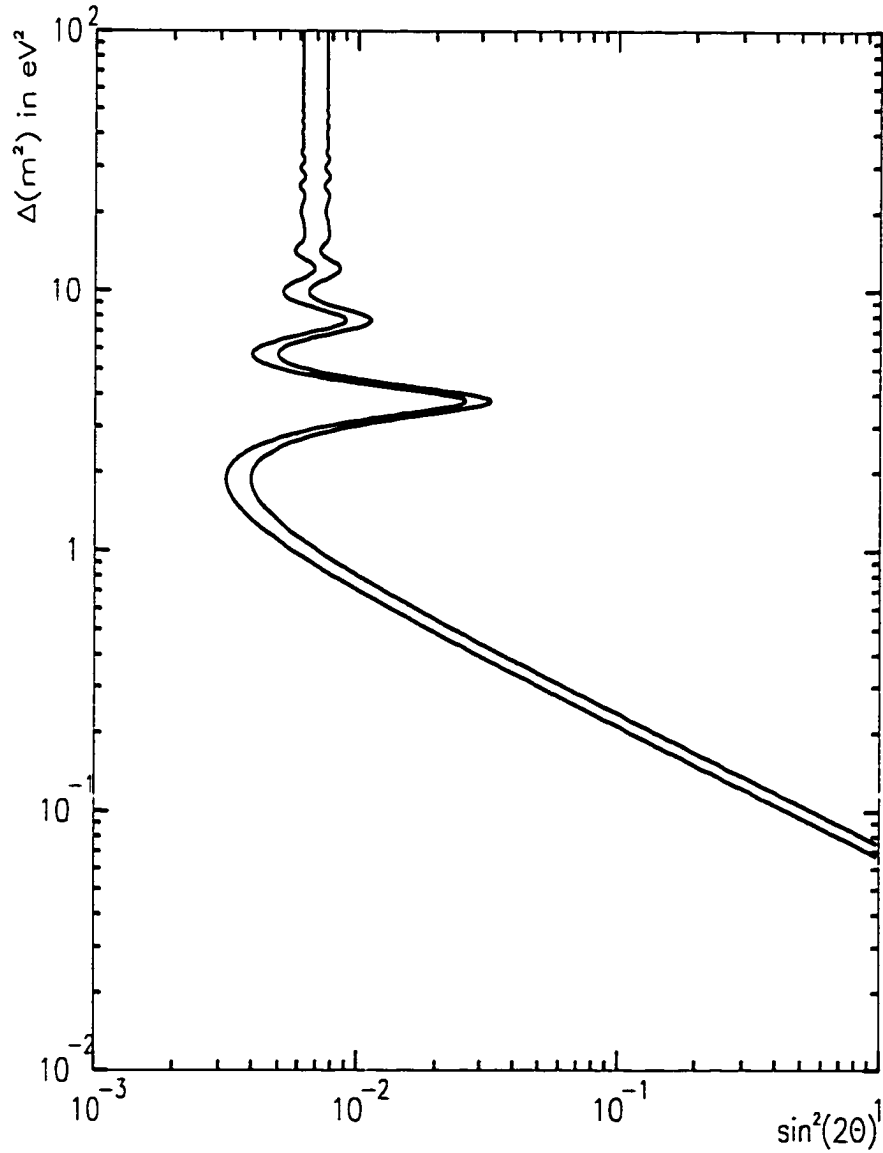


Figure 7.2: $\bar{\nu}_\mu \rightarrow \bar{\nu}_e$ exclusion plot for case of lower background. The total background level is taken as the prediction from table 5.3 -1σ , and the analysis repeated as for figure 7.1.

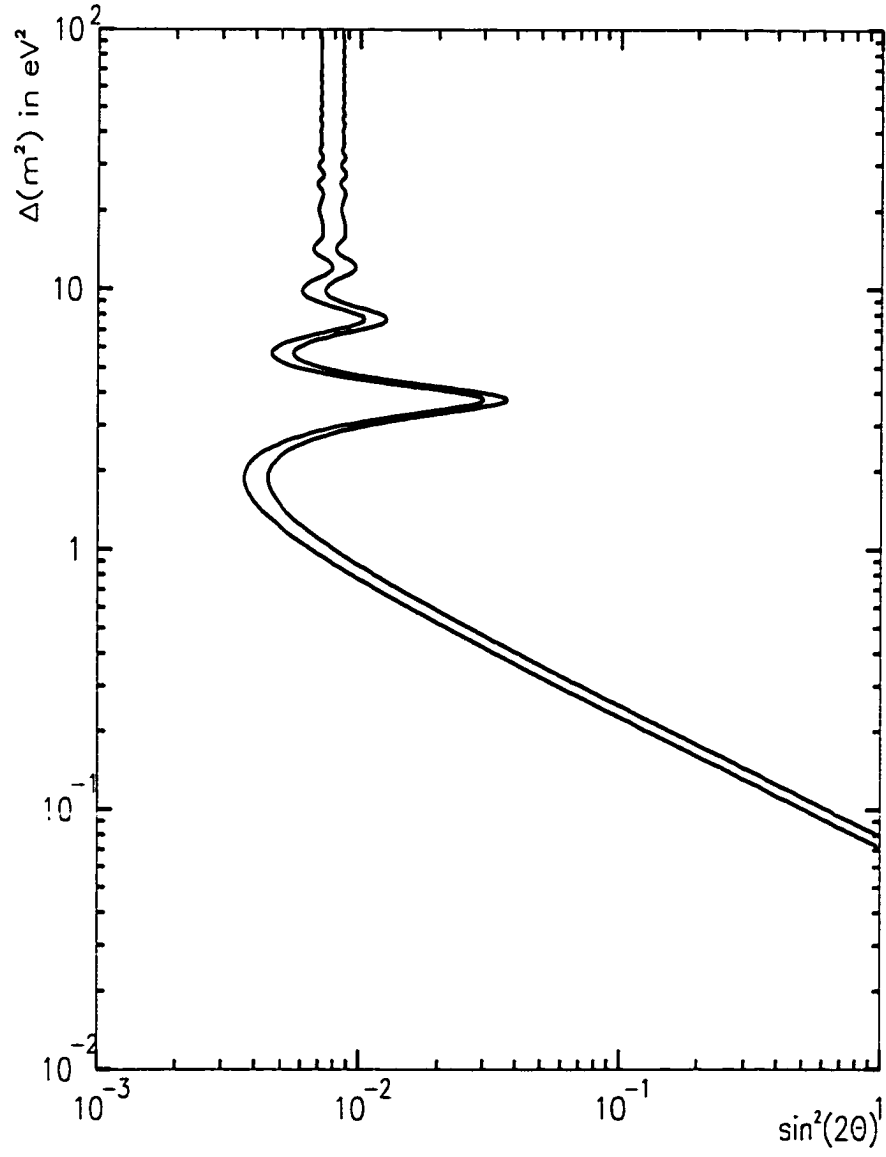


Figure 7.3: Excluded region of Δm^2 vs. $\sin^2 2\theta$ for the decay-in-flight channel when considered as a single measurement.

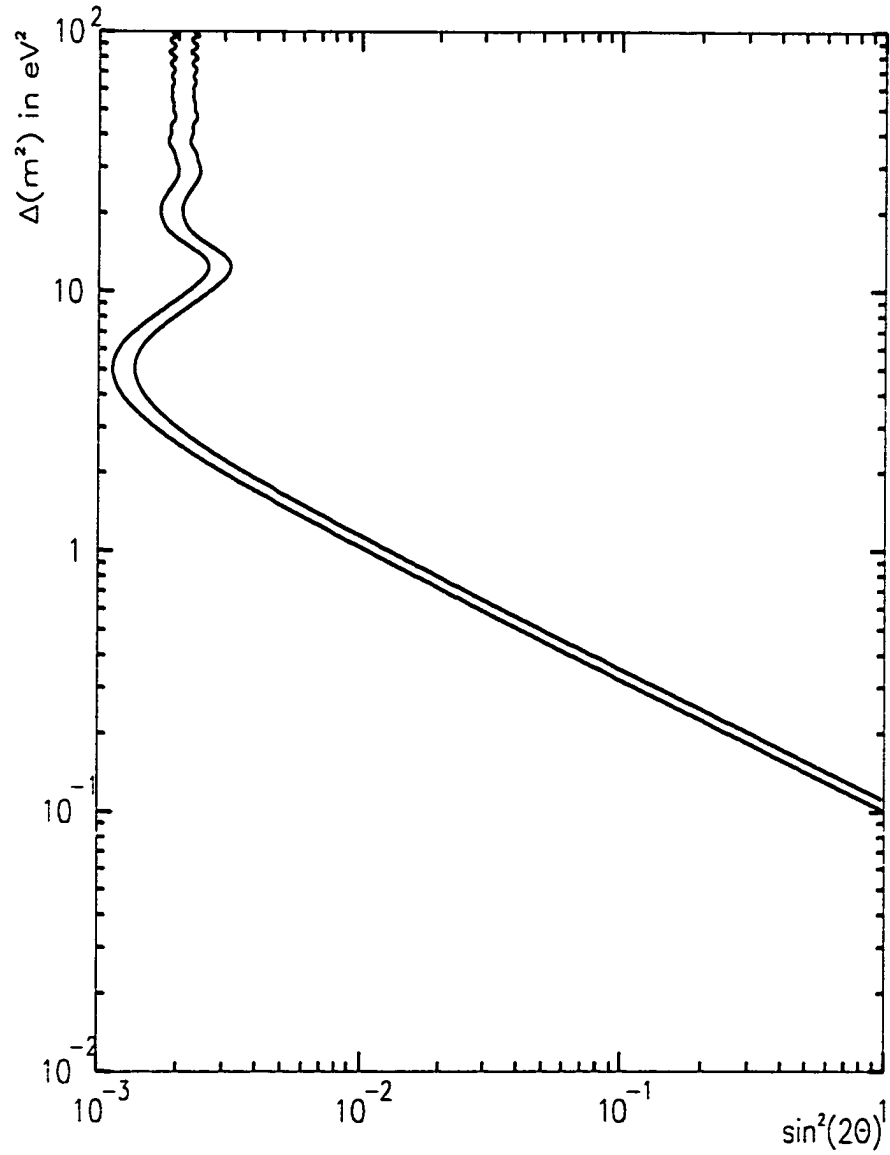


Figure 7.4: Weaker $\nu_\mu \rightarrow \nu_e$ exclusion assuming no ν backgrounds. The only use of the beam monte carlo is to get the predicted signal flux. Since the major background is from beam unrelated processes, these limits differs from figure 7.3 by a factor of about 1.2 in the high Δm^2 limit.

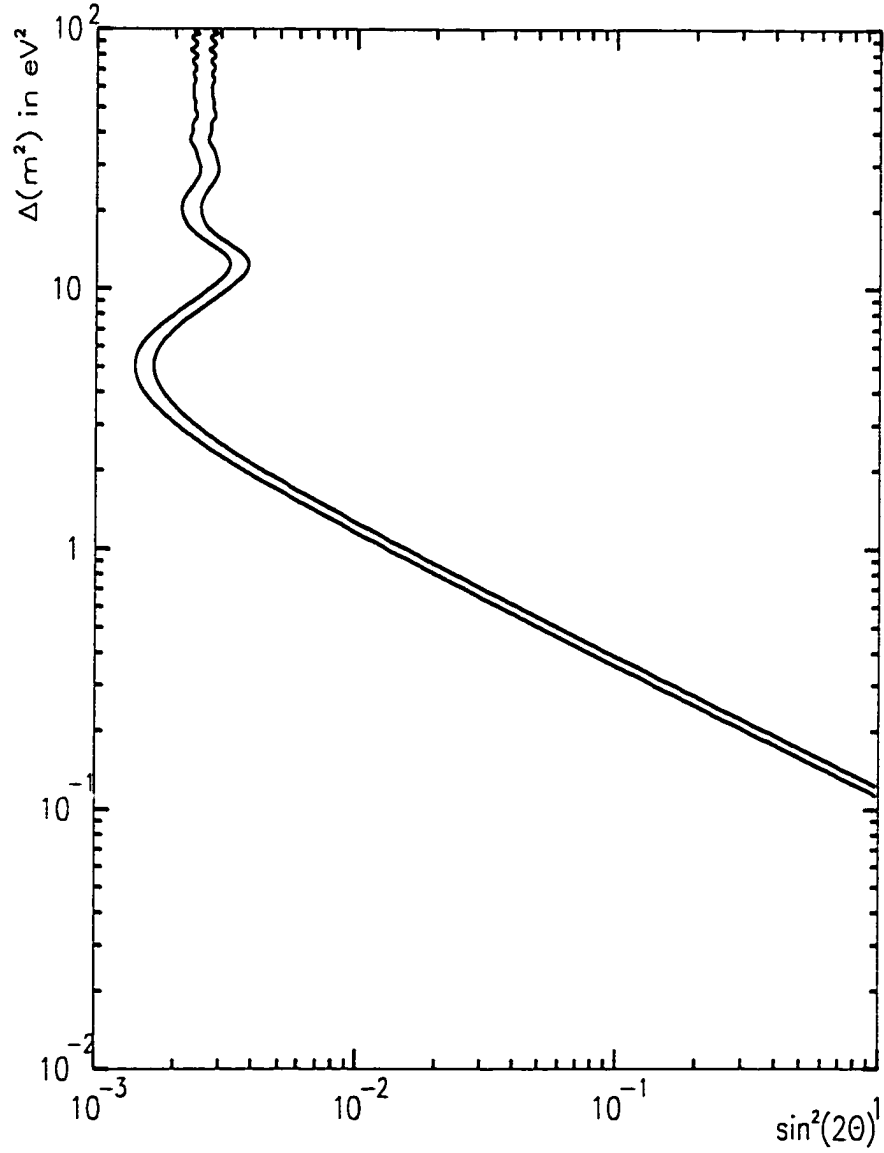


Figure 7.5: $\nu_\mu \rightarrow \nu_e$ exclusion assuming unrealistically low $\nu_e C$ cross sections. The signal and neutrino backgrounds are both arbitrarily reduced by a factor of 2 to address what is seen for the $\nu_\mu C$ cross section near threshold. This is not expected to be very relevant, but answers an often asked question.

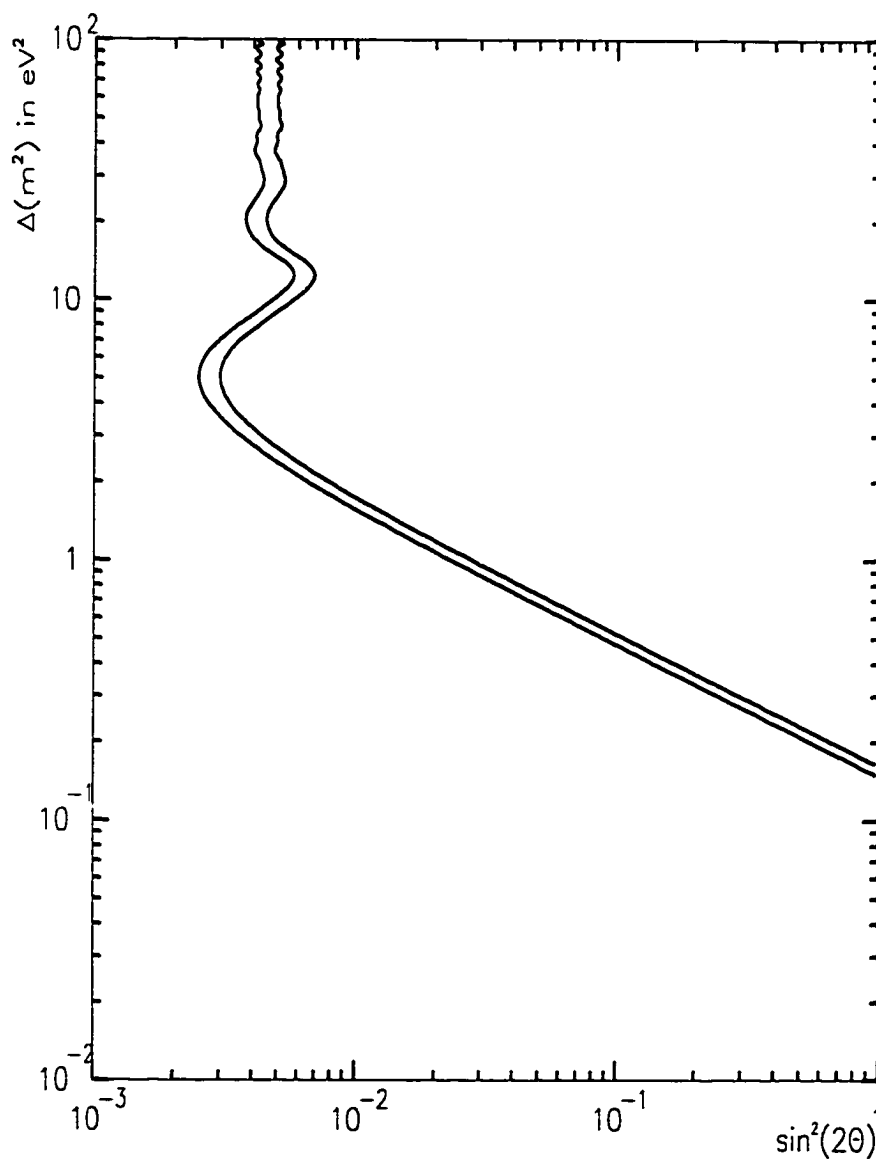


Figure 7.6: Exclusion plot for combined the data sets. The 90 and 95% limits are shown. The 90% confidence limit on Δm^2 at $\sin^2 2\theta = 1$ is $5.3 \cdot 10^{-2} \text{eV}^2$, and at high Δm^2 , $\sin^2 2\theta < 1.5 \cdot 10^{-3}$. Also shown are the separate $(\bar{\nu}_\mu \rightarrow \bar{\nu}_e)$ and $\nu_\mu \rightarrow \nu_e$ 90% confidence level curves from figures 7.1 and 7.3.

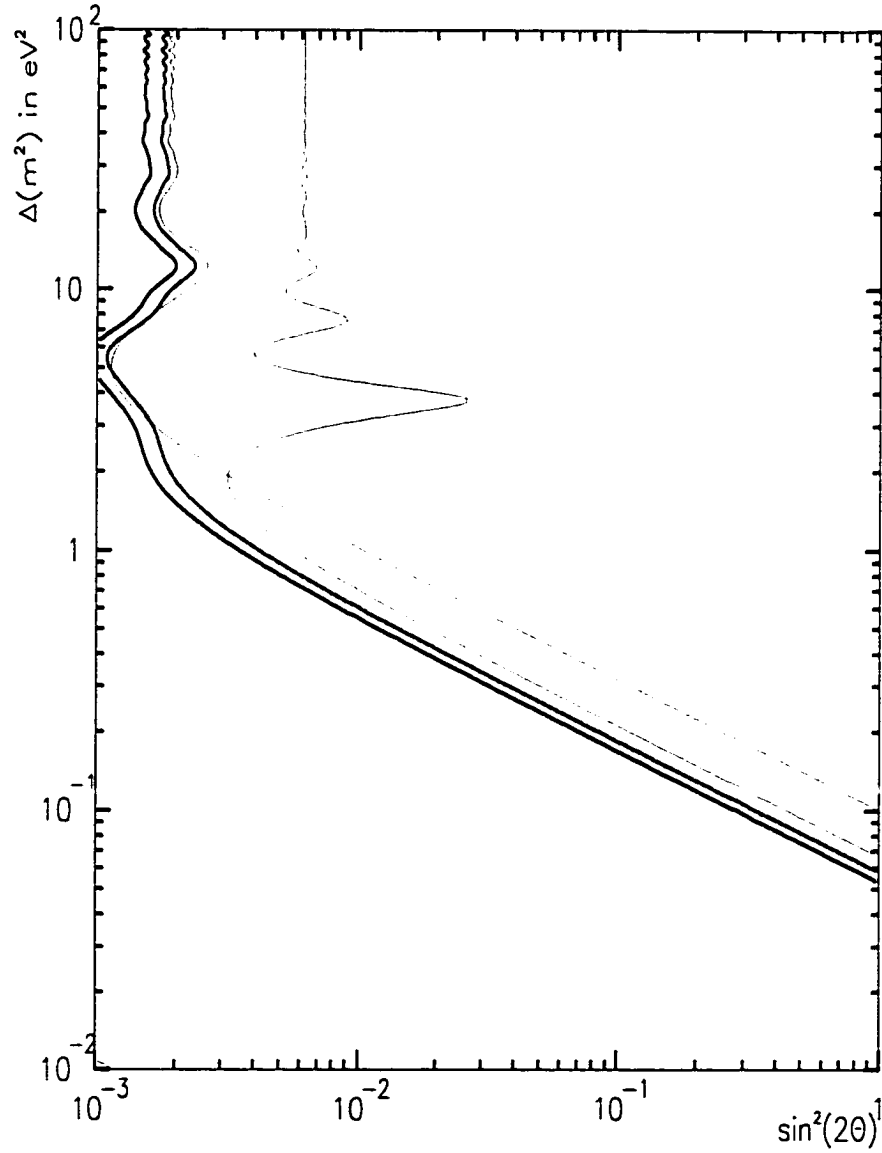


Figure 7.7: (For comparison) Combined fit result assuming 1 degree of freedom. The 90 and 95% contour levels are shown for this case.

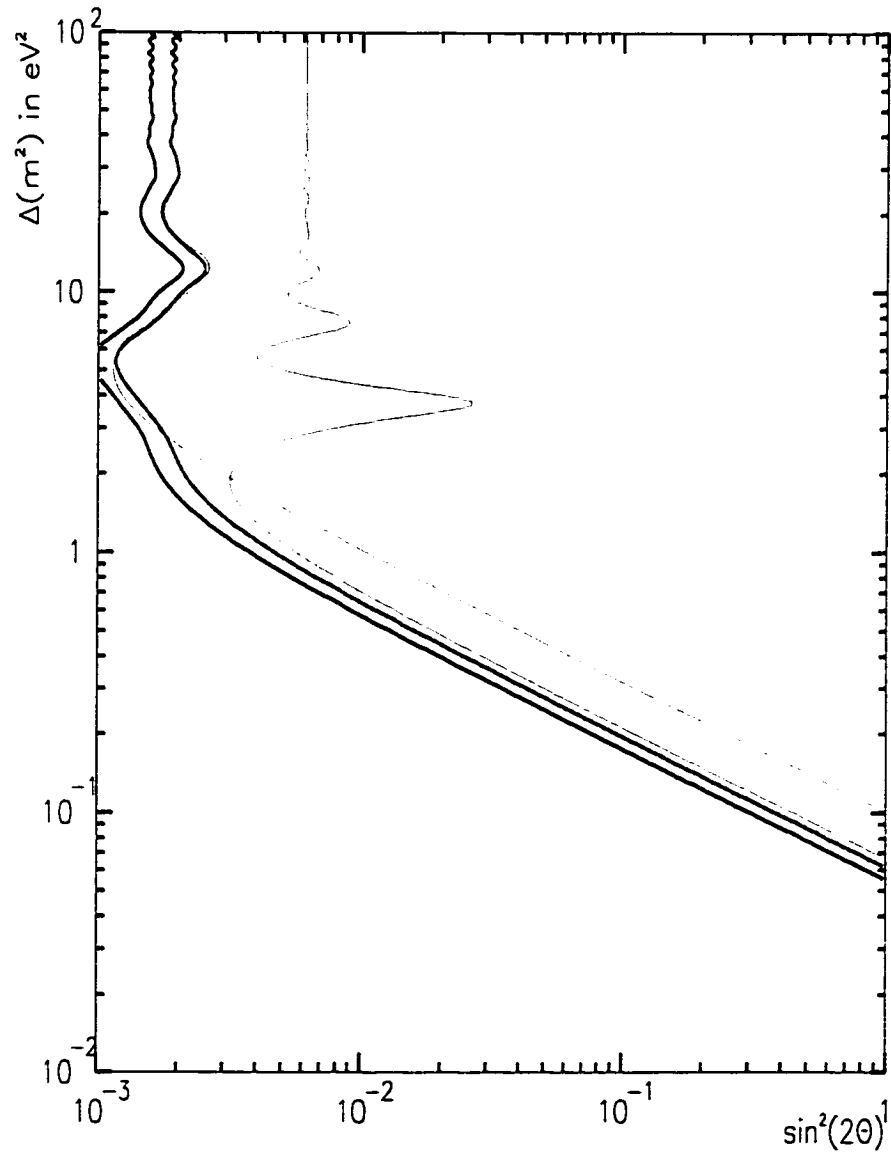


Figure 7.8: Combined fit if ν_e ^{12}C is low by a factor of 2. Again, the 90 and 95% confidence levels are shown, with the 90% confidence levels for the separate channels.

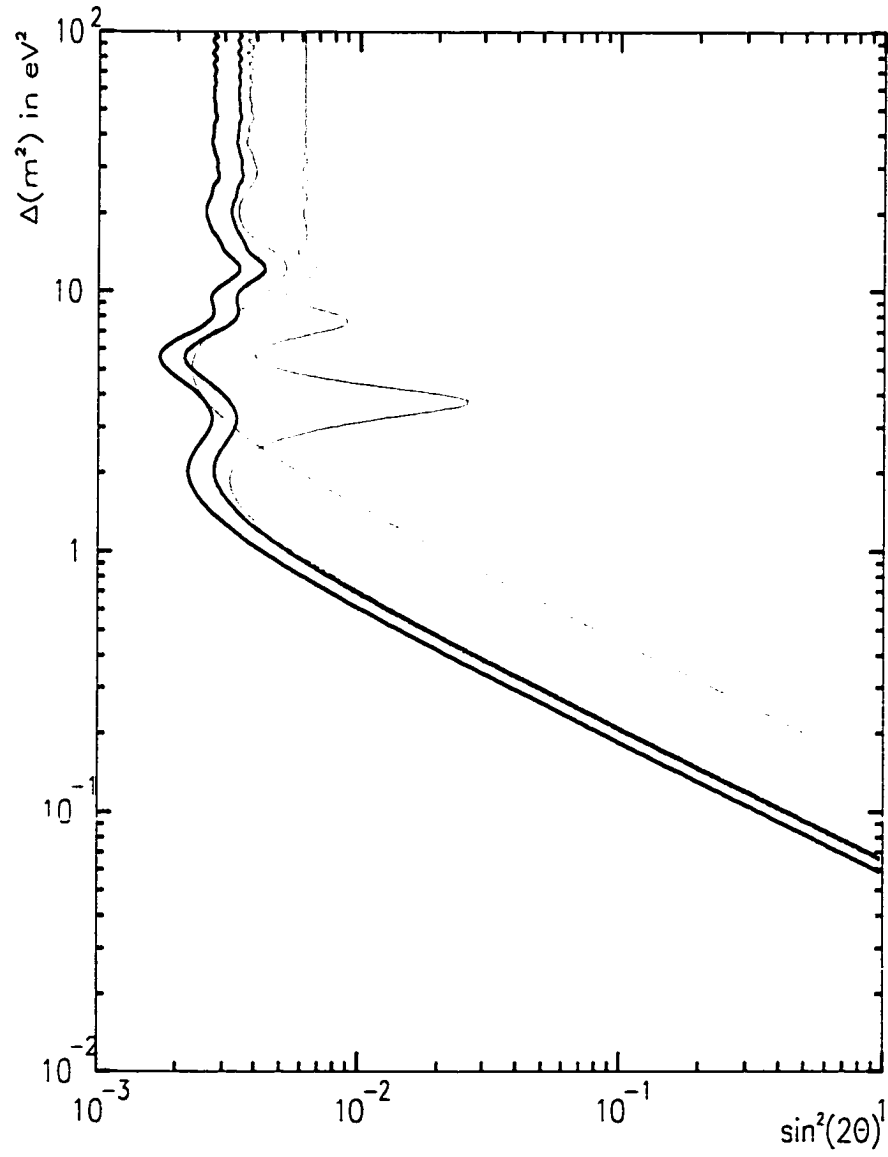


Figure 7.9: LSND limit compared to other published results. The combined fit 90% contour is shown with other relevant limits. The result of BNL-E776 shown here is their combined fit limit, and the result of KARMEN is that presented at NEUTRINO, '94. The Gösgen reactor $\bar{\nu}_e$ disappearance limit is shown, and the previous LAMPF experiment, E645.

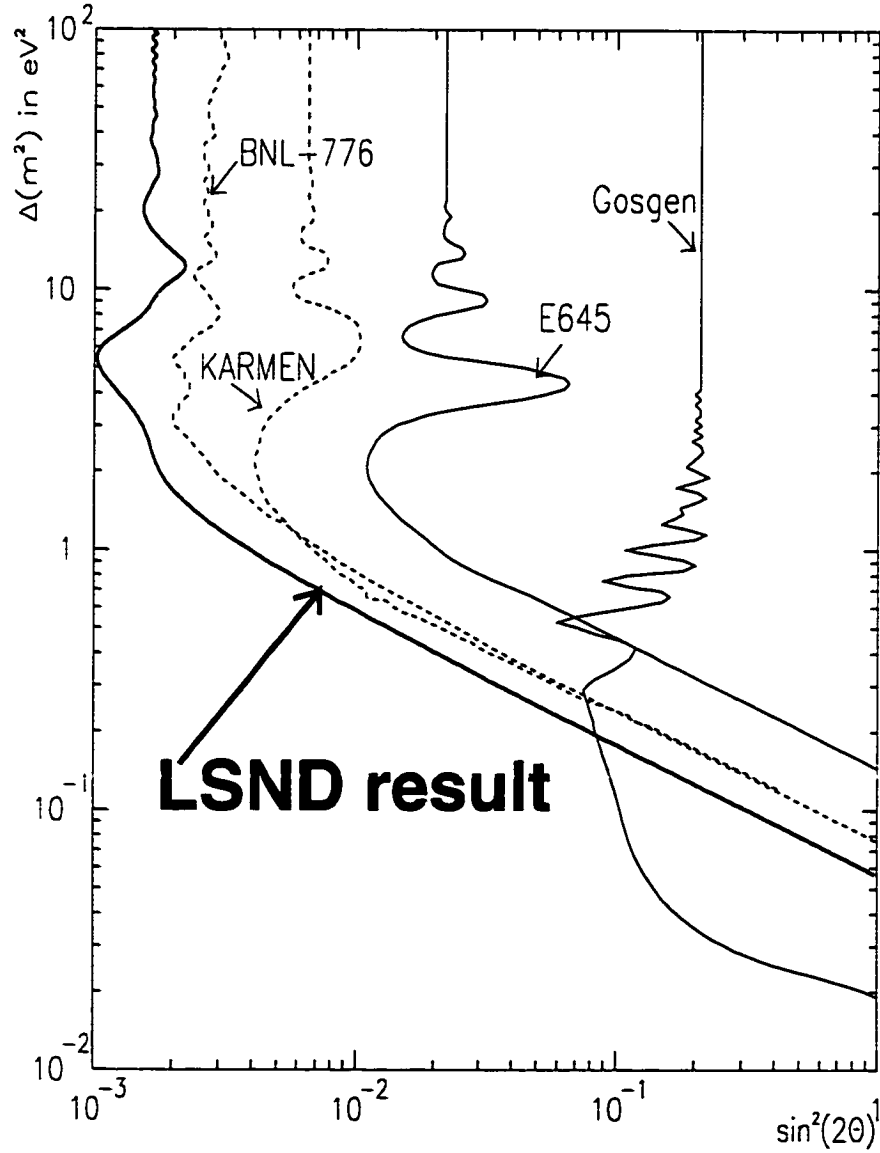


Figure 7.10: Comparison of other data and low sigma result. This is the same as the previous figure, except that the LSND result shown assumes the $\nu_e C$ cross section lower by a factor of two. The BNL experimental limit must also depend on a similar cross section.

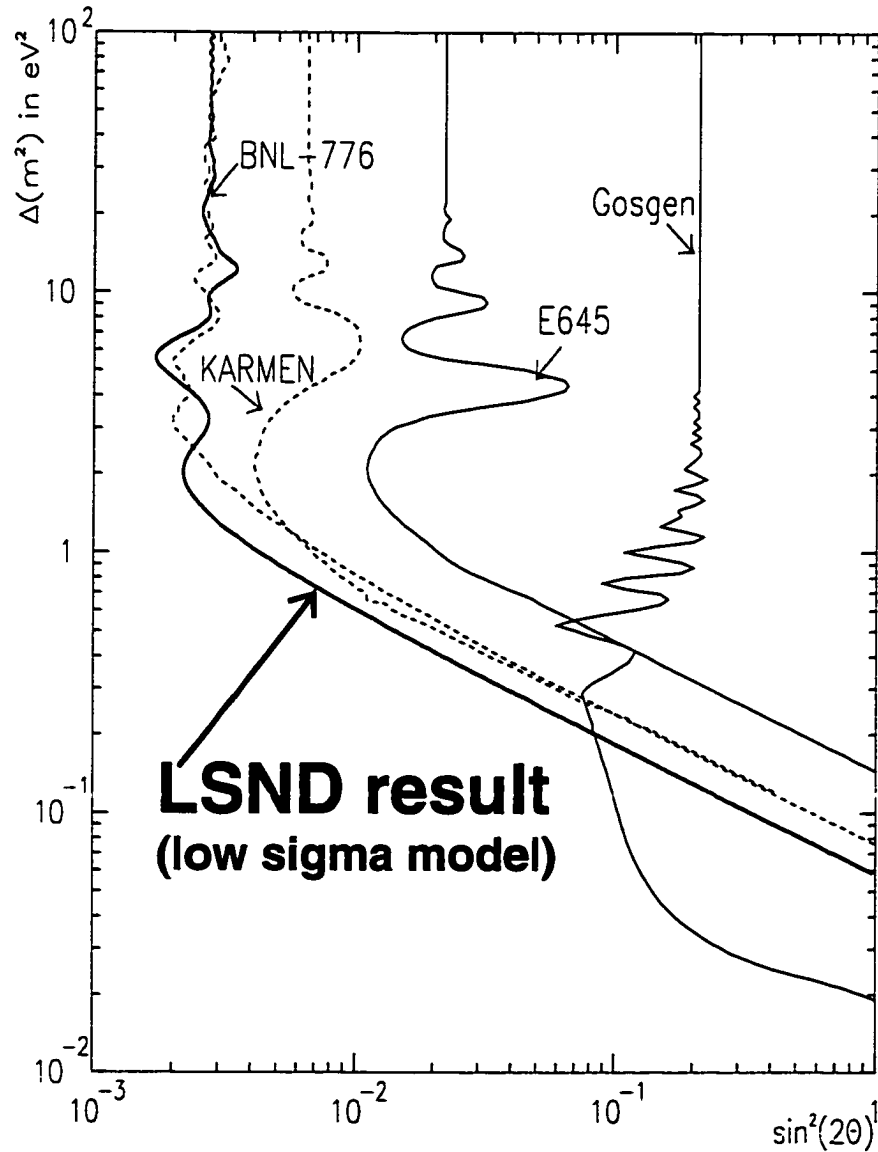
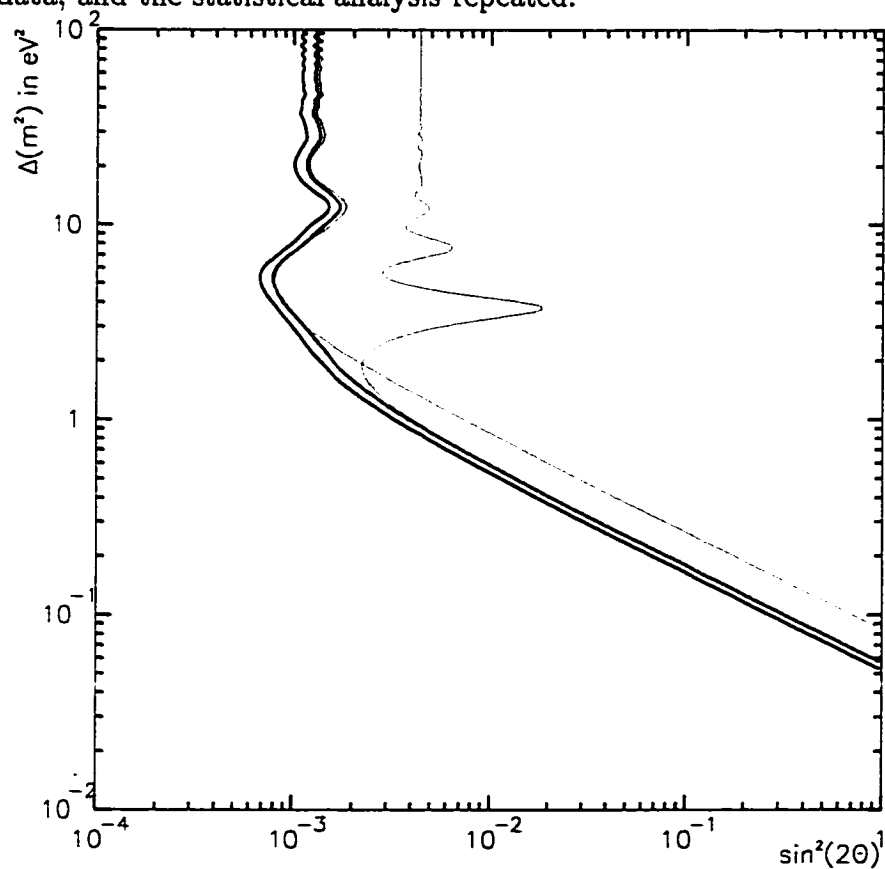


Figure 7.11: Extrapolation for limits after another 4 month run. The present backgrounds are added to both the measurement and the background from the 1994 data, and the statistical analysis repeated.



Appendix A

A critical look at other analyses presenting positive results

There have been other analyses of these data proceeding in parallel with this one. In particular, one of these analyses arrived at a positive result for the $\bar{\nu}_\mu \rightarrow \bar{\nu}_e$ search channel. (I.e.: a claim of strong evidence for neutrino oscillations.) Here, a critique of that analysis is presented with emphasis placed on what are likely problems with it. Some of the issues presented here have already been addressed in the event selection of chapter 5, but are revisited with special regard to the other analysis. A synopsis of what the author understands to be the main features of that analysis, and some critical remarks on what may have lead to the

spurious positive result will be presented. That analysis is not the work of the author and will not be presented in full here. Since there are apparently several versions of that work, it should be noted that what is discussed here is one version presented to the LSND collaboration in January of 1995, the results of which were written about in the New York Times a few weeks later. The fact that the analysis is not presented in any static form for review makes comparison difficult, but it should be made clear that what I am referring to is what I have just stated.

A.1 Event selection for the positive result

The final event selection criteria for this analysis uses many of the same variables as the selection done in chapter 5 in the main body of this work. In particular, the same reconstruction programs have been used, and the same data is included in the initial starting sample, although the other analysis chooses to keep the data from the engineering run in 1993. The total number of protons on target deposited at A6 in 1993 was 23% of the total in that sample.

The fiducial region used was defined by 35cm from the PMT faces, and either $y > -120$ or $z > 0$. This removes a small notch at the upstream bottom of the tank, where the accidental rates for both electrons and gammas are high. The projections of this volume are shown in figures A-1 and A-1. For comparison, the projections of the volume used in the result analyzed in chapter 7 are drawn on the same pictures. The pictures are approximately to scale. The analysis required no previous event within 35 μ s before the selected electron primary, and less than 2 veto system hits within the event itself. The energy range considered was the same as for this work: 37 to 60MeV electron equivalent. (Actually, there was some ambiguity about an average charge calibration for the 1994 part of the run, so at the meeting 3 extra beam on events were included. This correction for the correct calibration was made shortly after, and that change is accounted for here.)

For particle ID, there were several cuts: first, the particle ID parameter used in chapter 5 was used, but the energy dependence was not removed. The energy depen-

dence of the acceptance of this cut on a michel electron sample taken with the same energy and fiducial requirements is shown in figure A-3. This is a small but real effect. (Non-energy dependent) Cuts on the separate components of the variable already used are also in place (3 new cuts). The energy dependence of the acceptance of this combination of four cuts is also shown in figure A-3. Additional cuts on the detailed distribution of charge as a function of time within an event are used. For the result described, 4 such cuts were used, although it is claimed that using only one of them gives essentially the same result. This variable is the fraction of the total charge deposited which arrived within a 4ns window after the first PMT hit with 2 photoelectrons of charged deposited. This is to exclude events with very small precursor events, which might be expected for neutrons which knock out one or more protons with low momentum before finally dislodging one strongly enough to create the real event. The other extra particle id variables are somewhat similarly constructed, and apparently not so important.

A very important difference in this analysis is that it uses (primarily) a likelihood ratio for the tag of correlated 2.2MeV gammas. Only gammas within 2.5 meters of the primaries were considered, but the distributions that were used in the construction of the probability density functions for the ratio had the same requirement.¹ (Also, there is no requirement on low in-time veto activity for gammas, except that they pass the hardware veto of less than 6 PMT hits in the veto shield and 2 in the crack counters.) The distributions that are used in the construction of the likelihood ratio are: d_{γ}^e , t_{γ}^e , and $N_{\gamma}^{(\text{PMT})}$.

This set of criteria yields a sample of 18 beam on events, with 60 beam off. The duty factor averaged over the two years was used to do a background subtraction giving an excess of 13.5. The validity of using the average duty factor is not an issue since the background is so low anyway.

¹I would like to interject that while I do not use this technique, I do see advantages in constructing a single selection variable, and in using a method with firmer mathematical standing. Later, in section A.3.1, I explain some misgivings about the application here.

A.2 Interpretation of that event sample

The efficiency for accepting signal events for the cuts described is claimed to be $\mathcal{O}25\%$ overall. This assumes no correlations between the various detail timing PID cuts and the earlier PID cuts. (The efficiency of the latter is measured together.) The fiducial volume used is 95m^3 (about 1.6 times the fiducial volume used in this work). For large values of Δm^2 the 13.5 event excess corresponds to $\sin^2 2\theta \approx 0.01$, ruled out by an earlier experiment at BNL, *and* the analysis presented in the main body of this work. A rough approximation of the 90% confidence level *allowed* region derived from that level of signal is shown in figure A-2. The spectral information for the neutrinos that could have produced such events makes the high Δm^2 scenario less likely. (In fact, the cosmological bound of $\Sigma_{\text{mass states}} m_\nu < 20\text{eV}$ rules out very high masses. Remember that “high” for this experiment *begins at* $\Delta m^2 \approx \mathcal{O}(10)\text{eV}^2$.) Using only the result of KARMEN, the only region of parameter space available to accomodate this result lies at the peak of the detector

sensitivity for LSND and the trough for KARMEN. (The two experiments use essentially the same beam – muon decay at rest – the difference is only in the position relative to the beam. LSND is farther from its source than KARMEN is from its own, which makes LSND sensitive to slightly lower values of Δm^2 . KARMEN has been running longer, and its heavy metal target produces more pions (thus neutrinos) per proton on target. This gives an advantage in gathering high statistics.)

A.3 Questions about the validity of the sample

A.3.1 The intricacy of the selection criteria

The general idea that the more astonishing result is only seen with the more involved selection is already cause to start thinking. The use of many particle ID parameters which have correlations is a bad idea. It was confirmed on the large Michel electron sample that the one “detailed timing” cut described above showed no strong correlation to the set of four preceding PID cuts (the one used in our

analysis, and its three components). The others were still under study when the result was presented. One correlation in the initial PID variables is obvious: one is simply the product of the other three. The detector Monte Carlo has consistently estimated all these variables lower than in the data, and so could not be used fruitfully to explore correlations with the newer variables.² Other correlations exist, and one is simple to explain: If the position fit is poor for whatever reason, the angle fit cannot be expected to give a low χ^2 . This is true whether the event has a Čerenkov cone or not. The use of correlated cuts is not only a question of taste. By using correlated cuts, one makes a systematic study of the effects of varying the cuts more difficult.

The likelihood ratio used for “real” vs. accidental γ s is worth pursuing. The separate time and space correlations for capture gammas and for accidental coincidences was

²Some progress on getting the Monte Carlo distributions for particle ID parameters to match the data for such a well tagged sample as electrons from muon decay has recently been made. The detailed response of the scintillator is the main issue, and since this means that what is least trustworthy is the detailed time distribution within an event, it shows some of the difficulty in getting at the problem here.

addressed in section 4.1.3. Monte carlo predictions for the gamma energy calibration are claimed to be trustworthy, and are in good agreement with the data. The relative distance distribution is somewhat more subtle, since the data sample from which these distributions are drawn is one of high energy neutrons, and the neutrons expected in signal events are very low energy. Also, the spatial dependence of the background makes the correlation distance distribution for background events different at different points in the tank. This is never accounted for directly in the analysis. Variations where adjustments are made for the overall rate have been done (finding basic agreement with the result with no such adjustment), but the distributions used for correlation distance are the same.³ Figure 5.2 showed the distributions of correlation distance for accidental gammas in several regions of the tank. If the distributions for gammas from neutron capture are nearly constant in

³It is non-trivial to make such an adjustment, of course. What would be required is to incorporate a ratio representing each of the distributions as a function of the “observation point”. This is a significant task in itself, but then given that the best source of the prior distributions is not a tagged, but a statistically adjusted enriched sample, the prospects for provable success dwindle.

shape throughout the detector (which may or may not be a reasonable assumption), these should reject such gammas over 99% of the time. A slight variation on one of the plots from that figure (the one from the particularly active region of the tank at negative Y and Z) is shown in figure A-4. With it are the data distributions that are used in the development of the likelihood ratio. (These are essentially the same distributions as in figure 5.7. All are arbitrarily scaled to have the same maximum.) The distribution of correlation distances for the random gammas in that section of the detector looks nearly as similar to the average distribution for signal gammas as it does the one for random coincidences in this range of the variable. (The distributions used in defining the likelihood ratio were cut off at 250cm.)

A.3.2 Some questionable distributions

The evidence that the analysis may have faults lay not in its structure so much as in the comparison of certain distributions for the selected events to background, and to

predictions for a signal. Firstly, it is of note that the final beam on sample has 12 events from the 1994 run, and 6 from 1993. 23% of the total number of neutrinos has produced $\frac{1}{3}$ of the events. In this sample, the background is more evenly distributed than the putative signal, with 13 events in 1993 and 47 in 1994. For 18 events uniformly distributed over an interval, one expects the number in any small part of it chosen to be distributed approximately⁴ as a Poisson random variable of mean $\frac{\text{fraction sampled}}{\text{total number}}$. This means one expects slightly less than 4 events in 1993, and the probability of getting at least 6 is only about 20%. Therefore, the hypothesis that this data represents events uniform in time is excluded at the “ 1σ ” or 68% confidence level, but not so strongly as 90%. This alone would not be too strong an argument against the robustness of that sample.

The coordinate distributions of the candidate sample

⁴There is a small correction because the events are “chosen without replacement”. This is too small to be relevant here. The correct method is to use binomial distributions:

$$\sum_{i=6}^{18} \binom{18}{i} 0.22^i (1 - 0.22)^{(18-i)}$$

This gives about 19% for the answer.

are also suspicious. To examine this, let us posit that the Z coordinate distribution of signal is not known *a priori*, since it depends on the mixing scenario, and therefor will not be used to argue about the credibility of the sample. It has been claimed by the authors of the analysis that the coordinate distribution is not significantly skewed (in light of the low statistics). The beam on sample has 10 events at $x < 0$ and 8 at $x > 0$. This seems quite reasonable, and for ease in calculation, I concede it is not a problem at all. The Y coordinate, however, has 14 below the mid-plane of the fiducial volume (which is at $y \approx 25$; 1 event is between $y=0$ and $y=25$, and some have looked at this improperly taking that event as one in “the top part”.) To make the most liberal assumption, take it to be that all of the beam-unrelated background events that are subtracted are in the lower portion. The “fair question” to ask is: What is the probability of getting at least 9 of 13 events on either side of the midplane, in either or both of two coordinate distributions (X or Y). This is a straightforward problem in binomial statistics, and the answer is

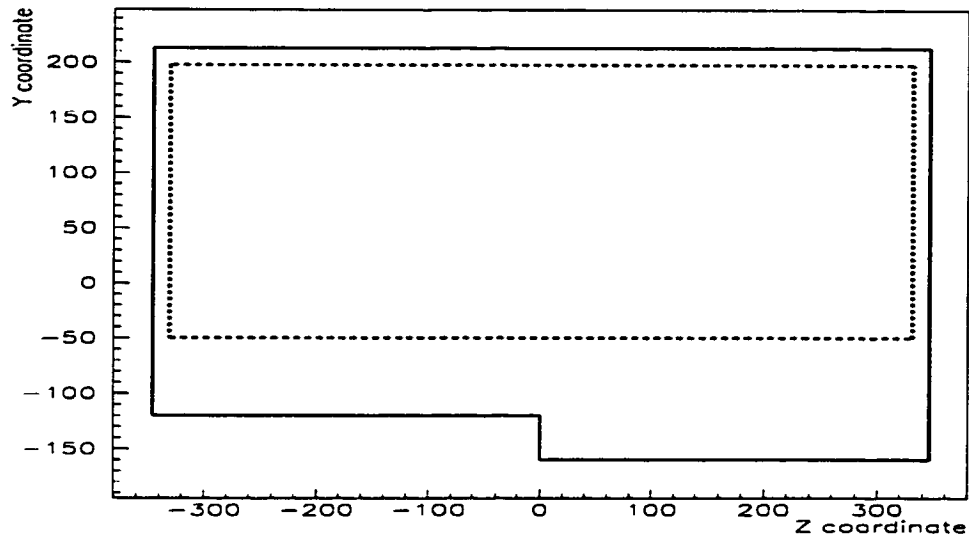
45%. A more realistic question, since the Y coordinate *is* special (in the nature of the background distribution) is just what is the probability that there come at least 9 of 13 events in one special side of that partition. The answer to that is slightly more than 13%. These two very simple counting games have each treated the sample very generously (even ignoring the nature of the background) and have each excluded the hypothesis at above the 68% confidence level.⁵ This is certainly enough to say that the data set has some rather strange properties (for a neutrino event sample) and that it is not convincing enough to significantly amend the standard model of electro-weak interactions. Stronger statements can be made by comparing the character of this sample with that of the background.

To characterize the background correctly, it is useful to “back-up” from the final sample and look at a more

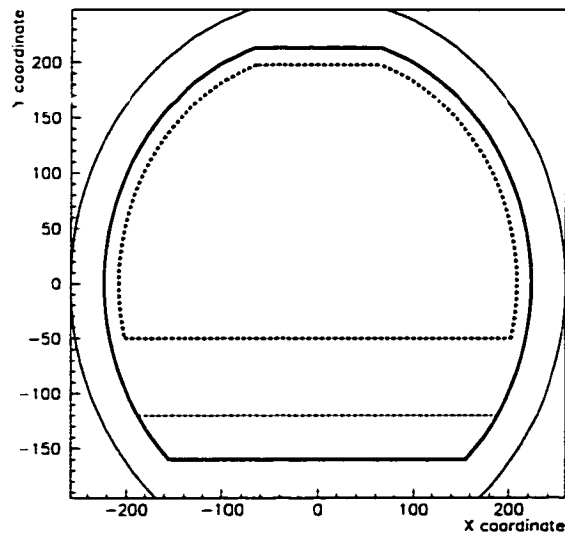
⁵Since these are essentially statistically independent distributions that have been examined, it is fair to say that *if* the questions had been devised as the sole tests of the data before the results were seen, they together would rule out that hypothesis at the $(1 - (0.2 \cdot 0.13)) = 97\%$ confidence level. This was not done, so this statement is not appropriate here. All that can be said is the results of the individual tests imply more work should be done. It is worth perhaps being a bit pedantic and saying that these are distributions that quite obviously should be checked.

loosely selected set of events which includes the final sample. The coordinate distributions for such a set are shown in figures A-5 and A-6. The same coordinate distributions are plotted for the alledged neutrino oscillation signal in the following two figures. The question is: Do these distributions look more like phase space, or more like the background?

Figure A-1: Coordinate projections of tank. The dark solid line is the volume used in the other analysis. The dark dashed line is the volume used in the main body of this work.



(a)



(b)

Figure A-2: Approximate allowed region from positive result. This is gotten by just scaling the analysis done in this work. The shaded region is the 90% allowed region. The thick solid curve is the 95% exclusion curve from chapter 7. The 90% exclusion curve from the decay at rest analysis (only) presented in chapter 7 is indistinguishable from the left border of the allowed region of the other analysis.

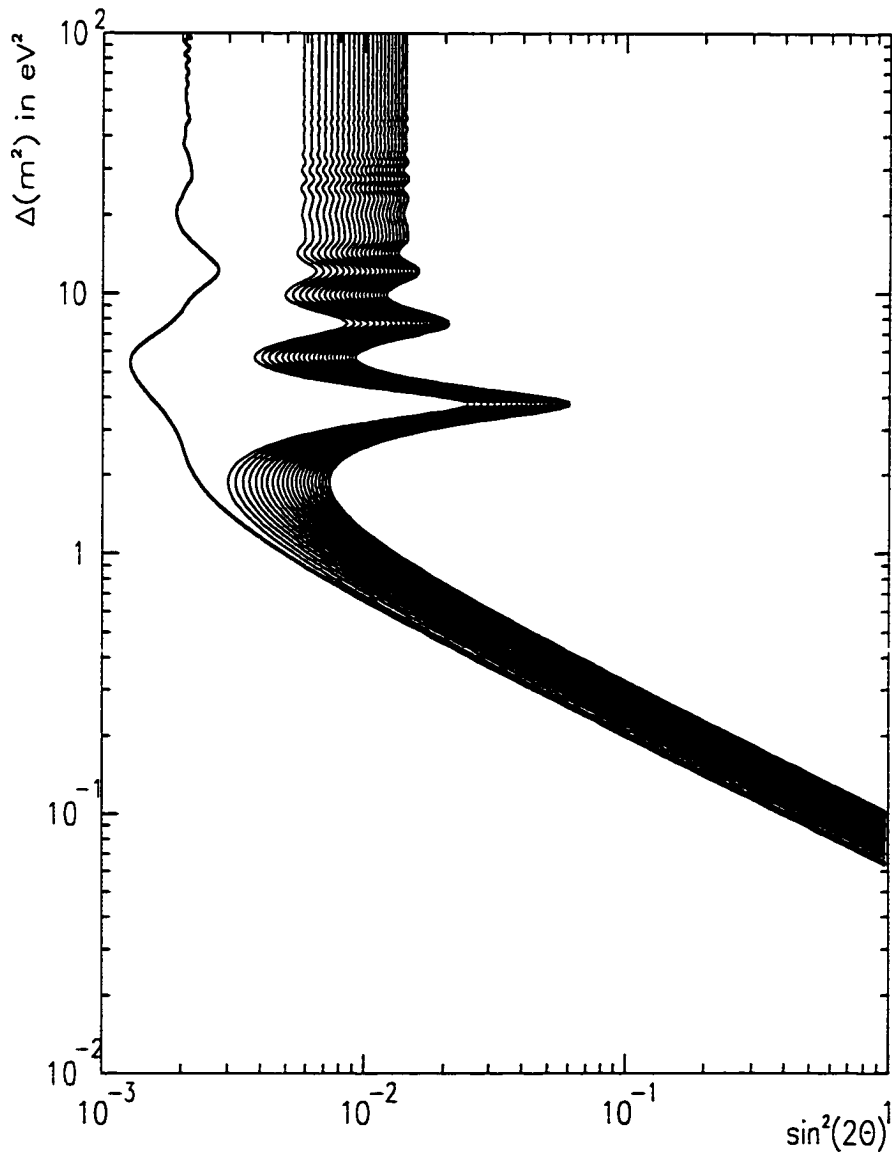


Figure A-3: Acceptance of the “flat” PID cuts as a function of energy, measured using the large sample of electrons from cosmic muon decay. The top figure is for only the cut on the single parameter defined as the product of the other three (average acceptance $89 \pm 2\%$ in 1994). Bottom is all four cuts applied at once (average acceptance $74 \pm 2\%$ in 1994). Error bars are from statistical error on counting events.

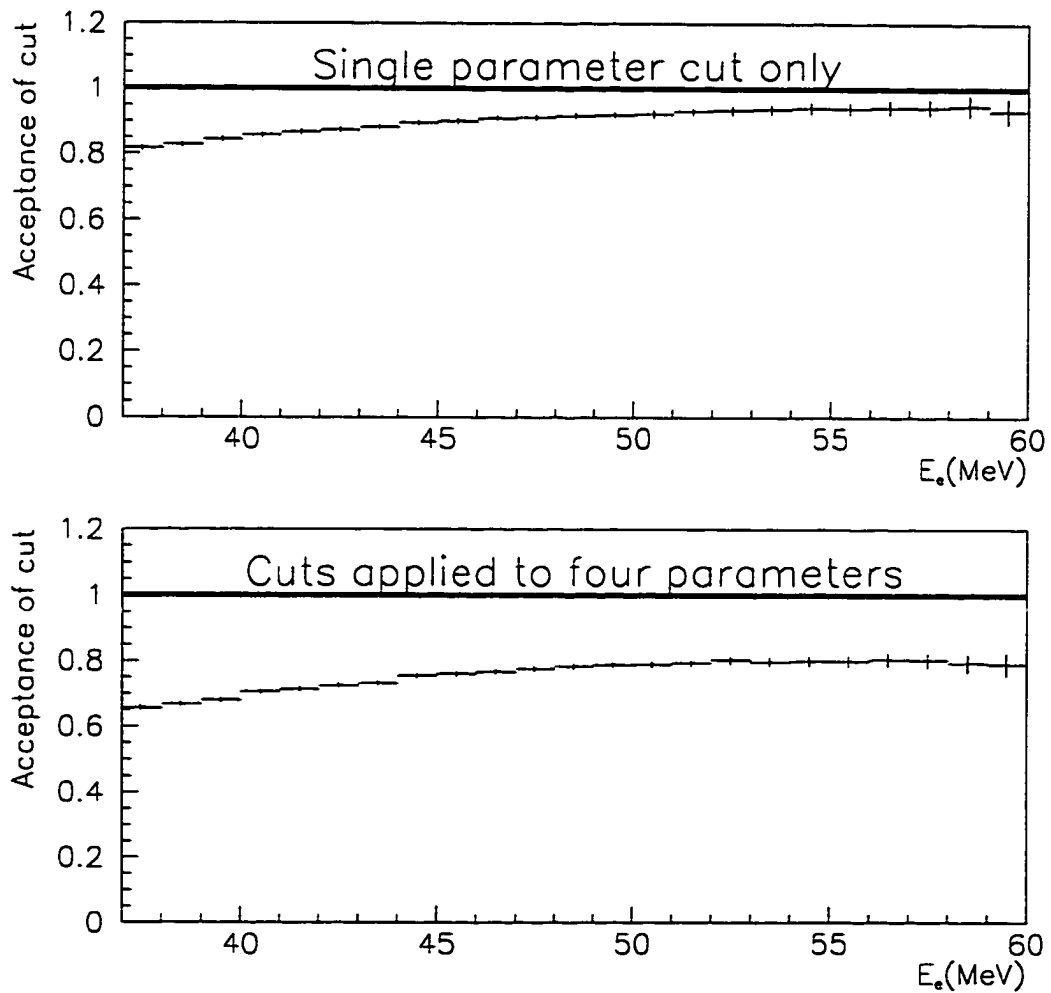


Figure A-4: Gamma correlation in a particularly bad corner. The region used is defined by $-120 < y < -50$, $z < 0$, $d_e^{\text{PMT}} > 35\text{cm}$. It is within the fiducial cut of the positive result analysis, but outside the region used in this work. 7 of the 22 events tagged as oscillation candidates lie in this 11% of the fiducial volume. The two histograms are the distributions used for accidental and correlated gammas.

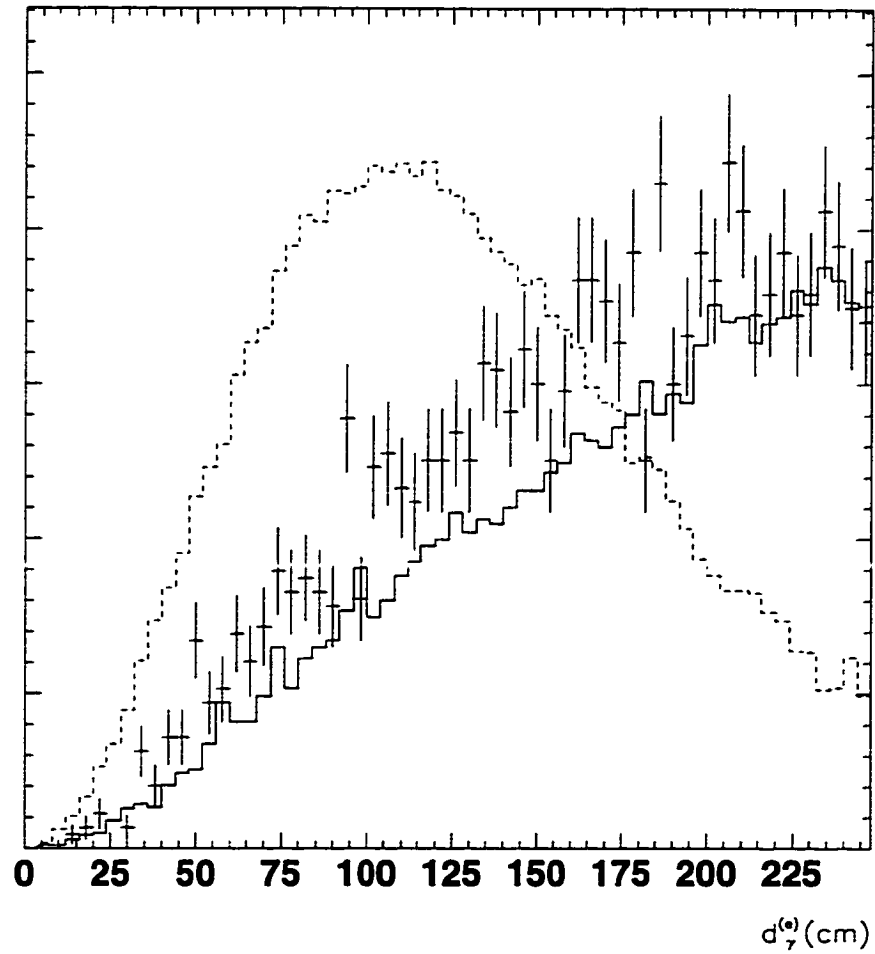


Figure A-5: Y-Z coordinate projection of background events taken from a superset of the final background sample of the positive result analysis. In particular, there is no gamma requirement for this set. This is only very minorly different from the set represented in figure 5.1, the difference being made so that this is a strict superset of the final sample relevant. It is important that the difference is not apparent, since part of the point is that this background is pervasive.

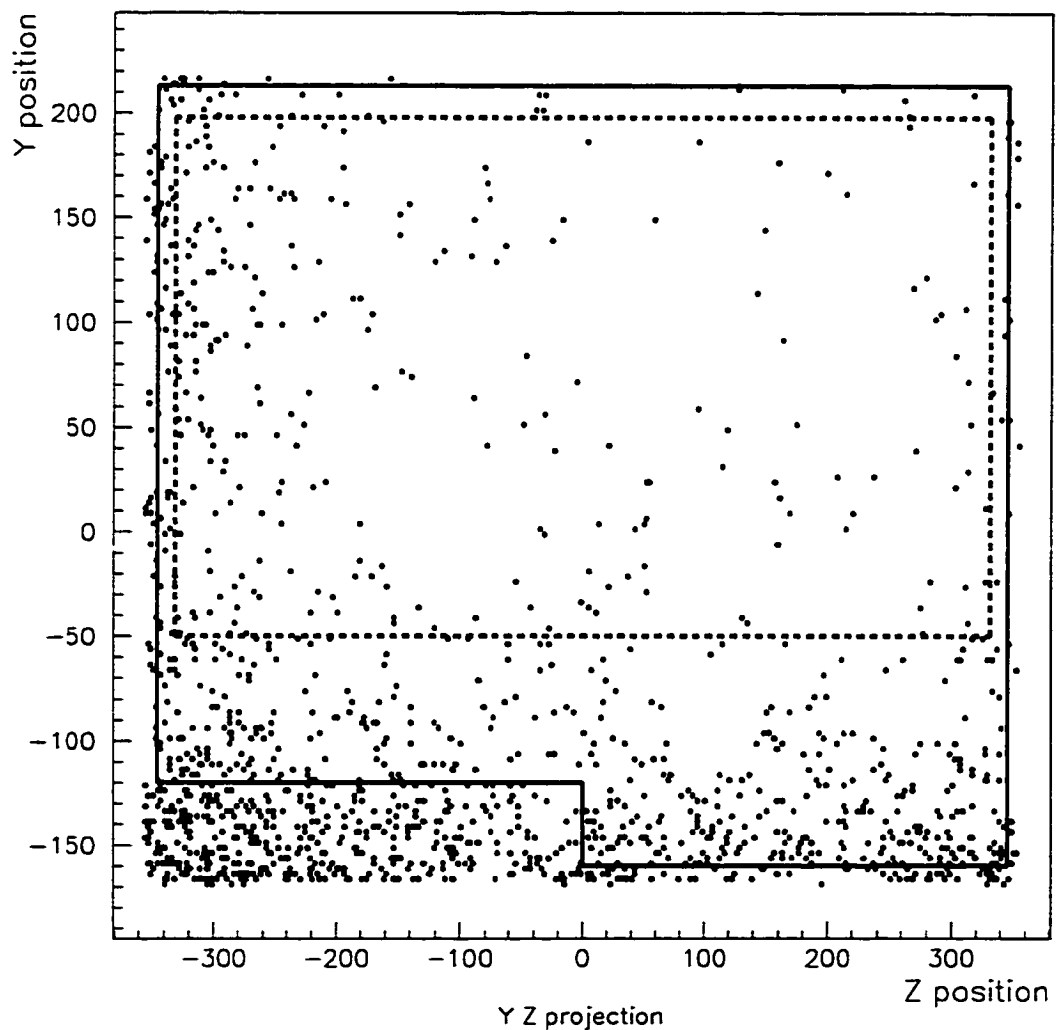


Figure A-6: Y-X coordinate projection of background events taken from a superset of the final background sample of the positive result analysis. (The same set as the preceding figure)

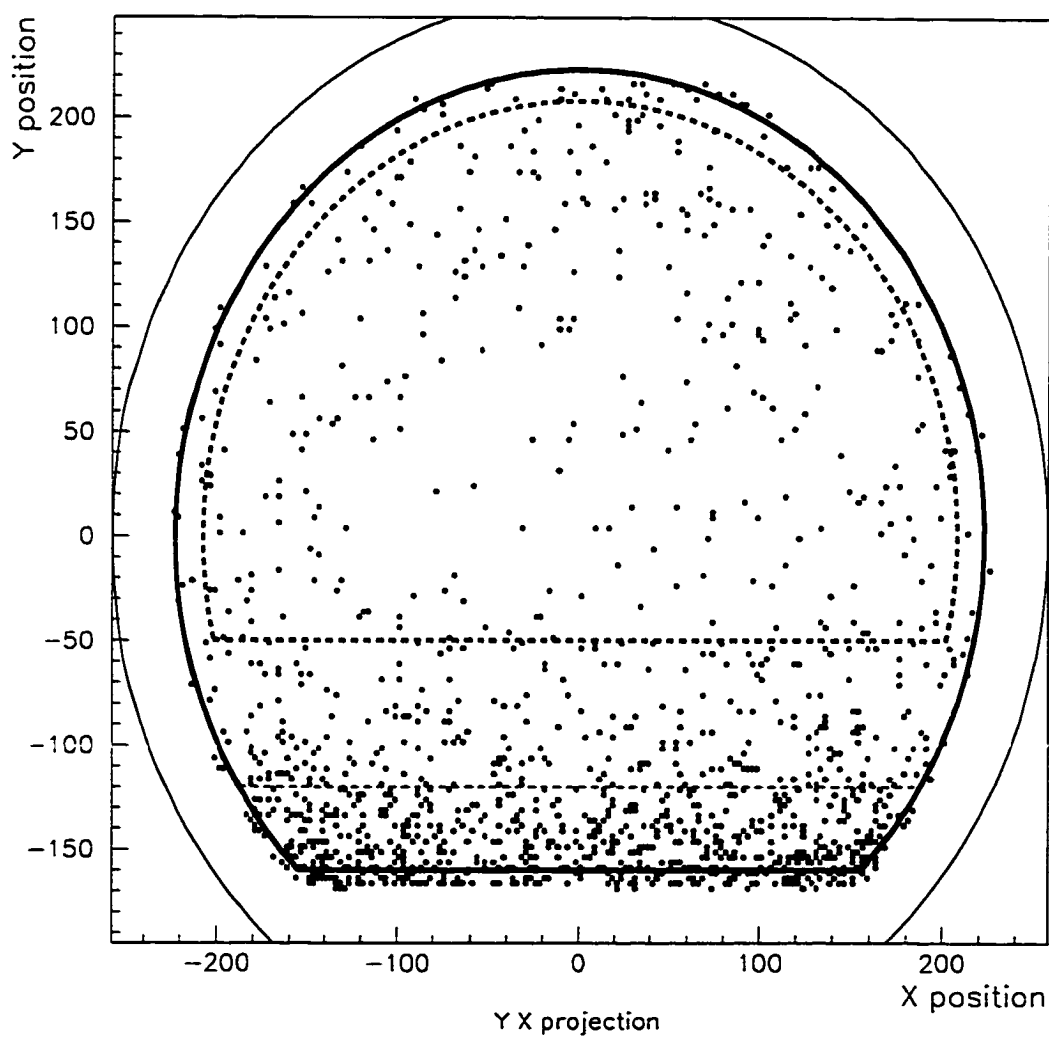
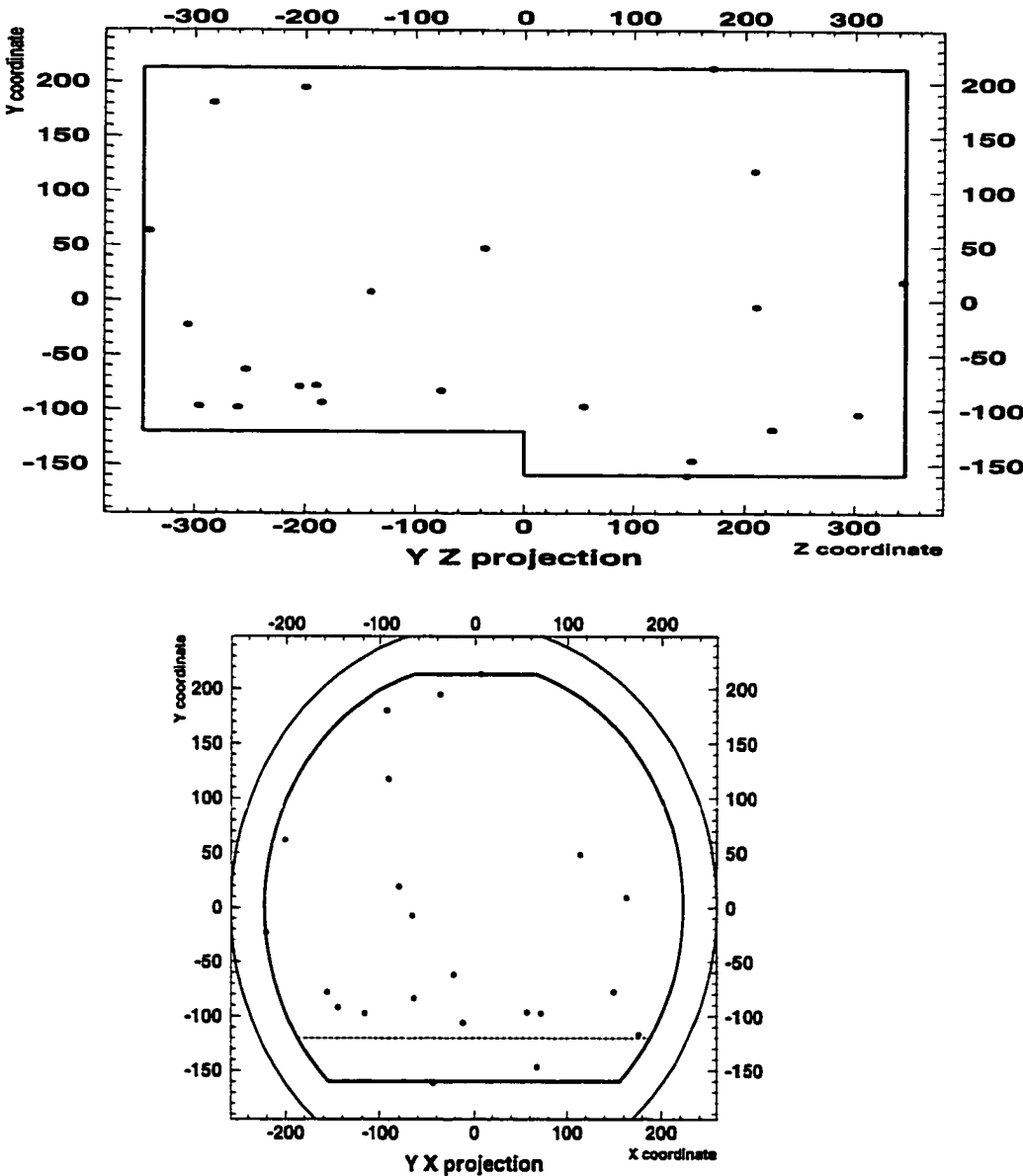


Figure A-7: Y-Z and Y-X coordinate projections of claimed signal events from analysis with positive result.



Appendix B

Understanding the LAMPF neutrino beam

The production of pions and the resulting spectrum and total flux of neutrinos from the LAMPF beam is fully modelled by the beam Monte Carlo using experimental pion yields and momentum distributions. The details of pion transport through the target and the other materials are rather complex, and lend themselves to treatment with the monte carlo method. However, a first order picture of the physics that takes place can show the rough magnitude and spectral distribution of the neutrinos produced without going into all the details of a full monte carlo simulation. There are three questions to address: What is the

total yield of pions from the proton beam? What are the relative numbers of π^\pm and π^0 ? and What is the shape of the spectrum of neutrinos produced by pion decay in flight?

B.1 Pion yields in the A6 water target

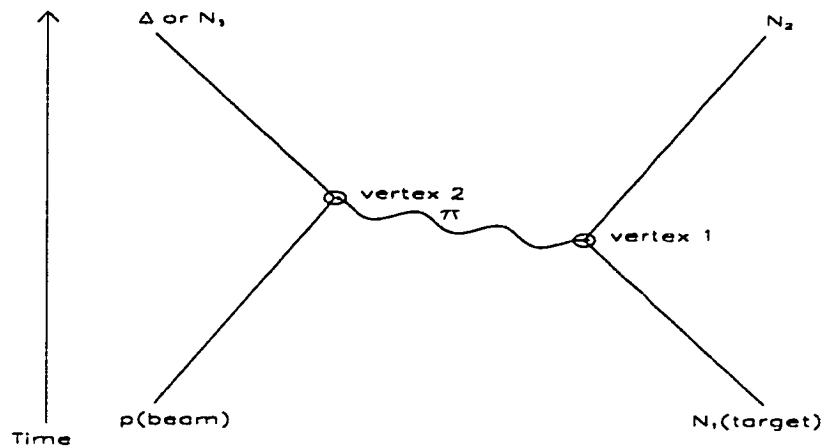
Neutrinos for LSND come from all three targets, the isotope stringers in the decay path, and the copper beam dump. Here, we will only discuss the pions from the A6 water target to get a general idea of the validity of the model.

The proton beam for LAMPF operates at 780MeV kinetic energy (= 2232 MeV in the center of mass frame) for the beam protons in the accelerator rest frame. The center of mass energy for the center of the Δ resonance is 2169MeV. (The beam is optimized so that Δ 's produced at the upstream targets have enough forward momentum to collect the produced pions in a beam. These targets degrade the total momentum at A6 by about $20\frac{\text{MeV}}{c}$.) The cross section for Δ production is proportional to a Breit-

Wigner term: $\frac{1}{(E_{\text{Res.}} - E)^2 + (\frac{115}{2})^2}$. This makes the cross section for Δ production at A6 about $\approx 45\%$ of its maximal value. The elastic cross section has two components: a Compton like part that is about 15mb; and a part that comes from (in this nuclear strong interaction description) the same process as the delta production. For protons on neutrons, there is no electromagnetic component, and the ratio of the other two parts is different. Since the strong interactions have large cross sections compared to the range of the strong force, the beam does not penetrate the nucleus, and scaling for nuclei goes as the nuclear surface area, about $A^{2/3}$, *and should reflect the nature of only those nucleons in the outermost nuclear shell*. For the electromagnetic part, since the force is long range, the screening effect is negligible, and the cross section scales as Z . Thus, the total cross section is, in this approximation, $Z\sigma_{\text{em}} + A^{2/3}\sigma_{\text{strong}}(\text{outer shell})$.

Before continuing with the full nuclear cross sections and the total pion yields, it is useful to first look at the processes for Δ production, and calculate the expected

number of pions of each type for protons on protons and for protons on neutrons. The generic process under study is:



In this picture (which is *not* to be taken as a diagrammatic representation for a series expansion) the first vertex is within the target nucleus and relies on the details of the nuclear pion field. (Since the emission of the crossing pion requires the initial nucleon to be off shell, the beam proton is not likely to do this.) The possible products are assumed to be a nucleon, which remains in the nucleus, and a pion which intermediates the interaction with the beam. The amplitudes for branching ratios to the allow states are

taken to be Clebsch-Gordon coefficients. In the case where N_1 is a proton, the only possibilities for the crossing pion are π^+ and π^0 , since π^- would leave no allowed nucleon for N_2 . The emission of π^+ is three times as likely, using the square of the Clebsch-Gordon coefficients. The state with π^0 and the beam proton can yield final states with Δ^+ , or just p^+ with relative probabilities $\frac{2}{3}$ and $\frac{1}{3}$. The state with π^+ crossing can only yield the Δ^{++} resonance. For target neutrons, the same analysis gives for each 9 scatters: 4 states with no resonance, two with Δ^+ , and 3 with Δ^0 . Since the relative decay rates of the resonances into the possible pion-nucleon pairs is also determined by Clebsch-Gordon coefficients, these processes contribute for each interaction on target proton:

$$\frac{3}{36}\text{elastic scatters, } \frac{29}{36}\pi^+, \text{ and } \frac{4}{36}\pi^0,$$

and for each interaction on a neutron:

$$\frac{12}{27}\text{elastic scatters, } \frac{2}{27}\pi^+, \frac{10}{27}\pi^0, \text{ and } \frac{3}{27}\pi^-.$$

For pp interactions at the Δ^+ resonance, the pion production cross section is (about) 28 millibarns. This implies

that the total cross section for the above “ Δ like processes” should be $\frac{36}{33}$ of this, or 30.5mb. At LAMPF beam energies, the cross section for strong interactions should then be $13\frac{3}{4}$ mb. Since we assume isospin invariance, this is the same for neutrons. Note, however, that this does *not* imply that the pion production rates are the same for all nucleons.

The pp electromagnetic cross section at this energy is about 15mb. pn interactions, of course, do not contribute. For hydrogen, then, the total cross section for protons in the LAMPF beam is (15mb “Compton like” + $13\frac{3}{4}$ “ Δ like” =) 29mb. For ^{16}O the total cross section is:

$$8 \cdot 15 + 16^{2/3} \cdot \left(13\frac{3}{4}\right) = 207\text{mb},$$

and the strong part should reflect that protons and neutrons are equally represented in the outermost nuclear shell. For ^{56}Fe :

$$26 \cdot 15 + 56^{2/3} \cdot \left(13\frac{3}{4}\right) = 591\text{mb},$$

and the outermost nuclear shell is entirely of neutrons. The relative probabilities of the different final states for each scatter from nuclei are found as follows:

For ${}^1\text{H}$:

σ	elastic	π^+	π^0	π^-			
15.)	1	:	0	:	0	:	0
$1^{2/3} \cdot 13\frac{3}{4}$.	$\frac{3}{36}$:	$\frac{29}{36}$:	$\frac{4}{36}$:	0
28.7mb total	16.145	:	11.073	:	1.527	:	0
per interaction	0.562	:	0.385	:	0.0531	:	0

For ${}^{16}\text{O}$:

$(8 \cdot 15.)$	1	:	0	:	0	:	0
$(\frac{16^{2/3}}{2} \cdot 13\frac{3}{4}.)$	$\frac{3}{36}$:	$\frac{29}{36}$:	$\frac{4}{36}$:	0
$(\frac{16^{2/3}}{2} \cdot 13\frac{3}{4}.)$	$\frac{12}{27}$:	$\frac{2}{27}$:	$\frac{10}{27}$:	$\frac{3}{27}$
207mb total	143.04	:	38.398	:	21.018	:	4.850
per interaction	0.690	:	0.185	:	0.101	:	0.0234

For ${}^{56}\text{Fe}$:

$(26 \cdot 15.)$	1	:	0	:	0	:	0
$(56^{2/3} \cdot 13\frac{3}{4}.)$	$\frac{12}{27}$:	$\frac{2}{27}$:	$\frac{10}{27}$:	$\frac{3}{27}$
591mb total	479.45	:	14.908	:	74.541	:	22.362
per interaction	0.811	:	0.0252	:	0.126	:	0.0378

Since hydrogen and oxygen occur together in a molecule, it is useful to think of it as one unit with a total cross section of $2\sigma_{\text{H}} + \sigma_{\text{O}} = 264\text{mb}$, with the relative probabilities

of the different final states for each scatter from any nucleus in the molecule:

$$0.665 : 0.229 : 0.091 : 0.018$$

For a cubic centimeter of water (density $1 \frac{\text{g}}{\text{cc}}$), there are $\frac{6 \cdot 10^{23}}{18}$ molecules, so the average volume occupied by a single molecule is $3 \cdot 10^{-23} \text{cm}^3$. The fraction of protons that produce pions for a given length of water is then $1 - e^{-L/\lambda}$, where the attenuation length $\lambda = \frac{\text{volume}}{\sigma}$ for a single molecule, here 114cm. For iron, the density is $7.9 \frac{\text{g}}{\text{cc}}$, so the attenuation length is only 20cm.

In the 30cm A6 target, there are approximately 2cm of stainless steel (comprising the case, and several dividers within the water). The fraction of beam protons that react in this volume is then:

$$1 - e^{-\left(\frac{28}{114} + \frac{2}{20}\right)} = 0.293$$

The ratio of scatters from iron nuclei to scatters from nuclei in water is $\frac{2/20}{28/114} \approx 0.29 : 0.71$ Therefore, the overall ratio of the different channels is:

$$0.71 : 0.17 : 0.10 : 0.023$$

The two results from this to compare to the Monte Carlo are the ratio of $\pi^- : \pi^+ = 13\%$, for which 14% is the result of the full Monte Carlo (looking *only* at pions produced in the region before the stringers), and a total yield of π^+ of 5%, where the complete calculation gives about 8.8% for the whole A6 area, where many pions are produced in the stringers and beam dump (and more in the target itself from non-resonant production).

B.2 The decay-in-flight spectrum of ν_μ

For the thin upstream targets where the momentum of the produced Δ 's is a little higher than in A6, the pions are produced in essentially a forward directed beam. In A6, however, the production of pions is much more nearly isotropic. The neutrino spectrum assuming for isotropically distributed pions can be computed relatively straightforwardly. (The exact spectrum for a given distribution could be calculated, but the exact pion distribution is very sensitive to the details of the geometry. To go into the full details of the exact calculation would obscure the physics

with geometry.)

Taking the above model for pion production in A6, since the nucleon in the target nucleus is assumed to remain in that nucleus, the linear momentum of the beam is transferred wholly to the Delta. This decays before any significant momentum loss, so that the center of mass spectrum of pions (a line spectrum) needs only to be Lorentz boosted by the appropriate factor. The width of the resonance must be taken into account, but the spectrum is cut off at the mass corresponding to the total available energy, producing a continuous spectrum of pions extending up to around $\frac{1}{2}\text{GeV}$.

B.2.1 Detailed calculation assuming a spatially isotropic pion spectrum.

For isotropically distributed pions, the spectrum of neutrinos at a given angle is the same as the spectrum from a linear beam integrated over 4π solid angle.¹ In the center of mass frame of the decay products of a pion (for the chan-

¹This is assuming that the observation point is far enough away so that the pion travel distance is small. In itself, this is a fair assumption for this case, however the asymmetry of the target area introduces further complications.

nel $\pi^+ \rightarrow \mu^+ + \nu_\mu$) the directional distribution is isotropic (for unpolarized pions). I.e.: $u^* \equiv \cos(\theta_{rest}^{(\pi)})$ is uniformly distributed on $[-1, 1]$.

For a particular neutrino from a pion of velocity β (hence Lorentz factor γ) in the lab frame, its energy in the lab frame is $E_\nu = \gamma E_\nu^{(c.m.)} + \gamma \beta p_\nu^{(c.m.)} u^*$. Since this is a simple 2-body decay, and the neutrino is nearly massless,

$$E_\nu^{(c.m.)} = c \cdot p_\nu^{(c.m.)} = \frac{\sqrt{M_\pi^4 - 2M_\pi^2(m_\mu^2 + m_\nu^2) + (m_\mu^2 - m_\nu^2)^2}}{2M_\pi}$$

$$\approx \frac{M_\pi^2 - m_\mu^2}{2M_\pi} = 29.4 \text{ MeV}$$

Thus, we can write: $E_\nu = E_0 \cdot \gamma(1 + \beta_\pi u^*)$ for pions of a particular energy, where $E_0 = 29.4 \text{ MeV}$ is the pion rest frame energy of the neutrino. *So the neutrino spectrum from pions at a particular energy is uniformly distributed over a specific interval.* In terms of the pion energy:

$$\frac{E_\nu}{E_0} = \left(\frac{E_\pi}{m_\pi} + u^* \sqrt{\left(\frac{E_\pi}{m_\pi} \right)^2 - 1} \right).$$

The integral over u^* is done numerically producing the neutrino spectrum shown in figure B-1. For comparison, the Monte Carlo neutrino spectrum for π^+ decay in flight

(integrated over a grid of points in the tank) is shown in figure B-2.

Figure B-1: Analytically calculated spectrum of ν_μ from π decay in flight. This simple calculation is insensitive to the charge of the pions, but the fraction of π^+ produced outside the water target is insignificant, while this is not true for π^- . The hard tail is systematically high because the beam stop is not accounted for. (Stopping the pions affects the higher energy ones preferentially.)

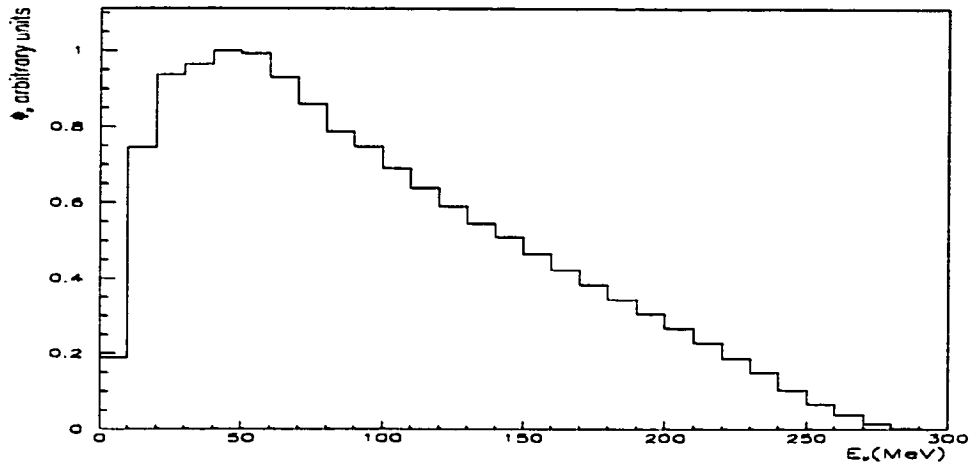
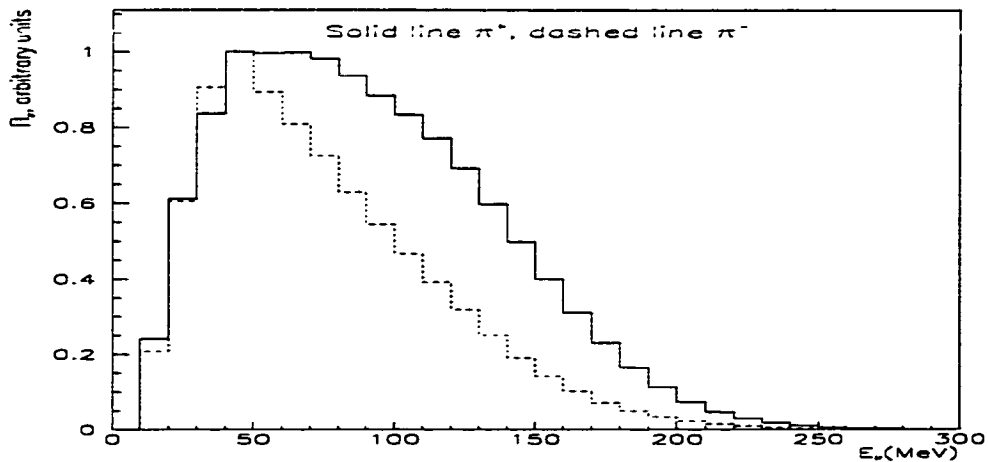


Figure B-2: Monte Carlo spectrum for π^\pm decay in flight from A6. All the geometry is accounted for as well as possible.



Bibliography

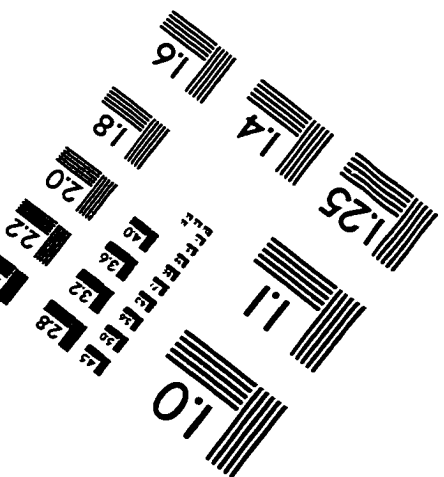
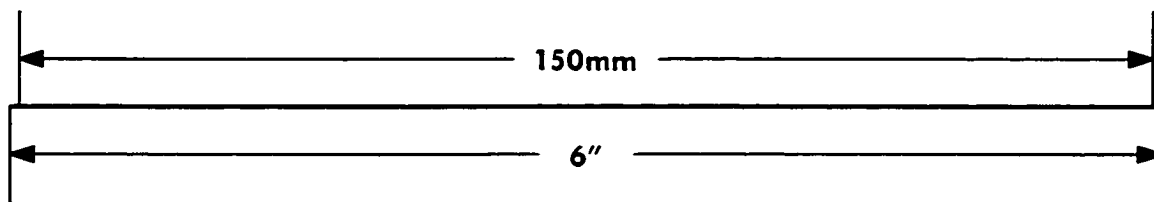
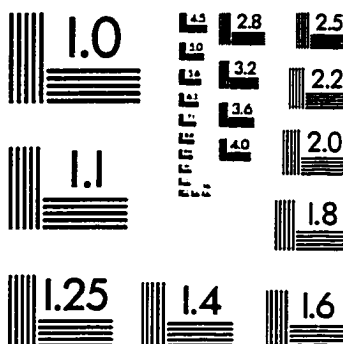
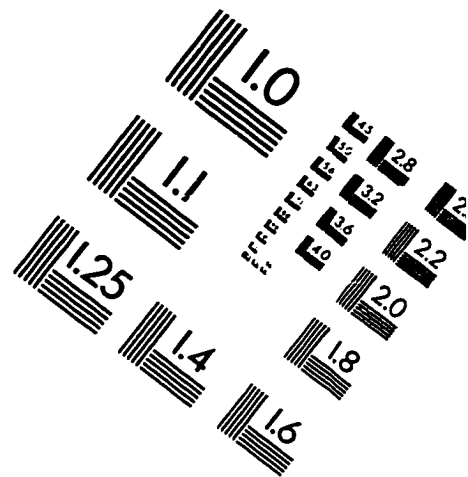
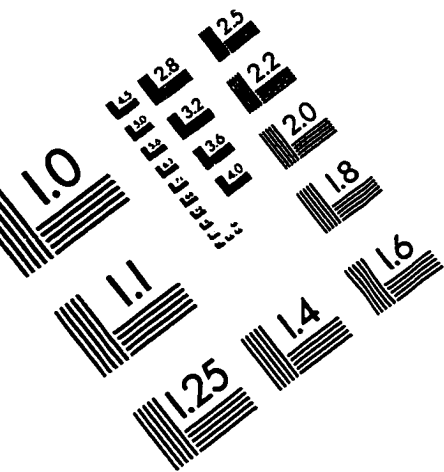
- [1] Pontecorve, B., *Zh. Eksp. Theor. Phys.* **33**, 549
1957, translated *Sov. Phys. JETP* **6**, 429 (1958).
- [2] Boehm, F. and Vogel, P., *The Physics of Massive Neutrinos* , (Cambridge University Press, Cambridge, G.Br., 1992)
- [3] B. Kayser, *with* F. Gibrat-Debu and F. Perrier, *The Physics of Massive Neutrinos* , (World Scientific Publishing Co. Pte. Ltd., Teaneck, N.J., 1989)
- [4] Mohapatra, R, and Pal, *Massive Neutrinos in Physics and AstroPhysics*, (World Scientific Publishing Co. Pte. Ltd., Teaneck, N.J., 1991)
- [5] J. Cronin in **Hawaii Topical Conference in Particle Physics, 1971**, (Proceedings), ed. Yount & Dobson, 1971.

- [6] B. Blumenfeld, private communication. There is evidently some question within the BNL-E776 collaboration about the method in which the two channels of oscillation search data were combined.
- [7] Christos Athanassopoulous, *The Cross Section for $C(\nu_\mu, \mu^-)X$ Near Threshold*, Doctoral Dissertation, Temple University, 1995.
- [8] Michael Albert, *A Measurement of the Reaction $C(\nu_\mu, \mu^-)X$ Near Threshold*, Doctoral Dissertation, Univ. of Penn., 1994
- [9] R.L.Burman, *et al.*, Nucl. Instr. Meth., **A291**, (1990) 621.
- [10] R.C.Allen, *et al.*, Nucl. Instr. Meth., **A291**, (1989) 347.
- [11] Konopinski, E. J., *The Theory of Radioactive Beta Decay*, Clarendon Press, Oxford, (1966).
- [12] B.E. Bodman, *et al.*, (KARMEN Collaboration), Phys. Lett., **B332**, (1994) 251.

- [13] J.D.Jackson, *Classical Electrodynamics*, (Wiley & Sons, New York, 1975)
- [14] L. Montanet, *et al.*, (Particle Data Group),
Phys. Rev. **D50**, 1173 (1994).
(the **Particle Data Book**)
- [15] J. Napolitano, *et al.*, Nucl. Instr. Meth., **A 274**, 152 (1989).
- [16] Strossman, W., *The search for $\nu_\mu \rightarrow \nu_e$ at LAMPF*,
Doctoral Dissertation, Univ. Cal., Riverside, 1995.
- [17] Reeder, R., *et al* , Nucl. Instr. and Methods, **A334**
(1993) 353.
- [18] Strossman, W., private communication.
- [19] R.Gunasingha, Ph.D. thesis in preparation, Louisiana
State Univ., 1995 (and private communications
thereon).
- [20] David L. Works, *A Search for $\nu_\mu \rightarrow \nu_e$ in the Ap-
pearance Channel*, Doctoral Dissertation, Temple
University, 1995.

- [21] Naoya Hata, *Theoretical Implications of Solar Neutrino Observations*, Doctoral Dissertation, University of Pennsylvania, 1994
- [22] Orear, J., “Notes on Statistics for Physicists”, (*Lecture Notes*), Laboratory for Nuclear Studies, Cornell University, Ithaca, NY, 1982.
- [23] G. Drexlin, **1994 International Conference on Neutrino Physics and Astrophysics** (proceedings) (1994).

IMAGE EVALUATION TEST TARGET (QA-3)



APPLIED IMAGE, Inc
1653 East Main Street
Rochester, NY 14609 USA
Phone: 716/482-0300
Fax: 716/288-5989

© 1993, Applied Image, Inc., All Rights Reserved

